

Structural Correlation and Tunability of Magnetic and Electric Properties of Manganese doped Cobalt ferrite Nanoparticles

by

Md. Ziaul Ahsan
ROLL No: 1015144006P
Session: October 2015

DOCTOR OF PHILOSOPHY IN PHYSICS





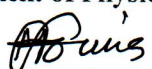
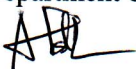
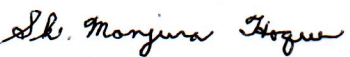


Department of Physics

BANGLADESH UNIVERSITY OF ENGINEERING AND TECHNOLOGY

26 September 2020

The thesis titled “STRUCTURAL CORRELATION AND TUNABILITY OF MAGNETIC AND ELECTRIC PROPERTIES OF MANGANESE DOPED COBALT FERRITE NANOPARTICLES” submitted by Md. Ziaul Ahsan, Roll No.:1015144006P, Session: October 2015, has been accepted as satisfactory in partial fulfillment of the requirement for the degree of Doctor of Philosophy in Physics on 26 September 2020.

 BOARD OF EXAMINERS

1. Dr. Md. Feroz Alam Khan
Professor (Supervisor)
Department of Physics, BUET, Dhaka
Chairman
2. Dr. Md. Rafi Uddin
Professor and Head
Department of Physics, BUET, Dhaka
Member
(Ex-officio)
3. 
Dr. Jiban Podder
Professor
Department of Physics, BUET, Dhaka
Member
4. 
Dr. Md. Farhad Mina
Professor
Department of Physics, BUET, Dhaka
Member
5. 
Dr. Mohammad Abdul Basith
Professor
Department of Physics, BUET, Dhaka
Member
6. 
Dr. Engr. Sheikh Manjura Hoque
Division Head
Material Science, BAEC
Member
7. 
Dr. Supriya Saha
Professor
Department of Physics
University of Dhaka, Dhaka-1000
Member
8. 
Dr. G.M. Bhuiyan
Professor
Department of Theoretical Physics
University of Dhaka, Dhaka-1000
Member (External)

CANDIDATE'S DECLARATION

It is hereby declared that this thesis or any part of it has not been submitted elsewhere for the award of any degree or diploma.

A handwritten signature in black ink, consisting of stylized letters 'ZA' followed by a long horizontal stroke extending to the right.

Md. Ziaul Ahsan

**DEDICATED TO
MY BELOVED WIFE AND SON**

Acknowledgement

I would like to sincerely thank my supervisor Prof. Dr. Md. Feroz Alam Khan who guided me to find a subject for the thesis and gave me a perfect description of the subject, which was a great help later for finding my way to do my research. Again thanks, Prof. Dr. Md. Feroz Alam Khan for giving his valuable time and observing the process of the study and giving me directions and recommendations. I am also grateful to all the members of my doctoral committee for giving me time to time their valuable observations and way out the problems encountered in the experimentation. Furthermore, I am very thankful to Lt Col BrajalalSinha, Maj Mahabub Shaha, Lecturer RumanaMaleque of the department of physics, MIST, for their wholehearted cooperation and support in my research work. I am very grateful to Md Aminul Islam, TanzinaTabassum, Asst. Prof. Tofayel, who has directly rendered their cooperation and assistance in the characterization of my investigated samples. I am also thankful to the lab assistants of the physics lab, MIST, who have helped me in the preparation of my investigated samples. I am thankful to the International Science Programs (ISP), Uppsala University, Sweden for financial and technical support. I am also thankful to the Department of Glass and Ceramics Engineering (GCE), Bangladesh University of Engineering and Technology (BUET), and to the Department of Physics, Military Institute of Science and Technology (MIST) for their experimental support. Thanks to the Head of the Department, teachers, staff, and assistants who have inspired me and helped me in their capacity. All my acknowledgments and thanks are expressed to my teachers, lab mates (M. A. Islam, Asma Akhter Bally, Tanzina Tabassum, Md. Tofayel Hossain), and my family who were supportive and encouraged in my research.

Finally, I would like to convey my sincere gratitude to the command of MIST and the Bangladesh Navy for allowing me to carry out my research.

Abstract

In the present work, three systems of manganese (Mn) doped cobalt ferrite nanoparticles were synthesized by the planetary ball milling technique with the composition formula $\text{Co}_{1+x}\text{Mn}_x\text{Fe}_{2-x}\text{O}_4$, $\text{Co}_{1-x}\text{Mn}_x\text{Fe}_2\text{O}_4$ and $\text{CoMn}_x\text{Fe}_{2-x}\text{O}_4$, where $0.125 \leq x \leq 0.5$ in step 0.125. The synthesized samples were characterized by their structural, electrical, and magnetic properties. The crystallinity and single-phase cubic spinel structure at the calcination temperature 900°C are confirmed by their XRD patterns. The decreasing trend in their lattice constant may be attributed to the relatively smaller ionic size of dopant (Mn). The enlarged crystallite size is observed $\text{Co}_{1+x}\text{Mn}_x\text{Fe}_{2-x}\text{O}_4$ due to elevated calcination temperature. The Field Emission Scanning Electron Microscopic images show agglomerated particles with average particles sizes in the nanoscaled range. The frequency response of ε' of all three systems' demonstrates the ferrimagnetic behavior at room temperature. The appearance of peaks in the $\varepsilon''(f)$ spectra of $\text{Co}_{1+x}\text{Mn}_x\text{Fe}_{2-x}\text{O}_4$ show the grain boundary contribution to their resistivity that causes the thermal energy dissipation. This behavior of ε'' may make the sample suitable for use in hyperthermia or related research in medical science. The increasing trend of the activation energy, E_a in $\text{CoMn}_x\text{Fe}_{2-x}\text{O}_4$ with Mn content implies a spin disorder phenomena leading to a possible ferrimagnetic-to-paramagnetic phase transition and thus tune the material to behave as a soft magnetic material above the room temperature. The temperature dependence of dc resistivity, ρ of $\text{Co}_{1+x}\text{Mn}_x\text{Fe}_{2-x}\text{O}_4$ system exhibits the semiconducting behavior above the room temperature that make them suitable for the possible applications in thermoelectric devices. A characteristic temperature, T_{char} is marked at around 162K in $\text{Co}_{1+x}\text{Mn}_x\text{Fe}_{2-x}\text{O}_4$ system that sets a boundary between long-range mobility and short-range mobility of charge carriers/ions. A crossover frequency is noticed at around 58kHz in the spectra of magnetic modulus of $\text{Co}_{1+x}\text{Mn}_x\text{Fe}_{2-x}\text{O}_4$. Above this crossover frequency, magnetic modulus is correlated to the crystallite/grain size. The Nyquist plot of the electric modulus separates the contribution of n-type and p-type ions in the conductivity of $\text{Co}_{1-x}\text{Mn}_x\text{Fe}_2\text{O}_4$. Comparatively, an enhanced ac permeability is observed in $\text{Co}_{1-x}\text{Mn}_x\text{Fe}_2\text{O}_4$ that make this system suitable to be used in high frequency applications. A phase transition between ferromagnetic to spin-glass state is observed in $\text{Co}_{1+x}\text{Mn}_x\text{Fe}_{2-x}\text{O}_4$ and $\text{CoMn}_x\text{Fe}_{2-x}\text{O}_4$ systems in the low temperature regime.

Contents

Acknowledgement	v
Abstract	vi
Contents	vii
List of Figures	ix
List of Tables	xiv
List of Symbols	xvi
CHAPTER-I: INTRODUCTION	1 - 5
1.1 Introduction	1
1.2 Motivation	4
1.3 Objective of Research Work	5
1.4 Specific Aims of Research Work	5
1.3 Sequence of Thesis	5
CHAPTER-II: LITERATURE REVIEW	6 - 29
2.1 Introduction	6
2.2 Surveyed literatures	6
2.3 Findings on literature review	26
2.4 Research spaces and scopes	28
CHAPTER-III: EXPERIMENTAL DETAILS	30 - 51
3.1 Introduction	30
3.2 Synthesis technique	30
3.3 Characterization technique	40
CHAPTER-IV: RESULT AND DISCUSSION: $Co_{1+x}Mn_xFe_{2-x}O_4$	52 – 124
4.1 Introduction	52
4.2 Non-stoichiometric composition $Co_{1+x}Mn_xFe_{2-x}O_4$	52
4.2.1 Structural properties	52
4.2.2 Magnetic properties	61

4.2.3	Electric properties	74
4.3	Stoichiometric composition $CoMn_xFe_{2-x}O_4$	90
4.3.1	Crystallographic and morphological analysis	90
4.3.2	Magnetic properties	93
4.3.3	Electric properties	99
4.4	Stoichiometric composition $Co_{1-x}Mn_xFe_2O_4$	109
4.4.1	Crystallographic and Morphological Analysis	109
4.4.2	Magnetic properties	112
4.4.3	Electric properties	117
4.5	Comparison of Three Systems on the Manifested Properties	124
CHAPTER-V: CONCLUSION AND RECOMMENDATION		125-126
5.1	Conclusion	125
5.2	Recommendations	126
REFERENCES		127-139
APPENDICES		A-1 - 5

List of Figures

Fig. No	Figure Caption	Page No
1.1	(a) The unit cell of the inverse (B) [AB] O ₄ spinel contains 8 sublattices (b) Schematic diagram of Cobalt ferrite	03
3.1	Pictorial flow chart of sample preparation method by solid-state reaction route using ball milling	31
3.2	Ball mill and its cross-section picture(MSK-SFM-1 benchtop planetary ball mill)-step-1-2	33
3.3	Schematic drawing of planetary ball milling machine	34
3.4	(a) Particle size as a function of ball milling time (b) Unit cell volume as a function of particle size	34
3.5	WiseTherm Furnace used for the calcination of the ball-milled powders in step-3	36
3.6	The pelletization in the form of pellet/disc and toroid in step-4	36
3.7	Sintering of pellet/disc and toroid shaped samples in the WiseTherm furnace in step-5	37
3.8 (a)	(a) The four basic elements of materials science and engineering, (b) General fabrication the pattern of sintered parts	38
3.9	Basic phenomena occurring during sintering under the driving force for sintering, $\Delta(\gamma A)$	39
3.10	(a) The schematic diagram of Bragg's diffraction for X-ray (b) EMPYREAN PANalytical X-ray diffractometer	43
3.11	(a) The ray diagram of FESEM, (b) FESEM model JSM-7600F	44
3.12	(a) The block diagram of VSM, (b) Homemade VSM	46
3.13	(a) Virgin curve, (b) Hysteresis loop of ferromagnetic material	47
3.14	(a)The Waynekerr Impedance Analyzer 6500B (b)Toroid and disc-shaped sample for permeability measurement	48
3.15	4-probe technique to measure resistivity	50
3.16	Experimental setup the measurement of field dependent resistivity	50

4.1	Rietveld refined X-ray diffraction (XRD) patterns of non-stoichiometric manganese doped cobalt ferrite nanoparticles at $x=0.125, 0.250, 0.375, 0.500$	53
4.2	FESEM micrographs of $\text{Co}_{1+x}\text{Mn}_x\text{Fe}_{2-x}\text{O}_4$ at $x=0.125, 0.250, 0.375, 0.500$	56
4.3	Particle size distribution histogram of $\text{Co}_{1+x}\text{Mn}_x\text{Fe}_{2-x}\text{O}_4$ at $x=0.125, 0.250, 0.375, 0.500$	57
4.4	EDS spectrum of $\text{Co}_{1+x}\text{Mn}_x\text{Fe}_{2-x}\text{O}_4$ at $x=0.125, 0.250, 0.375, 0.50$	58
4.5	X-ray diffraction patterns for the representative samples of $\text{Co}_{1+x}\text{Mn}_x\text{Fe}_{2-x}\text{O}_4$ with concentration level, $x = 0.125$ at different calcination temperatures ($T_{\text{Calcination}}$)	59
4.6	FESEM micrographs for the representative sample of $\text{Co}_{1+x}\text{Mn}_x\text{Fe}_{2-x}\text{O}_4$ with $x = 0.125$ at milling time (MT) (a) MT = 8 h (b) 12 h	60
4.7	(a) Real part of complex permeability, μ' as a function of frequency for the samples of $\text{Co}_{1+x}\text{Mn}_x\text{Fe}_{2-x}\text{O}_4$, (b) Imaginary part of complex permeability, μ'' as a function of frequency for the samples of $\text{Co}_{1+x}\text{Mn}_x\text{Fe}_{2-x}\text{O}_4$	62
4.8	(a) Normalized real part, μ' as a function of temperature (T) above room temperature (323K – 573K), (b) Normalized real part, μ'' as a function of temperature (T) below room temperature (77K – 245K) for the samples of $\text{Co}_{1+x}\text{Mn}_x\text{Fe}_{2-x}\text{O}_4$ with $\text{Mn}(x) = 0.5$ at different selected frequencies	63
4.9	(a) M_m' vs $\log f$ curves (b) Extended view of M_m' vs $\log f$ (c) M_m'' vs $\log f$ curves (d) Nyquist plot at room temperature for the samples of $\text{Co}_{1+x}\text{Mn}_x\text{Fe}_{2-x}\text{O}_4$	65
4.10	(a) Imaginary part M_m'' as a function of frequency at selected temperature, (b) Relaxation time, τ_{max} as a function of temperature (T) in the temperature range 77K – 245K for the sample of $\text{Co}_{1+x}\text{Mn}_x\text{Fe}_{2-x}\text{O}_4$ with $\text{Mn}(x) = 0.5$	67
4.11	(a) Initial magnetization curves for the non-stoichiometric composition (b) Hysteresis curves for the non-stoichiometric composition at room temperature in the magnetic field range 0 – 4 kOe	68
4.12	Hysteresis curves in the temperature regime 77 – 300K (left: non-fitted and right: fitted) for the samples (a) $x = 0.125$, (b) $x = .375$, (c) $x = 0,5$	69

4.13	(a) $M - T$ curves (b) $H_C - T$ curves (c) $M_R/M_S - T$ curves for the investigated samples of composition, $Co_{1+x}Mn_xFe_{2-x}O_4$ in the temperature range 77K – 300K (d) $T_c - x$ curve of $Co_{1+x}Mn_xFe_{2-x}O_4$	71
4.14	(a) $1/\chi - T$ curves (b) $\theta - x$ curves for investigated samples of composition $Co_{1+x}Mn_xFe_{2-x}O_4$	72
4.15	(a) Real part of complex dielectric constant, ϵ' as a function of frequency (b) Imaginary part of complex dielectric constant, ϵ'' as a function of frequency at room temperature in the frequency range 1 kHz – 1MH	74
4.16	(a) Real part of dielectric constant, ϵ' as a function of temperature (b) Imaginary part of dielectric constant, ϵ'' as a function of temperature at selected frequency 10 kHz in the low-temperature regime (77K – 300K)	76
4.17	(a) Real part of dielectric constant, ϵ' as a function of temperature (b) Imaginary part of dielectric constant, ϵ'' as a function of temperature for $x = 0.125$ of $Co_{1+x}Mn_xFe_{2-x}O_4$ in the high-temperature regime 310K – 400K	77
4.18	(a) $M' vs \log f$ curves (b) $M'' vs \log f$ curves at room temperature for the representative samples of $Co_{1+x}Mn_xFe_{2-x}O_4$	79
4.19	(a) $M'/M'_{Max} vs f/f_{Max}$ curves (b) $\tau_{Max} vs f$ curves samples of $Co_{1+x}Mn_xFe_{2-x}O_4$ for $x = 0.125$ in the temperature range 77K – 300K	82
4.20	(a) AC resistivity as a function of frequency at room temperature (RT) (b) Normalized ac resistivity for the sample of $x = 0.125$ as a function of frequency at RT and liquid nitrogen temperature (LNGT) in the frequency range 1kHz – 1MHz	83
4.21	AC resistivity as a function of temperature for the sample of $x = 0.125$ (a) at selected frequencies 100Hz, 1kHz, 10kHz, 100kHz and 1MHz (b) at selected frequencies 100kHz (inset 1MHz) (300K-400K)	84
4.22	a) Resistivity as a function of temperature (b) Magnetoresistance, MR% as a function of the magnetic field (c) Normalized resistivity as a function of the magnetic field at RT, and (d) Rate of change of resistivity to the magnetic field ($\Delta\rho/\Delta H$) of the investigated sample with $x = 0.125$	87
4.23	$Z vs \log f$ curves (b) $X vs \log f$ curves (c) $X vs R$ curves at room temperature for the samples of $x = 0.125, 0.25, 0.375, 0.5$ of $Co_{1+x}Mn_xFe_{2-x}O_4$	87

4.24	The Cole-Cole plot for (a) the sample of MT 8h (b) for the sample of MT 12h of the composition $\text{Co}_{1+x}\text{Mn}_x\text{Fe}_{2-x}\text{O}_4$ at $x = 0.125$	89
4.25	(a) X-ray diffraction patterns (b) FE-SEM Micrographs for the samples of $\text{CoMn}_x\text{Fe}_{2-x}\text{O}_4$ within content $(x) = 0.125, 0.25, 0.375$ and 0.5	90
4.26	(a) Real part (b) Imaginary part of ac permeability as a function of frequency for $\text{CoMn}_x\text{Fe}_{2-x}\text{O}_4$ sample with different Mn content (x) at room temperature in the frequency range $100 \text{ Hz} - 100 \text{ MHz}$	93
4.27	Normalized real part of permeability, μ' as a function of temperature for the samples of Mn content $(x) = 0.125, 0.375,$ and 0.5 at different selected frequencies in the low-temperature regime	95
4.28	(a) M_m' vs $\log f$ curves (b) M_m'' vs $\log f$ curves for the samples of $\text{CoMn}_x\text{Fe}_{2-x}\text{O}_4$ at room temperature (RT)	96
4.29	(a) Hysteresis Curves (b) Initial M-H Curves for the sample of $\text{CoMn}_x\text{Fe}_{2-x}\text{O}_4$ with Mn content $(0 \leq x \leq 0.5)$ at RT	98
4.30	(a) Relative dielectric constant, ϵ_r (b) D-factor as a function of frequency for the sample of $\text{CoMn}_x\text{Fe}_{2-x}\text{O}_4$ at room temperature in the frequency range $100 \text{ Hz} - 10 \text{ MHz}$	99
4.31	Graphs for (a) Real part, ϵ' and (b) Imaginary part, ϵ'' of dielectric constant as a function of the temperature for the sample of $\text{CoMn}_x\text{Fe}_{2-x}\text{O}_4$ at Mn content, $x = 0.125$	100
4.32	Ac resistivity, ρ_{ac} as a function of frequency for the sample of $\text{CoMn}_x\text{Fe}_{2-x}\text{O}_4$ at room temperature in the frequency range $100 \text{ Hz} - 1 \text{ MHz}$	102
4.33	AC Conductivity, σ_{ac} as a function of inverse temperature $(1000/T)$ for the sample of composition $\text{CoMn}_x\text{Fe}_{2-x}\text{O}_4$ at selected frequency of 10 kHz over the temperature range $(300 - 573) \text{ K}$	103
4.34	(a) Real part, M' , (b) Imaginary part, M'' of electric modulus as a function of frequency, (c) Nyquist plot (M'' vs. M') for CFM system at RT in the frequency range $100 \text{ Hz} - 1 \text{ MHz}$, (d) Equivalent circuit	106
4.35	:(a) Normalized real part of electric modulus, M' (b) Normalized imaginary part of electric modulus, M'' as a function of frequency $(100 \text{ Hz} - 20 \text{ MHz})$ at selected temperature $423 \text{ K}, 473 \text{ K},$ and 523 K for representative sample of CM system with Mn $(x) = 0.125$	108

4.36	(a) X-ray diffraction patterns (b) FE-SEM Micrographs for samples of the CMF system with Mn content (x) = 0.125, 0.25, 0.375 and 0.5	109
4.37	(a) Real part, μ' (b) Imaginary part, μ'' for the sample of $\text{Co}_{1-x}\text{Mn}_x\text{Fe}_2\text{O}_4$ at different Mn(x) in the frequency range 100Hz – 1MHz	113
4.38	(a) M_m' vs $\log f$ curves (c) M_m'' vs $\log f$ curves at room temperature for the samples of $\text{Co}_{1-x}\text{Mn}_x\text{Fe}_2\text{O}_4$	113
4.39	(a) M-H Curves (b) the variation of M_S and H_C as a function of Mn content (x) for the samples of $\text{Co}_{1-x}\text{Mn}_x\text{Fe}_2\text{O}_4$, within Mn content ($0 \leq x \leq 0.5$) at RT	115
4.40	(a) Initial M -H curves for the determination of μ_i (b) χ vs. H Curves for the samples of $\text{Co}_{1-x}\text{Mn}_x\text{Fe}_2\text{O}_4$ with different Mn content ($0 \leq x \leq 0.5$) at RT	117
4.41	AC resistivity for the samples of $\text{Co}_{1-x}\text{Mn}_x\text{Fe}_{2-x}\text{O}_4$ in the frequency range 100 Hz – 1MHz at room temperature (RT)	118
4.42	(a) Real part, ε' as a function of frequency on a logarithmic scale (b) Imaginary part, ε'' as a function of frequency on a logarithmic scale for the samples of $\text{Co}_{1-x}\text{Mn}_x\text{Fe}_{2-x}\text{O}_4$ at RT	119
4.43	AC conductivity for the samples of $\text{Co}_{1-x}\text{Mn}_x\text{Fe}_{2-x}\text{O}_4$ at RT in the frequency range 100 Hz – 10 MHz	120
4.44	(a) Real part, M' , (b) Imaginary part, M'' of electric modulus as a function of frequency, for the sample of $\text{Co}_{1-x}\text{Mn}_x\text{Fe}_2\text{O}_4$ at RT in the frequency range 100Hz–10MHz	121
4.45	Nyquist plot or electric modulus for the sample of $\text{Co}_{1-x}\text{Mn}_x\text{Fe}_2\text{O}_4$ at Mn content (a) x = 0.125 (b) x = 0.25 (c) x = 0.375, and (d) x = 0.5 in the frequency range 100Hz – 100MHz	123

List of Tables

Table No.	Table Caption	Page No
3.1	Matrix to highlight the spaces and scopes for further investigations	27
4.1	Different structural parameters of $\text{Co}_{1+x}\text{Mn}_x\text{Fe}_{2-x}\text{O}_4$ system at room temperature (RT)	54
4.2	Cation distribution of $\text{Co}_{1+x}\text{Mn}_x\text{Fe}_{2-x}\text{O}_4$ system as determined from Rietveld refined XRD patterns	55
4.3	Average particle sizes, particle diameter, and elemental composition of $\text{Co}_{1+x}\text{Mn}_x\text{Fe}_{2-x}\text{O}_4$ system at room temperature (RT)	58
4.4	Mass% and Estimated average particle size of the composition $\text{Co}_{1+x}\text{Mn}_x\text{Fe}_{2-x}\text{O}_4$ at $x = 0.125$	61
4.5	Resonance frequency, $f_{resonance}$ and relaxation time constant (τ) of $\text{Co}_{1+x}\text{Mn}_x\text{Fe}_{2-x}\text{O}_4$	66
4.6	Values of M_S , H_C , M_R and μ_i for the investigates samples of $\text{Co}_{1+x}\text{Mn}_x\text{Fe}_{2-x}\text{O}_4$ at room temperature (RT)	69
4.7	The magnetic parameters for samples of $\text{Co}_{1+x}\text{Mn}_x\text{Fe}_{2-x}\text{O}_4$ in the low temperature regime (77- 3K)	73
4.8	Relaxation time constant (τ) and activation energy, E_a for $x=0.125$ of $\text{Co}_{1+x}\text{Mn}_x\text{Fe}_{2-x}\text{O}_4$	78
4.9	Critical frequency (f_C), critical relaxation time constant (τ_C), characteristic frequency (f_{max}), relaxation time constant (τ_{Max}), and activation energy (E_a)	81
4.10	Different structural parameters of $\text{CoMn}_x\text{Fe}_{2-x}\text{O}_4$ as determined from the XRD patterns	91
4.11	Cation distribution of $\text{CoMn}_x\text{Fe}_{2-x}\text{O}_4$ as determined from Rietveld refinement of XRD patterns	92
4.12	Resonance frequency, $f_{resonance}$, and relaxation time constant (τ_m) and activation energy for $x=0.125$ of $\text{CoMn}_x\text{Fe}_{2-x}\text{O}_4$	97
4.13	The magnetic parameters of $\text{CoMn}_x\text{Fe}_{2-x}\text{O}_4$ (CFM) ferrite system at RT	98

4.14	Relaxation time constant (τ) for the sample of $\text{CoMn}_x\text{Fe}_{2-x}\text{O}_4$ with Mn (x) = 0.125 at RT	101
4.15	Values of E_a at 10 kHz for the investigated samples of $\text{CoFe}_{2-x}\text{O}_4$ composition	104
4.16	Characteristic frequency (f_{max}), relaxation time (τ), grain-boundary capacitance (C_{gb}), grain capacitance (C_g), grain-boundary resistance (R_{gb}) and grain resistance (R_g) for the investigated samples	107
4.17	Different structural parameters of $\text{Co}_{1-x}\text{Mn}_x\text{Fe}_2\text{O}_4$ as determined from the XRD patterns	110
4.18	Cation distribution of $\text{Co}_{1-x}\text{Mn}_x\text{Fe}_2\text{O}_4$ (CFM) system as determined from Rietveld refinement of XRD patterns	111
4.19	Resonance frequency, $f_{resonance}$ and relaxation time constant (τ) of $\text{Co}_{1-x}\text{Mn}_x\text{Fe}_{2-x}\text{O}_4$	114
4.20	The magnetic parameters for the samples of $\text{Co}_{1-x}\text{Mn}_x\text{Fe}_2\text{O}_4$ at room temperature (RT)	116
4.21	Characteristic frequency (f_{max}) and relaxation time (τ)	122
4.22	Comparison of three compositions on significant demonstrated properties	124

List of Symbols/abbreviations

Symbols	Usual Meaning
Co	Symbol for Cobalt
Mn	Symbol for Manganese
Fe	Symbol of Iron
x	Signifies Mn concentration/concentration levels at weight percentage
Å	Angstrom (unit of dimension) = 10^{-10} m
K	Kelvin scale of temperature
AC	Alternating current
nm	Nanometer (unit of dimension) = 10^{-9} m
emu g ⁻¹	Electromagnetic unit per gram (unit of magnetization)
XRD	X-ray diffraction
FESEM	Field Emission Electron Microscopy
M (H)	Magnetization as a function of magnetic field
M _S	Saturation Magnetization
M _R	Remnant Magnetization
H _C	Coercivity
μ_i	Initial Permeability
n _B	Magnetic moment per formula unit in Bohr Magneton
μ'	Real part of ac permeability
μ''	Imaginary part of permeability
χ	Susceptibility
tan δ	Loss factor (Corresponds to both dielectric and magnetic loss)
ϵ'	Real part of permittivity
ϵ''	Imaginary part of permittivity

ϵ_r	Relative dielectric constant
C	Capacitance
Z	Impedance
X	Reactance
R	Resistance
ρ_{ac}	AC resistivity
σ_{ac}	AC Conductivity
f_o	Resonance frequency
τ	Relaxation time constant
f_c	Critical frequency
f_{max}	Maximum characteristic frequency
M'	Real part of electric modulus
M''	Imaginary part of electric modulus
M_m'	Real part of magnetic modulus
M_m''	Imaginary part of magnetic modulus
$\Delta M(T)$	Change of magnetization as a function of temperature
ΔT	Change in temperature
ΔH	Change in magnetic field
ΔS	Change in entropy
ΔS_m	Change in magnetic entropy
ΔS_{lat}	Change in entropy due to lattice vibrations
ΔS_{elec}	Change in entropy due to electronic contribution

CHAPTER – I

INTRODUCTION

1.1. Introduction

Ferrites are the attractive materials for basic research and technological applications because of their unique electric and magnetic properties[1-2]. Nanotechnology has initiated a renewed interest in spinel ferrites to explore the possibility of their applications in a wider range. Nanomaterials exhibited enhanced properties in comparison to their bulk counterpart since in nanocrystalline material the physical properties are predominantly controlled by the grain boundaries than by the grains [3-4]. Nanoparticles of spinel ferrite have been extensively used in a wide range of applications. Spinel ferrite can be represented by the general formula AB_2O_4 in which A and B are the tetrahedral and octahedral sites respectively and filled up by the metal ions. They are of three types such as normal, inverse, and mixed spinels. Among the spinel ferrites, cobalt ferrite is a special one owing to its unique properties like high Curie temperature, high coercivity, high magnetocrystalline anisotropy, and moderate saturation magnetization, as well as its excellent chemical stability, large Kerr effect, and Faraday rotation [5]. This cobalt ferrite is of inverse spinel structure wherein relatively larger oxygen ions (O^{2-}) form cubic closed pack (*ccp*) lattice. Its tetrahedral (A) and octahedral (B) sites formed by the oxygen ions (O^{2-}) are occupied by metal ions (Fe^{3+} and Co^{2+} ions). The Tetrahedral (A) site is occupied by Fe^{3+} ions and the Octahedral (B) site by Fe^{3+} and Co^{2+} ions in equal proportionate as depicted in Fig. 1.1[6]. The degree of this inversion in its structure mostly depends on synthesise techniques and heat treatment. In the family of ferrites, cobalt ferrite has attracted researches, materials scientists, technologists, and engineers for synthesizing new properties because a wide variety of total solid solutions is possible in this cobalt ferrite keeping its basic structure almost unchanged. As such intensive investigations have been performed on cobalt ferrites over the years to optimize them in diversified applications. The use of nanoparticles has increased in recent times because of their interesting unusual and superior properties that are different from their bulk material. Moreover, magnetic nanoparticles are found to gain increasing importance because of their new

applications in the field of medical science, environmental, catalysts, and sensors [7]. In this respect, ferrimagnetic material cobalt ferrites seems to play a significant role because of their possibility to be synthesized by doping transition or rare earth elements. Also, because of fifty-seven oxidation states of manganese, it may be a good choice as a dopant to tune and tailor the properties of this cobalt ferrite both in bulk and nano dimension. Accordingly, efforts have already been made to substitute *Co* or *Fe* by metal ions for offering the ability to tailor the structural, magnetic, and electrical properties in a controlled manner by synthesizing them through various techniques. Subsequently, the recent literature survey reveals some important facts: (i) the dielectric properties are strongly affected by the cation redistributions with the increase of *Mn* concentration in $Co_{1-x}Mn_xFe_2O_4$ due to the generation of heterogeneity that leading to improve their resistive property, and their ac electrical properties are also strongly frequency-dependent [8, 9]. (ii) The frequency-dependent ac impedance measurement of $CoMn_xFe_{2-x}O_4$ makes it possible to use in frequency band filter design as reported in the literature [10]. (iii) Low level ($x = 0.1$ and 0.2) substitution of *Mn* in $CoFe_{2-x}Mn_xO_4$ induces a residual phase Fe_2O_3 and MnO_2 and increases the density of intergranular pores and the grain size but a further increase of *Mn* concentration decreases the grain size with the same porosity [11]. (iv) The formation of two phases for $x > 1$ in the non-stoichiometric compound $Co_xFe_{3-x}O_4$ ($x = 1$ to 2) is observed, where the coercivity increases but magnetization decreases with the increase of *Co* concentration [12]. However, very seldom investigations have been performed on their electromagnetic properties for high-frequency applications, and also ball milling technique was found to seldom use in synthesizing nonmaterial despite its ability to control the particle size by changing milling time. In the present work, cobalt ferrite ($CoFe_2O_4$) has been chosen as a parent material for this research by manganese (*Mn*) doping in three systems with a composition formula $Co_{1-x}Mn_xFe_2O_4$ (CMF), $CoMn_xFe_{2-x}O_4$ (CFM) and $Co_{1+x}Mn_xFe_{2-x}O_4$ (CFMZ) for different concentration levels x in the weight percent $x = 0.125, 0.250, 0.375, 0.5$. Among these three systems, the first two are the stoichiometric compositions and the last one is non-stoichiometric composition. The samples of this research work were prepared through the conventional solid-state reaction route by using the planetary ball milling technique. This ball milling technique has been chosen to synthesize nanoparticles of this research work to

provide the opportunity for investigating the effect of particle size on structural, magnetic, and electric properties. The prepared samples were characterized by structural, magnetic, and electric properties to establish their correlation and in a quest to find their suitability in the high frequency and other probable promising applications. To investigate their structural properties, crystallographic analysis, morphological and elemental studies were carried out by using X-ray diffraction patterns (XRD), field emission scanning electron micrographs (FESEM), and energy dispersion spectrum (EDS). The experimental findings on electromagnetic properties are found to be more significant for the non-stoichiometric composition $Co_{1+x}Mn_xFe_{2-x}O_4$ (CFMZ) and thereby it is suggested that this non-stoichiometric composition of manganese (*Mn*) doped cobalt ferrite nanoparticles be more suitable in the high frequency and microwave device applications. That is why the non-stoichiometric composition as designated by the CFMZ system has come in the major focus of my research work. However, the scientific rigors on structural, magnetic, and electric behavior of these three compositions have been presented in this thesis paper manifesting their promising outcomes to explore their suitability in other diversified fields of applications along with some recommendations for further investigations.

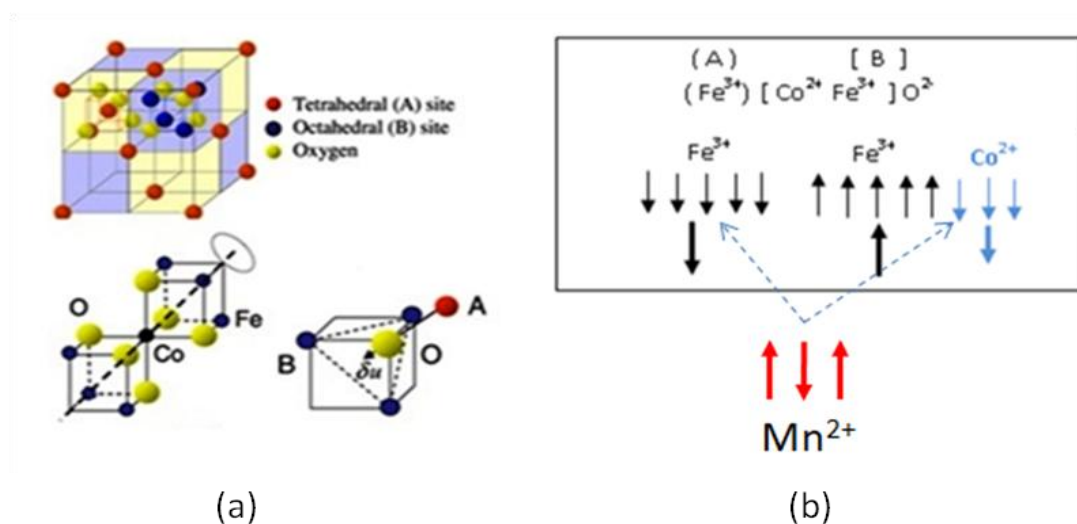


Fig. 1.1: (a) The unit cell of the inverse (B) [AB] O₄ spinel contains 8 sublattices
(b) Schematic diagram of Cobalt ferrite

1.2 Motivation

The following motivation factors have encouraged me to do research on three systems of manganese doped cobalt as mentioned above in a quest to explore and exploit their suitability in high frequency and sensor applications.

- i. There are a variety of ferrites, among them; cobalt ferrites have come in the main focus for intensive researches over the decades. This is because of the wide variety of total solid solutions that can be achieved in the cobalt ferrite by doping using transition or rare-earth elements that manifest tuned and tailored properties while maintaining its basic structure almost unchanged.. Besides, around fifty-seven oxidation states of manganese are considered to be used as a good and versatile dopant to tune or tailor the material in a variety of properties
- ii. In the family of ferrites, cobalt ferrite is unique with an inverse spinel structure. This inversion mostly depends on synthesis techniques and thermal treatment.
- iii. The nanoparticles of cobalt ferrites gained gradual importance because of their interesting unusual and superior properties over their bulk counterparts. As such, recently Cobalt ferrites doped with metallic ions have received renewed attention across the world to optimize them for the application in medical science, catalysts, environmental and sensors. These applications are mostly based on structural, magnetic and electrical behaviors and their tuning by adjusting the substitution level of dopant, sintering temperature, and particle size.
- iv. Moreover, the change in the particle size is also possible with the planetary ball milling technique by changing milling time during the synthesizing of nanoparticles, which is also cost-effective because a large number of nanoparticles may be possible to synthesize by this technique.

1.3 Objective of Research Work

The objective of this research work is to understand structural, electrical, and magnetic properties of the newly synthesized material for exploiting and exploring them in diversified applications, in particular, high frequency and sensor devices.

1.4 Specific Aims of Research Work

To achieve the aforesaid objective, the specific aims are as follows:

- i. To synthesize the stoichiometric and non-stoichiometric samples of manganese (Mn) doped cobalt ferrite nanoparticles with composition $\text{Co}_{1-x}\text{Mn}_x\text{Fe}_2\text{O}_4$, $\text{CoMn}_x\text{Fe}_{2-x}\text{O}_4$, and $\text{Co}_{1+x}\text{Mn}_x\text{Fe}_{2-x}\text{O}_4$, where, $0 \leq x \leq 0.5$ using the conventional solid-state reaction route.
- ii. To investigate the effects of Mn doping on structural, magnetic, and electric properties and establish their correlation for optimization of device performances.
- iii. To study the frequency response and temperature dependence of complex permeability and permittivity and hence find a suitable frequency band to maximize the device performance.
- iv. To investigate the effect of size and calcination/sintering temperature on magneto-transport properties to find their suitability in the sensor applications.

1.5 Sequence of Thesis

In this thesis, the procedures of synthesizing nanoparticles of the investigated samples and experimentation with their findings and discussion are presented in a logical sequence:

- i. Chapter – I: Introduction
- ii. Chapter – II: Literature Review
- iii. Chapter – III: Experimental Details
- iv. Chapter – IV: Result and Discussion
- v. Chapter – V: Conclusion

CHAPTER – II

LITERATURE REVIEW

2.1. Introduction

Literature' review is an important aspect and first-hand method for deriving the research objective to the discovery and development of new materials suitable for diversified applications. Intensive research works are being continued with different objectives and aim across the world. Among the research findings on the subject material, untouched or unaddressed or non-conclusive or conspicuous issues on properties need to bring out for further investigations, where literature' review plays its role. As such results of recent researches on the composition of Cobalt ferrite nanoparticles by surveying related available works of literature have been discussed in this chapter for finding the unresolved or aforesaid any issues required to further investigate for the purpose.

2.2. Surveyed literatures

Adeela Narian et al [13] reported that 20% Co substituted with Mn^{2+} ions (AFM) in $CoFe_2O_4$ ($Co_{0.8}Mn_{0.2}Fe_2O_4$) ferrite, prepared using chemical Co-precipitation method, exhibit crystalline Size – 14.33 nm, lattice constant – 8.439 Å (L) – 3.654 Å, [L] - 2.983 Å, A-O – 1.914 Å, B-O – 2.060 Å and X-ray density – 5.167 gm cm⁻³ from XRD pattern and confirmed the single-phase inverse spinel structure without any impurity. Hoping and bond lengths have also been calculated using the corresponding Stanley's equations. So, there is scope to investigate the structural parameters (lattice constant, X-ray density, hoping, and bond lengths) with different substitution levels of Mn in Cobalt ferrite for Co, which might provide the correlation between lattice constant and magnetic moment and thus ability to tune magnetic properties. Furthermore, it is reported that the shift in blocking temperature T_b and bifurcation temperature T_{irr} towards lower temperature with the applied magnetic field in ZFC-FC cycles typically identifies the superparamagnetism below T_{irr} and strong dipolar interactions among the particles. The increase in coercivity and saturation magnetization of the sample is observed when the temperature goes down to 5 K. This increase of coercivity at low temperature happens to occur due to

an increase of magnetic anisotropy and particles scattering in the direction of the anisotropy field. In the nanoparticles' (NPs), the effect of thermal fluctuations of blocked moments across the anisotropy barrier is responsible for the enhancement of coercivity at low temperatures. Therefore, with decreasing temperature, the reduced thermal fluctuations tend to make magnetic moment isotropic and causing an increase of coercivity of the system. At room temperature, the magnetization of the samples depends mostly on size effects. The temperature dependence of magnetization had been explained by the formula, $M_s(T) = M_s(0) - C \left[e^{-\frac{E_1}{k_B T}} + e^{-\frac{E_2}{k_B T}} \right]$, where $M_s(T)$ is the temperature-dependent magnetization, $M_s(0)$ the magnetization at $T = 0K$, C is constant ($M_s(0)/Nn$), depending on the number of modes (N), and occupancy state (n), E_1 and E_2 denote energy levels and k_B the Boltzmann constant. The shift in the spin-wave spectrum relative to temperature alters the population in magnetic energy levels and resultantly, magnetic response increases. Hence, the magnetic moment per unit formula (n_B) at different temperature had been calculated from the equation, $n_B = \frac{M \times M_s}{5585}$, where, M is the molecular weight of the nanoparticle and M_s is the saturation magnetization, measured at different temperatures. The magnetization is showed ferromagnetic nature. The anisotropy had also been calculated using the equation $H_C = \frac{K_{eff} \times 0.96}{M_s}$, where H_C is the coercivity and M_s the saturation magnetization at a particular temperature. Hence, the magnetic parameters such as coercivity, saturation magnetization, magnetic moments, and anisotropy constant were found to increase with the decrease in temperature below room temperature due to the dominance of anisotropy energy over the thermal energy as the temperature of the system drops. The high magnetic properties of the sample suggested that its nanoparticles are suitable for applications in spintronics. So the analysis showed that the magnetic properties have been tuned as a function of temperature and externally applied magnetic field only for particular substitution level of Mn for Co below the room temperature. So, there are rooms for further analysis with different substitution level ($x = 0.125, 0.250, 0.375$ and 0.500) to study the dopant content (Mn) dependency, which might provide the tuning ability on to T_B and T_{irr} to control the superparamagnetic behavior of Mn substituted Co nanoferrites closer to the room temperature. Sheena Xavier et al, [14] showed that all the samples of $CoDy_xFe_{2-x}O_4$

to exhibit simple cubic spinel when the XRD patterns compared with the standard data for cobalt ferrite (JCPDS PDF card No. 22-1086) only the small peaks corresponded to the residual phase for the samples with higher dysprosium content. It is also reported that the crystallite size, the lattice constant, X-ray density, and porosity of $\text{CoDy}_x\text{Fe}_{2-x}\text{O}_4$ increase with the substitution of Dy^{3+} . The increase in lattice constant of Cobalt ferrite for $x = 0.0 - 0.2$ is attributed to the replacement of smaller Fe^{3+} ions (0.67\AA) at the octahedral site by the larger Dy^{3+} ions (0.91\AA). A slight decrease in the lattice parameter is noticed when the dysprosium content exceeds 0.2, which is an indication of the solubility limit of Dy^{3+} ions in the spinel lattice. Beyond this limit, the redundant Dy^{3+} ions cannot enter the spinel lattice and lead to the formation of the DyFeO_3 phase on the grain boundaries. Thus with higher dysprosium content, the secondary phase formation hinders the expansion of lattice with the result that further grain growth is inhibited. The porosity depends on several parameters such as preparation method, grain size, sintering temperature, and density. The X-ray density increases with the dysprosium content, which is correlated with the increase of the atomic weight of Dy^{3+} substituted for Fe^{3+} of lower atomic mass. This increased the porosity of this composition. The saturation magnetization (M_s), coercivity (H_c), and remnant ratio (M_R/M_s) are reported. The decrease in M_s with Dy content is attributed to the weakening of A-B interactions. Three types of interactions are possible between the unpaired electrons of ions occupying the A and B sites. The net magnetic moment in a ferrimagnetic material is the difference of magnetic moments between B and A sublattices. Due to large ionic radii, Dy^{3+} ions are substituted on the B-site of spinel lattice. Thus the substitution of Fe^{3+} ions by Dy^{3+} ions decreases Fe^{3+} - Fe^{2+} interactions and reduces the magnetic moment in B sites, causing M_s to decrease. A significant reduction in coercivity and remanence is noticed in doped samples with concentration $x \geq 0.2$. The decrease in coercivity is reported due to the increase in the crystallite size of the samples with dysprosium concentration. The remanent ratio is the characteristics parameter and it is the ease with the magnetization direction reorients to the nearest easy axis after the removal of the applied field. It decreases from 0.44 to 0.08 with doping and this can be related to the decrease in anisotropy of the crystal lattice by Dy substitution. The considerable reduction in the magnetic hysteresis loss can be attributed to the grain growth and reduced magnetocrystalline anisotropy. Mariano M. et al [15] reported

that $Fe_{2-x}CoSm_xO_4$ nanoparticles are of the inverse spinel structure for Sm^{3+} ($x = 0 - 0.2$). But for higher content of Sm^{3+} ($x = 0.3 - 0.5$) other stable phase appears, which is $FeSmO_3$ perovskite phase. The lattice constant a , of non-calcined particles, showed to oscillate for large amounts of Sm^{3+} ($x = 0.4 - 0.5$) with a slight decrease but for calcined particles to decrease with Sm^{3+} content when increases further than 0.1 ($x > 0.1$). This effect has been attributed to the binding energy between Sm^{3+} and O^{2-} which is higher than the binding energy between Sm^{3+} and Fe^{3+} . Thus with large amounts of Sm^{3+} and calcined temperature $800^\circ C$ the perovskite phase $FeSmO_3$ started to segregate. This second phase compresses the spinel structure and decreases the lattice parameter, average crystallite size, and particle size with an increase of Sm content. It is also reported that for all the composition ($x=0.0 - 0.5$), M_s and M_r increase after calcination at $800^\circ C$. But H_c decreases. M_s and M_r increase up to $x=0.1$ and then decreases monotonically due to (1) Fe^{3+} ions of larger magnetic moment ($5.9\mu_B$) are placed by Sm^{3+} ions of smaller magnetic moment ($1.7\mu_B$). (2) Sm^{3+} has higher molecular mass ($150.36g/mol$) than Fe^{3+} ($55g/mol$) yielding monotonically decreasing the magnetization per unit of mass over the entire x . (3) Higher surface to- volume ratio of the nanoparticles (3) presence of perovskite phase between 0.2 and 0.5 for calcined particles. Sheena Xavier, et al [16] reported that the lattice parameters a , and X-ray density D_x to increase due to the larger ionic radius of Sm^{3+} (0.964 nm) compared to that of Fe^{3+} (0.67\AA) of cobalt ferrite with the composition formula $CoFe_{2-x}Sm_xO_4$ ($x = 0.00, 0.05, 0.10, 0.15, 0.20, 0.25$). The decrease of lattice constant after $x = 0.2$ is likely due to the transfer of Co^{2+} to A site from B-site, as evident from the shifting of Bragg's peak positions to the left and no additional phase formation seen and the entire sample found to exist in *fcc*. It is also reported that the saturation magnetization value to decrease from 52.24 to 32.55 emu/g, which has been explained by the finite size effect of the nanoparticles that leading to canting or non-co linearity of spins on the surface and resulting reduction of magnetization. The saturation magnetization, M_s decreases with the Sm^{3+} content due to the decrease in the net magnetic moment with the presence of nonmagnetic materials (Sm^{3+}) in the system. S Nasrin, et al [17] reported that in $Co_{1-x}Zn_xFe_2O_4$ the grain size decreases with the Zn content but increases with the sintering temperature. The lattice constant increases with the zinc content due to smaller ionic radii of Co^{2+} replaced by larger ionic radii of Zn^{2+} . Both the X-ray and

bulk densities showed a decreasing trend with the Zn content and sintering temperature. The decrease in densities with Zn content has been reported due to the density of Zn^{2+} (7.14g/cm³), which is lower than that of Co^{2+} (8.9 g/cm³) and Fe^{3+} (7.86g/cm³). Both the M_S and H_C of $Co_{1-x}Zn_xFe_2O_4$ are reported decreasing with the concentration of Zn^{2+} . This decrease in M_S and H_C is due to the spins' canteen effect. This canteen effect arises from the strong B-B interaction. The B-B interaction increases due to an increase of Fe^{3+} ions in B-sites because some Fe^{3+} migrates from A-site to B-site when Zn^{2+} introduces for Co^{2+} ions owing to A-site preference of Zn. The Curie temperature (T_C) is reported to decrease almost linearly with the Zn content for both the sintering temperatures as shown in figure-2.7(b). This decreases in T_C due to the modification of A-B exchange interaction strength due to redistribution of cations between A-site and B-site because of Zn^{2+} substitution for the Co^{2+} ions. The variation of the real part of permeability (μ'), measured in the frequency range 1kHz – 120MHz, is shown to remain stable up to a particular frequency characterized by the onset of resonance. The dispersion of permeability is due to either domain wall movement or domain rotation or a combination of them. The values of initial permeability rise with the Zn content at a lower frequency. This frequency range is desirable for wideband video recording and wideband pulse transformer. Sonal Singhal, et al [18] reported that both the X-ray density ρ_x and lattice constant a , as calculated by Pawley and Li Bail refinement method, found to increase with Zn^{2+} ion substituted for Co^{2+} in $Co_xZn_{1-x}Fe_2O_4$ ($x=0, 0.2, 0.4, 0.6, 0.8, 1.0$) due to larger ionic radius of Zn^{2+} compared to Co^{2+} . The lattice constant a , and density ρ_x , derived from X-ray diffraction pattern also observed to increase with the Zn content while Zn^{2+} substituted for Co^{2+} at annealed temperature 1000°C. It is also reported that in simple cubic ferromagnetic spinels, the magnetic order is mainly due to the super-exchange interaction mechanism occurring between the metal ion in the A and B sublattices. The substitution of a nonmagnetic ion such as Zn, which has preferentially A site occupancy results in the reduction of the exchange interaction between A and B-sites. Hence, by varying the amount of Zn substitution, it is possible to vary the magnetic properties of the samples. According to Neel's two sublattices model of ferrimagnetism, the magnetic moment per formula unit in μ_B is expressed as $n_B^N = M_B(x) - M_A(x)$, where M_A and M_B are magnetizations of A and B sites respectively. The saturation magnetization is reported to increase for $x = 0$ to $x = 0.4$

from 84.5 emu/g to 91.6 emu/g. This is due to Zn^{2+} (0 magnetic moment) replace in A site that causing the decrease of the magnetic moment in $M_A(x)$ and thus increasing of the total magnetic moment. Again the saturation magnetization for $x > 0.4$ decreases with further concentration of Zn^{2+} , which could be due to increasing hopping length, which ultimately resulted in strengthening the B-B interactions and weakening the A-B interactions. As a consequence, the total magnetization decreases. The value of coercivity H_C reaches a maximum and decreases as the grain size increases. This variation of H_C with grain size can be explained based on domain structure, critical diameter, and anisotropy of the crystal. In the single-domain region, the coercivity H_C decreases as the grain size decreases because of thermal effects. Hence, the coercivity H_C in the single domain can be expressed as $H_C = g - \frac{h}{D^2}$ where 'g' and 'h' are constants. In the multi-domain region, the variation of coercivity can be expressed as $H_C = a + \frac{b}{D}$, where 'a' and 'b' are constants and D is the diameter of the particle. Furthermore, a decrease in coercivity observed with an increase in Zn concentration was attributed to the decrease in anisotropy that in turn decreased the domain wall energy whereas the grain size was found to increase with the annealing temperature. Hemaunt Kumar et al, [19] reported that the crystallite size, saturation magnetization, remnant magnetization, and coercivity of $CoFe_{2-x}Dy_xO_4$ to decrease with the concentration of Dy^{3+} . This decrease in the magnetization of Dy^{3+} substituted cobalt ferrite is attributed to the reduction in magnetic interaction and cation redistribution. This reduction of magnetic interaction may be correlated with the hopping lengths, which is subject to further investigation. J. A. Paulsen, et al [20] reported that in cobalt ferrite, with composition $CoMn_xFe_{2-x}O_4$, where $0 \leq x \leq 0.8$, found to cause migration of Co from B site to A site after sintering, which changes both the structural and magnetic properties. The microstructure of the un-substituted sample was found to be well defined with a large distribution of grain size. Low level ($x=0.1$ and 0.2) substitution of Mn for Fe observed to induce uniform microstructure by polygonal structure causing an increase in porosity and grain size. Further increase of substitution level ($x = 0.3, 0.4$) exhibits to decrease in density but the porosity remains almost constant. It is also reported that the cobalt ferrite has higher magnetostriction with a negative value to the parallel direction and smaller with a positive value in the perpendicular

directions. The magnetostriction shows a strong dependence on chemical composition and the nature and level of substitution. But the temperature dependence of magnetostriction is still not conclusive. However, the maximum value of magnetostriction and maximum strain derivative corresponds to $CoFe_{1.8}Mn_{0.2}O_4$. The Curie temperature T_C is reported to decrease with the increase in Mn content. The variation in magnetization, M with Mn content exhibits an Inverse relationship between them. It is also reported that there is a substantial decrease in the Curie temperature T_C but the modest decline of magnetization M with Mn content, substituted for Fe . The Curie temperature, T_C was shown to decrease approximately linearly and the magnitude of maximum magnetostriction decreases with the Mn content for Fe . But the Mn content does not adversely affect the maximum strain derivative, which makes it possible for sensor applications. The Curie temperature T_C and magnetostriction of cobalt ferrite where Mn substituted for Fe , is selectable by adjusting the Mn content, which makes it one of the best candidates to be used for magneto-mechanical sensors. Ovidiu Caltan et al [21] reported that the X-ray density D_x of $CoFe_2O_4$ (COFS), $Co_{0.8}Fe_{1.2}O_4$ (COFU), $CoFe_{1.8}Mn_{0.2}O_4$ (COFM)(Mn substituted for Fe), and $Co_{1.3}Si_{0.3}Fe_{1.4}O_4$ (COFCS) (Co and Si Substituted for Fe) synthesized by standard ceramic method, found to increase with sintering temperature due to decrease in porosity. It is also reported that the maximum magnetization under the influence of applied magnetic field 6 kOe was found to decrease with increasing sintering temperature, but the Curie temperature T_C found to be less tunable by sintering temperature and Mn content, substituted for Fe of $CoFe_{1.8}Mn_{0.2}O_4$ due to paramagnetic effect of Mn content. When Mn cation is substituted in tetrahedral or octahedral sites as Mn^{2+} for Co^{2+} , a large increase of total magnetization is expected than when the same incorporated as Mn^{3+} in the octahedral site. However, the salient observations are (i) The magnitude of magnetostriction shows a strong dependency on the chemical composition and nature and substitution level, (ii) a small amount of Mn substitution for Co in $Co_{1-2-x}Mn_xFe_{1.8-x}O_4$ enhances magnetostriction. But the further increase of Mn content decreases the same, (iii) in the case of the $CoSi_{0.2}Fe_{1.8}O_4$ sample, a small amount of Si substitution decreases magnetostriction but increases the strain derivative, and (iv) the small amount of Co and Si substitution for Fe is reported as more beneficial to the magnetic properties of cobalt ferrite. But the temperature dependency of magnetostriction is still conclusive.

O.F. Caltun, et al [22] reported that *Mn* substituted *Co* ferrite with composition formula $CoMn_xFe_{2-x}O_4$ where $x = 0, 0.2, 0.3, 0.4, \text{ and } 0.6$ were prepared by standard powder ceramic technique. By increasing the sintering temperature the Curie temperature significantly decreases, which is also accompanied by the decrease of the temperature of magneto-mechanical hysteresis. The decrease of the Curie temperature with the *Mn* substitution for *Fe* in the Cobalt ferrites also causes a decrease in the temperature of magneto-mechanical hysteresis, which is the desirable magneto-mechanical property for the sensors applications. Magnetization decreases with the substitution levels of *Mn* for *Fe*. This also causes the decrease of coercive field H_C . The sintering process does not induce any magneto-mechanical anisotropy. The magnetostriction decreases with the substitution level of *Mn* for *Fe* in the cobalt ferrite. The slope of the magnetostriction curve increases with the low substitution of *Mn* in the low field. By adjusting the *Mn* content level for *Fe* in cobalt ferrite, the Curie temperature and magnetostriction coefficient can be controlled and tunable, which makes it one of the best candidate materials to be used in magneto-mechanical sensors. Lilia Ajroudi, et al [23] reported that in the nanoparticles of cobalt ferrite with composition $Co_xFe_{3-x}O_4$, synthesized by a new nonaqueous route, derived from the work of *Pinna* concerning magnetic nanoparticles, the mean size of nanoparticles found to slight decrease with increasing *Co* amount $x = 1.8$. The relative amount of *Co* and *Fe* noticed to influence the morphology of particles. Hemaunt Kumar et al, [24] reported that the dielectric constant of dysprosium doped cobalt ferrite ($CoFe_{2-x}Dy_xO_4$) decreases with the increase in frequency, which is normal behavior. The decrease in dielectric constant with increasing frequency is because, above a certain frequency of the applied electric field, the electron exchange between Fe^{2+} to Fe^{3+} cannot follow the variation of the electric field. But for the sample sintered at 300°C , the dielectric constant remains almost unchanged with the frequency. The high value of the dielectric constant is useful in capacitor dielectrics. The low value of the dielectric constant is suitable to be used as microwave absorbers in high-frequency applications. Amrita Khan et al, [25] reported that the variation of dielectric constant (ϵ') for different compositions of $CoZn_xFe_{2-x}O_4$ to decrease continuously with increasing frequency exhibiting normal dielectric behavior of ferrites. The dielectric dispersion is rapid at the lower frequency region and remains almost independent at the higher frequency region. The incorporation of *Zn* into the

$CoZn_xFe_{2-x}O_4$ has no pronounced effect on the dielectric constant at higher frequency but significantly decreases in the lower frequency range. The observed decrease in dielectric constant is since above certain frequencies, the electronic exchange between Fe^{2+} and Fe^{3+} ions cannot follow the frequency of the applied alternating electric field. It is also reported that the resistivity increases markedly by the addition of Zn ion. The conduction mechanism in ferrite is considered as the electron hopping between Fe^{2+} and Fe^{3+} ions in the B sites. In the sample without Zn^{2+} content ($x = 0$), Fe concentration is maximum at the B sites, which is responsible for electrical conduction in ferrites. The addition of Zn in the system reduces the concentration of Fe^{2+} ions due to the presence of Zn^{2+} ions at the B sites. Hashim Farooq et al, [26] reported that the dielectric constant of $MnFe_2O_4$ as measured in the range of 600Hz to 1MHz to decrease exponentially with increasing frequency in the lower frequency range and then reached a constant value at a higher frequency range. The decrease of dielectric constant with the increasing frequency is reported due to the space charge polarization. A. A. Kadam et al [27] reported that the dielectric constant and loss $\tan \delta$ decreases with the increase of frequency and Dy content for Dysprosium doped Ni-Co substitution spinel ferrites. In its conduction, grain interior contribution is evident from the complex impedance spectroscopy. The variation of resistivity with temperature is reported to confirm its semiconducting behavior. Its low coercive field suggests that it is suitable for use in magnetic shielding devices. Swati Tapdiya et al [28] reported that Co^{2+} ions in the octahedral (B) sites Cobalt Ferrite with the composition $Co_{1-x}Mn_xFe_2O_4$ ($0.0 \leq x \leq 0.3$) nanoparticles are responsible for the origin of the anisotropy due to a strong spin-orbit interaction. The magnetic anisotropy constant for the samples decreases with Mn^{2+} substitution. The observed behavior is attributed to the fact that Mn^{2+} replaces Co^{2+} ions in the B-sites, which is responsible for a high value of the anisotropy in cobalt ferrite. This sort of magnetic property can be used for practical applications in recording media and data storage. N Ponpandian, et al [29] reported on electrical conductivity and dielectric constant for nanocrystalline $NiFe_2O_4$ spinel for four different average grain sizes, ranging from 8 to 97 nm. The activation energy for the grain and grain boundary conduction and its variation with grain size has been reported. The conduction mechanism is found to be due to the hopping of both electrons and holes. The high-temperature conductivity shows a change of slope at about 500 K for grain sizes of 8 and 12 nm and this is

attributed to the hole hopping in tetrahedral sites of NiFe_2O_4 . Since the activation energy for the dielectric relaxation is found to be almost equal to that of the dc conductivity, the mechanism of electrical conduction must be the same as that of the dielectric polarization. The real part ϵ' of the dielectric constant and the dielectric loss $\tan\delta$ for the 8 and 12 nm grain size samples are about two orders of magnitude smaller than those of the bulk NiFe_2O_4 . The anomalous frequency dependence of ϵ' has been explained based on the hopping of both electrons and holes. The electrical modulus analysis shows the non-Debye nature of the nanocrystalline nickel ferrite. Ritu Rani, et al [30] reported that the presence of Zn ions causes appreciable changes in the electrical and dielectric properties of CoFe_2O_4 . A higher value of dc resistivity, 108 Ω cm, and very low values of the dielectric loss tangent is obtained which shows that these ferrites are suitable for microwave applications. M. Atif, et al [31] reported that in Manganese substituted cobalt ferrites, *i.e.*, $\text{Co}_{1-x}\text{Mn}_x\text{Fe}_2\text{O}_4$ ($0.0 \leq x \leq 0.4$), prepared by a solid-state reaction method, *Mn* substitution changes the microstructure by migrating Fe^{3+} cations from tetrahedral (A) sites to octahedral (B) sites which have a relatively smaller covalence. To explore the effects of observed variations in the microstructure and cation distribution on the dielectric and resistive properties, the prepared samples were subjected to impedance spectroscopic experiments in a wide frequency range at room temperature. *Mn* substitution is reported to improve the resistive properties by about two orders of magnitude. This increase in the resistive properties is explained in terms of the variations in the microstructure and decrease in the mobility of the charge carriers associated with the cations redistribution. Similarly, the variation in the dielectric permittivity is also conferred in terms of the change in microstructure and cation redistribution. J.C. Maurya, et al [32] reported that the influence of manganese substitution on the magneto impedance ratio and magnetostrictive constant of cobalt ferrite. Magneto impedance was found to vary with manganese content and frequency under the action of the applied axial magnetic field. The maximum value of the magneto impedance ratio was obtained for the composition $\text{Co}_{1.1}\text{Mn}_{0.1}\text{Fe}_{1.8}\text{O}_4$ at a low frequency of 10^2 Hz. It was also noted that magnetostrictive constant under applied dc magnetic field changes with manganese content. The magnetic field required for maximum magnetostriction decreases with the substitution of cobalt by manganese in $\text{Co}_{1.2-x}\text{Mn}_x\text{Fe}_{1.8}\text{O}_4$. The value of strain sensitivity ratio $d\lambda/dH$ was maximum for $\text{Co}_{1.1}\text{Mn}_{0.1}\text{Fe}_{1.8}\text{O}_4$, whereas the value of

magnetostriction was maximum for the $\text{CoMn}_{0.2}\text{Fe}_{1.8}\text{O}_4$ sample. Zhi Hong Yang, et al [33] reported that the effect of cobalt doping on permeability spectra of nickel ferrites with excess iron ($\text{Ni}_{0.743-x}\text{Mn}_{0.057}\text{Co}_x\text{Fe}_{2.20}\text{O}_4$, $x=0-0.027$) has been studied. With increasing amounts of Co-doping, the static permeability μ_i decreases at first, then increases to the local maximum at Co substitution of $x = 0.018$, and finally decreases again. The permeability spectra go through a modification of relaxation-resonance-relaxation dispersions. The samples with Co substitution of $x = 0.018$ and 0.021 have the static permeability of ~ 13 , the resonance frequency of 400 MHz, and sufficiently low magnetic loss tangents, over 1-250 MHz, make them promising candidates for higher frequency applications. Lawrence Kumar, et al [34] reported the structural and magnetic properties of nanocrystalline $\text{Co}_{1-x}\text{Mn}_x\text{Fe}_{2-2x}\text{Mn}_{2x}\text{O}_4$ ($x = 0.1, 0.2, 0.3$ and 0.4). *Mn* is not soluble to crystal lattice beyond 0.3. Saturation magnetization, coercivity, and magnetocrystalline anisotropy constant at room temperature (25C) show a decreasing trend with an increase in Mn ion concentration in $\text{Co}_{1-x}\text{Mn}_x\text{Fe}_{2-2x}\text{Mn}_{2x}\text{O}_4$. It is due to the size effect as well as the modification of super-exchange interaction between the cations in the lattice sites. Thus, structural parameters and magnetic behaviors at room temperature in nanocrystalline $\text{Co}_{1-x}\text{Mn}_x\text{Fe}_{2-2x}\text{Mn}_{2x}\text{O}_4$ materials are controllable for $x = 0.2$. It shows some unusual behavior for high concentration ($x = 0.3$), which could be due to the strain in the lattice site. The studies on $\text{Co}_{1-x}\text{Mn}_x\text{Fe}_{2-2x}\text{Mn}_{2x}\text{O}_4$ material suggest that it can be used in high-density recording media. Sweety Supriya, et al [35] reported that the average grain size (30–40 nm) of $\text{CoFe}_{2-x}\text{Mn}_x\text{O}_4$ for $x \frac{1}{4} 0.00, 0.10, 0.15,$ and 0.2 are close to each other. Rietveld analysis of the XRD pattern reveals the crystallization of the sample to the cubic inverse spinel with the space group of $\text{Fd}3\text{m}$. The *Mn* substitution does not affect the ac impedance response of cobalt ferrite. Two transition temperatures have been reported from temperature variation ac impedance plot, as well as DC measurement. One transition temperature is below and another is above 500 K. The former one is identified as dielectric transition T_D and the later one is identified as a paramagnetic phase to ferrimagnetic phase transition temperature (T_M). The T_D increases with the increase in frequency, however, T_M is independent of frequency. These two transition temperatures are visible in the temperature variation of the DC resistivity measurement plot. Both ac impedance and dc resistivity do not vary much with the *Mn* concentration in $\text{CoFe}_{2-x}\text{Mn}_x\text{O}_4$. It is due to the similar charge

configuration of *Mn* compared to that of *Fe*. However, the minute changes are attributed to lattice strain which arises due to the different ionic size of $Mn^{2+/3+}$ and $Fe^{2+/3+}$. The frequency-dependent ac impedance measurement suggests the possible use of *Mn* substituted cobalt ferrite as a frequency band filter. The present study opens a window to understand the electrical behavior of substituted cobalt ferrite and explore it for technological applications. Ameer Azam, et al [36] reported that the increase of manganese concentration in Mn-doped SnO_2/SnO_2 there is a decrease in the crystallinity, crystallite size, and lattice constant. Complex impedance spectra demonstrate the existence of two semicircles corresponding to pure SnO_2/SnO_2 nanoparticles while one semicircle for Mn-doped samples, suggesting the dominance of grain boundary resistance in the doped samples. Moreover, the grain boundary resistance R_{gb} is found to increase, while the grain boundary capacitance C_{gb} is observed to decrease with doping. The ac conductivity shows the frequency and composition-dependent behavior. It decreases with the increase in dopant concentration and can be explained based on the grain boundary defect barrier in doped samples. The data reveals that the dielectric constant and $\tan \delta$ exhibit the normal dielectric behavior and decreases with the increase in frequency and dopant concentration, which has been explained in the light of the Maxwell–Wagner model. Dielectric loss tends to zero at a high dopant concentration in the higher frequency region implying that the material is suitable for higher frequency device applications. A. A. Birajdar, et al [37] reported that in Al^{3+} substituted Ni-Zn ferrites the unit cell parameter decreases linearly with the increase of aluminum concentration due to its small ionic radius. The structural characterization of the powders using XRD and SEM confirmed the formation of nanosized particles. The crystallite size was reduced with the increase of Al^{3+} ions. The distribution of the magnetic Fe^{3+} ions thus affected by Al^{3+} substitution has interesting effects on the magnetic structure. The system maintains ferrimagnetic ordering at room temperature for the whole range of the composition studied. The strength of the magnetic coupling, however, decreases monotonously with increasing Al^{3+} substitution. The increase in Al^{3+} content in Ni-Zn ferrite led to a considerable reduction in the saturation magnetization, whereas coercivity increased. It is also reported that the initial permeability (μ_i) decreases with the increase of Al^{3+} substitution. The real part of permeability (μ'_i) decreased

gradually with the increasing frequency. The Curie temperature decreases from 525 to 445 °C with an increase of Al³⁺ concentration. The decrease of Curie temperature with non-magnetic Al³⁺ concentration has been explained by the A-B exchange interaction strength due to the change of Fe³⁺ distribution between A and B sites. Razia Nongjai et al [38] reported that Nanoparticles of CoFe₂O₄ and CoIn_{0.15}Fe_{1.85}O₄ ferrites were prepared by the citrate gel route and characterized to understand their structural, electrical, and magnetic properties. X-ray diffraction and Raman spectroscopy were used to confirm the formation of a single-phase cubic spinel structure. The average grain sizes from the Scherrer's formula were below 50 nm. Microstructural features were obtained by scanning electron microscope and compositional analysis by energy dispersive spectroscopy. The hysteresis curve shows enhancements in coercivity while the reduction in saturation magnetization with the substitution of In³⁺ ions. Enhancement of coercivity is attributed to the transition from multi-domain to single domain nature. Electrical properties, such as dc resistivity as a function of temperature and ac conductivity as a function of frequency and temperature were studied for both the samples. The activation energy derived from the Arrhenius equation was found to increase in the doped sample. The dielectric constant (ϵ') and dielectric loss ($\tan \delta$) are also studied as a function of frequency and temperature. The variation of dielectric properties ϵ' , $\tan \delta$, and ac conductivity (σ_{ac}) with frequency reveal that the dispersion is due to Maxwell–Wagner type of interfacial polarization in general and the hopping of charge between Fe²⁺ and Fe³⁺ as well as between Co²⁺ and Co³⁺ ions at B-sites. Magnetization and electrical property study showed its dominant dependence on the grain size. Ashish Saini et al [39] reported that indium doped nanosized nickel-zinc cobalt-based ferrite ceramics with composition Ni_{0.5}Zn_{0.3}Co_{0.2}In_xFe_{2-x}O₄ (x= 0.4) material could be a very promising and potential candidate for antenna substrate of microstrip antenna in the VHF range, with miniaturized size, and very good impedance matching to the free space because of the following electromagnetic characteristics (i) electromagnetic characterization shows that the high and consistent value of permittivity and permeability of 10 and 15.2, (ii) low dielectric and magnetic loss tangent values of the order of 10⁻² and 10⁻¹, (iii) better stoichiometry and homogeneous structure, (iv) the miniaturization factor of 12.32 shows a lot of potential for the reduction of the form factor of the antenna, (v) the size of the

antenna can be reduced by 68% at a frequency of around 100MHz and lower frequencies. Sichuan Li et al [40] reported that the cobalt–ferrite nanoparticles exhibit superparamagnetism. The blocking temperatures and coercivities are dependent on the $\text{Co}^{2+}:\text{Fe}^{2+}$ ratio in the system. John Jacob et al [41] reported that single-crystalline nickel ferrite NiFe_2O_4 which has an inverse spinel structure is transformed into a mixed spinel structure when its grain size is reduced to the nanometer range. H. Arabi, et al [42] reported that the saturation magnetization of NiCoMn ferrite increases but the coercivity decreases with the calcination temperature. The increase of saturation magnetization is explained based on grain growth. The decrease of coercivity is reported to decrease due to the combination of surface effect and its anisotropy. Somalia Bawa Waje et al [43] reported that the permeability values of $\text{Co}_{0.2}\text{Ni}_{0.3}\text{Zn}_{0.5}\text{Fe}_2\text{O}_4$ vary with both the sintering temperature and frequency. Its absolute value decreased after the natural resonance frequency. The real part of permittivity is found to constant in the frequency range 10 MHz to 1 GHz while the loss tangent value decreased gradually with the increase of frequency. R. C Hansen et al [44] reported that Substrate materials of high dielectric constant can reduce the size, but suffers from two disadvantages: (i) field remains highly concentrated in high permittivity medium and (ii) decrease in the characteristic impedance of the substrate material results in impedance mismatch, hence, resulting in an antenna with low efficiency. These limitations and disadvantages can be overcome by loading antenna with magneto-dielectric materials. A Saini et al [45] reported that the miniaturization factor for microstrip antenna is a function of permittivity and permeability of substrate material, and is described by $n = \sqrt{\epsilon' + \mu'}$, which dictates to have a moderate value of permeability and permittivity for a significant reduction in antenna size. Ni-Zn ferrite is reported to be suitable for the application in a low-frequency range. Ashish Saini et al [46] reported that the materials to be used in high frequency and microwave applications require having very low electrical conductivity and dielectric loss as well as high magnetic permeability. The controlling of these electromagnetic parameters is a challenge to scientists, researchers, physicists, technologists, and engineers for size constraint applications such as in the design of antenna for portable and mobile communication systems. P. Jeppson et al [47] reported that an unanticipated superparamagnetic response has been observed in cobalt ferrite materials after thermal treatment under

an inert atmosphere. Cobalt ferrite particles were prepared via normal micelle precipitation that typically yields $\text{Co}_x\text{Fe}_{3-x}\text{O}_4$ nanoparticles ($x=0.6-1.0$). While samples thermally treated under oxygen show majority spinel phase formation, annealing in nitrogen gas yields materials consisting of Co-Fe alloy, FeS, and CoFe_2O_4 spinel. The extremely high saturation magnetization (159 emu g^{-1}) with low coercivity (31 Oe) was observed for one of the treated compositions, which drastically deviates from prototypical cobalt ferrite with large magnetocrystalline anisotropy. F.E. Carvalho et al [48] reported that niobium pentoxide (Nb_2O_5) was added to cobalt spinel ferrite (CoFe_2O_4) powders for the first time, at varying amounts of 0, 5, 10, and 15 wt%. The purpose was to evaluate the effect of niobium on the crystalline phases, microstructure and complex electromagnetic behavior (complex permittivity and permeability between 300 MHz and 10 GHz) of CoFe_2O_4 . The samples were prepared by conventional ceramic methods and sintered at 1475°C , as potential applications are as aerospace materials (radomes) which have to survive at such temperatures upon re-entry. The only crystalline phase observed in all samples was CoFe_2O_4 , but microstructural evaluation showed that a non-crystalline, niobium-rich intergranular region was formed between the grains with niobium addition, and this apparent liquid/glassy phase aided sintering as considerable grain growth was also observed. It was shown by Raman spectroscopy that this niobium-rich amorphous intergranular phase was FeNbO_4 . The electromagnetic measurements of complex permittivity (ϵ^*) and permeability (μ^*) measurements indicated a steady decrease in both permittivity and permeability with increasing niobium oxide addition, although the values for each sample were relatively stable between 300 MHz and 10 GHz. The real part of permittivity, ϵ' , decreased from ~ 12 in the pure CoFe_2O_4 to ~ 5.5 with increasing addition, while its imaginary part assumed values very close to zero. At the same time, the real permeability, μ' , decreased from ~ 1.4 to ~ 1.1 , and a similar effect can be observed in the permeability curves. The results of the complex measurements also allowed us to obtain reflectivity graphs representing the energy loss of the incident electromagnetic wave when crossing the layer of the evaluated composition. The graphs are presented in the frequency domain and indicate that the reflection loss increases with the addition of niobium. Giovanni Baldi et al [49] reported that magnetic nanoparticles have attracted increasing attention due to their potential applications in many industrial fields, even extending

their use in biomedical applications. In the latter contest, the main features of magnetic nanoparticles are the possibility to be driven by external magnetic fields, the ability to pass through capillaries without occluding them, and to absorb and convert electromagnetic radiation into heat (Magnetic Fluid Hyperthermia). The main challenges of the current works on hyperthermia deal with the achievement of higher efficiency magnetic nanoparticles, the surface grafting with ligands able to facilitate their specific internalization in tumor cells, and the design of stealth nanocomposites able to circulate in the blood compartment for a long time. This article presents the synthesis of cobalt ferrite nanoparticles dispersed in diethylene glycol via the so-called polyol strategy and the crystal size control through successive synthesis steps. Preliminary heat dissipation evaluations on the prepared samples were carried out and the question of how particle sizes affect their magnetic and hyperthermic properties was addressed as well. Furthermore, we will present how surface chemistry can be modified to change the dispersity of the product without affecting magnetic and hyperthermic properties. Fausto Fiorillo et al [50] reported that the contribution of eddy currents to power losses in polycrystalline Mn-Zn ferrites and apply it to experimental results obtained on a broad frequency range in different commercial materials and differently sized ring samples. It is varied by theory and experiment that the eddy currents can, insufficiently large specimens, measurably contribute to the energy dissipation, in conjunction with spin damping mechanisms. In this context, the direct role of the domain wall processes is shown to be negligible, with the so-called classical losses, chiefly associated with the rotations, accounting for all of the eddy-current losses. To predict the frequency-dependent classical loss in the actual heterogeneous material, the electromagnetic field equations are formulated under a variational multiscale approach, with fine and coarse scales identified with the thickness of grain boundary layers and grain size, respectively. The eddy-current patterns are correspondingly observed to evolve, on increasing the magnetizing frequency, from mostly grain-connected to circulating on the scale of the sample cross-section. Based on the measurement of the electrical resistivity versus frequency and knowledge of the average grain size, the overall frequency dependence of the classical loss is formulated. With the energy loss measured from dc to 10 MHz in different types of commercial Mn-Zn ferrites having different cross-sectional areas, it is found that the behaviors in a given material all

tend to fall onto a single curve once purged of the calculated. The residual size-independent loss is the one associated with the damping of the precessional spin motion, which can separately be accounted for. Swati Tapdiya et al [51] reported that manganese substituted cobalt Ferrite $\text{Co}_{1-x}\text{Mn}_x\text{Fe}_2\text{O}_4$ ($0 \leq x \leq 0.3$) nanoparticles were prepared using low-temperature chemical co-precipitation method. All the samples were annealed at 900°C for 3 hours. The crystal lattice symmetry and phase purity were performed by X-ray diffraction (XRD). The varying dopant concentration affects the crystalline size, surface morphology, and magnetic properties of the cobalt ferrite. The particle sizes are found to be in the range of 29-37 nm. SEM with EDAX examines the morphological and compositional analysis of the nanoparticles. EDAX confirms the presence of Co, Mn, Fe, and O. Fourier transform infrared spectroscopy (FTIR) study confirms the formation of spinel ferrite. The saturation magnetization, magnetic remanence, and coercive field of CoMn nanoparticles are obtained at room temperature. Saturation magnetization initially increases and then decreases for a higher value of dopant, which shows the applicability of these materials for recording media and magnetic data storage. Y. Melikhov et al [52] reported that the temperature variation of magnetic anisotropy and coercive field of magnetoelastic manganese-substituted cobalt ferrites $\text{CoMn}_x\text{Fe}_{2-x}\text{O}_4$ with $x=0.6$ was investigated. Major magnetic hysteresis loops were measured for each sample at temperatures over the range 10–400 K, using a superconducting quantum interference device magnetometer. The high-field regimes of the hysteresis loops were modeled using the law of approach to saturation equation, based on the assumption that at sufficiently high field only rotational processes remain, with an additional forced magnetization term that was linear with applied field. The cubic anisotropy constant K_1 was calculated from the fitting of the data to the theoretical equation. It was found that anisotropy increases substantially with decreasing temperature from 400 to 150 K, and decreases with increasing Mn content. Below 150 K, it appears that even under a maximum applied field of 5 T, the anisotropy of CoFe_2O_4 and $\text{CoMn}_{0.2}\text{Fe}_{1.8}\text{O}_4$ is so high as to prevent a complete approach to saturation, thereby making the use of the law of approach questionable in these cases. T George et al [53] reported that Abstract. Cobalt ferrite nanoparticles of average size 18 nm are synthesized by the sol-gel method and investigated the magnetic properties. The saturation magnetization value calculated from vibration

sample magnetometer (VSM) studies for CoFe_2O_4 is lower than the reported value for the bulk. The magnetization curves demonstrate a trend towards the superparamagnetic behavior of the as-prepared CoFe_2O_4 nanoparticles. The microwave magnetic parameters show a decreasing trend with the increase of frequency. R C Kambale et al [54] reported that $\text{Co}_{1.2-x}\text{Mn}_x\text{Fe}_{1.8}\text{O}_4$ ($0 \leq x \leq 0.4$) compositions were synthesized by the auto combustion route by keeping the oxidizer to fuel ratio at 1. Thermogravimetric analysis (TGA) shows the stable phase formation takes place at a temperature above 600°C . Structural characterization of all the samples was carried out by the x-ray diffraction technique. Room temperature magnetization measurements showed that, for the substitution of Co by Mn, there is an initial increase in the saturation magnetization (M_s) for lower concentrations (i.e. $x = 0.1$ and 0.2); and then the magnetization decreases for higher concentrations (i.e. $x = 0.3$ and 0.4). Also, it is observed that the coercivity (H_c) goes on decreasing with the substitution of Mn content, except for $x = 0.3$ which shows a slight increase in coercivity as compared to $x = 0.4$. Room temperature dielectric properties, namely relative dielectric permittivity (ϵ), dielectric loss ($\tan \delta$), and ac conductivity (σ_{ac}), for all the samples were studied as a function of applied frequency in the range from 20 Hz to 1 MHz. These studies indicate that the relative dielectric permittivity goes on increasing with the increase of Mn content in Co ferrite and also all the samples show the usual dielectric dispersion which is due to the Maxwell–Wagner-type interfacial polarization. The ac conductivity measurement suggests that the conduction is due to small polaron hopping. Y.D. Kolekar et al [55] reported that the frequency ($f/420$ Hz–1 MHz) and temperature ($T/300$ – 973 K) dependent dielectric properties of hafnium (Hf) incorporated cobalt ferrite ($\text{CoF}_{2-x}\text{Hf}_x\text{O}_4$ (CFO–Hf); $x/0.00$ – 0.20). The dielectric constant (ϵ_0) of CFO–Hf is T-independent at $T \leq 450$ K, at which point increasing trend prevails. A grain bulk-boundary based two-layer model, where semiconducting-grains separated by insulating-grain boundaries, satisfactorily accounts for ϵ – T (4450 K) variation. Correspondingly, electrical responses in impedance formalism are attributed to the grain and grain-boundary effects which also account for the observed two dielectric-relaxations. The results demonstrate that the dielectric phenomena in CFO–Hf can be tailored by tuning Hf-concentration. T Ramesh et al [56] reported that the effect of Al^{3+} substitution on electromagnetic properties has been studied for nanocrystalline $\text{Mg}_{0.8}\text{Cu}_{0.2}\text{Mn}_{0.05}\text{Al}_x\text{Fe}_{1.95-x}\text{O}_4$

ferrites, wherein x varies from 0 to 0.4 in steps of 0.1. These ferrites were synthesized by using the microwave hydrothermal method and then characterized using an X-ray diffractometer (XRD), Fourier transforms infrared, and transmission electron microscopy. The synthesized powders were densified using the microwave sintering method at $950^{\circ}\text{C}/50\text{min}$. The structural and surface morphology of sintered samples were characterized using XRD and atomic force microscopy, respectively. The complex permittivity and permeability properties were measured over a frequency range of 100Hz – 1.8GHz . The temperature variation of magnetic properties was measured in the temperature range of 300 – 650K . The electrical and magnetization studies inferred that the values of d.c. resistivity increases by 27%, whereas saturation magnetization decreases linearly from 38.6 to 23.0emu g^{-1} , and Curie temperature was found to be decreased from 628 to 513K with an increase of Al^{3+} ions. The low dielectric, magnetic losses, moderate saturation magnetization, and high-temperature stability properties exhibited by Al^{3+} substituted MgCuMn ferrites make them find applications in microwave devices, such as circulators and isolators, etc. The applicability of present samples for microwave devices has been tested by the measurement of ferromagnetic resonance linewidth at Ka-band. S. Shabnam et al [57] reported that the behaviors of CuFe_2O_4 nanoparticles prepared by chemical co-precipitation has been studied. The XRD result of the as dried and samples calcined at different sintering temperatures has shown that the single-phase has been observed in the as dried condition and there is no observation of extra peak. The grain size has been obtained from Scherrer's formula and found as 4nm to 56nm for the CuFe_2O_4 nanoparticle sample with the systematic variation of sintering temperature. The nanoparticle has been characterized to understand the magnetic properties from the observation of hysteresis loops. The initial permeability varies with sintering temperature due to the variation in the kinetics of diffusion which depends on the particle size of the starting material. The Curie temperature has been measured from the result of temperature dependent initial permeability. F.E. Carvalho, et al [58] Niobium pentoxide (Nb_2O_5) was added to cobalt spinel ferrite (CoFe_2O_4) powders for the first time, at varying amounts of 0, 5, 10, and 15 wt%. The purpose was to evaluate the effect of niobium on the crystalline phases, microstructure and complex electromagnetic behavior (complex permittivity and permeability between 300 MHz and 10 GHz) of CoFe_2O_4 .

The samples were prepared by conventional ceramic methods and sintered at 1475 °C, as potential applications are as aerospace materials (radomes) which have to survive at such temperatures upon re-entry. The only crystalline phase observed in all samples was CoFe_2O_4 , but microstructural evaluation showed that a non-crystalline, niobium-rich intergranular region was formed between the grains with niobium addition, and this apparent liquid/glassy phase aided sintering as considerable grain growth was also observed. It was shown by Raman spectroscopy that this niobium-rich amorphous intergranular phase was FeNbO_4 . The electromagnetic measurements of complex permittivity (ϵ^*) and permeability (μ^*) measurements indicated a steady decrease in both permittivity and permeability with increasing niobium oxide addition, although the values for each sample were relatively stable between 300 MHz and 10 GHz. The real permittivity, ϵ' , decreased from ~ 12 in the pure CoFe_2O_4 to ~ 5.5 with increasing addition, while its imaginary part assumed values very close to zero. At the same time, the real permeability, μ' , decreased from ~ 1.4 to ~ 1.1 , and a similar effect can be observed in the permeability curves. The results of the complex measurements also allowed us to obtain reflectivity graphs representing the energy loss of the incident electromagnetic wave when crossing the layer of the evaluated composition. The graphs are presented in the frequency domain and indicate that the reflection loss increases with the addition of niobium.

Kunal Pubby et al [59] Cobalt substituted nickel spinel ferrites were synthesized in the form of $\text{Ni-Co FeO}_{1.24-x}\text{X}$ ($0 \leq x \leq 1$, $\Delta 0.15$) via Pechini's sol-gel citrate method with final sintering at 1000 °C for 6 h. The structural purity of the prepared ferrites is examined by using X-ray diffraction (XRD), Raman spectroscopy, scanning electron microscopy (SEM), and energy dispersive spectroscopy (EDS). Thermogravimetric and differential thermal analysis (TG-DTA) show that the formation of the spinel phase is completed up to 700 °C. The lattice constant, cationic distribution, and cationic site parameters are estimated from XRD data. For the first time, the lattice parameter (a) is determined using four different methods and quite similar values are obtained in those. Characteristic peaks of nickel ferrites are observed in the Raman spectrum of each ferrite composition. Grain size (80–95 nm) is observed to be higher than the crystallite size (26.2–31.8 nm) due to the agglomeration of grains. Mössbauer spectra recorded at 300 K temperature show the presence of iron in only +3 valency. Variations of isomer shift, hyperfine field, quadrupole splitting, and line

width are analyzed with the amount of doped cobalt. This paper also presents the electromagnetic and shielding properties of these Ni-Co ferrites in the X-band (8.2–12.4 GHz) frequency range using a vector network analyzer (VNA). The analysis of shielding effectiveness shows that increasing the amount of cobalt in nickel ferrites increases the shielding efficiency of the ferrites which proves the utility of this specific doping. C.R.Stein et al (60) reported that the structural properties and particle sizes of the cobalt ferrite (CoFe_2O_4) nanoparticles changes monotonically with the sintering temperature. Moreover, the magnetic moment and magnetization also increases monotonically with the synthesizing temperature and thus exhibit superparamagnetism. Yuksel Koşeoğlu et al [61] reported that all the samples of $\text{Mn}_x\text{Co}_{1-x}\text{Fe}_2\text{O}_4$ possess both the ferromagnetic and superparamagnetism behavior that is separated by the blocking temperature in the low-temperature regime. This blocking temperature decreases with the increase in Mn content in the sample. R. Jabbar et al [62] reported that the average crystallite size (D) increases from 10.79 nm to 14.18 nm with increasing the Mn^{+2} doping ratio from (0.2 to 0.6) then decrease to 9.95 nm with further increasing of Mn^{+2} to (0.8) for the samples of $\text{Mn}_x\text{Co}_{1-x}\text{Fe}_2\text{O}_4$. Their dielectric properties of samples found to be decreased by increasing the doping ratio. While the hysteresis loop obtains from VSM indicated the formation of soft magnetic material and the saturation magnetization decrease from 56 emu g^{-1} ($\text{Mn}^{+2} = 0.2$) to 38 emu g^{-1} ($\text{Mn}^{+2} = 0.8$).

2.3 Findings of the Literature Review

The findings of the literature review on various parameters of structural, magnetic, and electric properties of different relevant samples so far investigated by the researches, scientists, physicists, engineers, and technologists are presented in the matrix to highlight the spaces and scopes for further investigations:

Table-3.1: Matrix to highlight the spaces and scopes for further investigations

Structural Properties #	Magnetic properties #	Electric properties#	Electromagnetic properties #	Remarks
Lattice Constant	x Magnetization	x DC resistivity	x Complex permittivity	x
Crystallite Size	x Coercivity	x AC resistivity	* Complex permeability	x
Hopping Lengths	* Remnant Magnetization	* DC Conductivity	* Impedance	*
Bond Lengths	* Curie Temperature	x AC Conductivity	* Characteristics impedance	*
X-ray Density	x Anisotropy constant	Field dependent resistivity	x Dielectric loss	x
Porosity	x Initial Permeability	x Temperature dependent resistivity	x Magnetic loss	x
Stain	* Susceptibility	* Magnetoresistance	* Temperature dependence of complex permittivity	*
Particle Size	x ZFC and FC	x Magnetostriction	x Temperature dependence of complex permeability	*
Dopant Dependency Sintering	*	i.	Very seldom investigations performed on the effect of dopant and sintering temperature on manganese (Mn) doped cobalt ferrites nanoparticles.	
Temperature dependency	x	ii.	Temperature-dependent measurement of complex permittivity and permeability is not performed on this type of material.	

Intensive investigations have been carried out on the stoichiometric composition of manganese (Mn) doped cobalt ferrite

Milling Time	*	<ul style="list-style-type: none"> iii. Impedance and characteristic impedance are an important parameter in the microwave device application. No investigation so far is performed on this aspect of this type of material. iv. Seldom investigations were performed on electromagnetic properties of the non-stoichiometric composition of cobalt ferrite doped with Mn focusing on to the high frequency and microwave device applications
--------------	---	---

Note: x indicates studied, * indicates scopes to study and # indicates not studied for CFMZ system.

3.4. Research Spaces and Scopes

The lack of in-depth analysis and scanty information on the structural correlation and tunability of fundamental magnetic and electrical properties of cobalt ferrite nanoparticles with manganese substitution led to having scopes for further study on the following aspects as evident from the literature review for the purpose:

- i. The structural parameters (lattice constant, X-ray density, hopping lengths, bond lengths, etc.) with different substitution level of *Mn* in Cobalt ferrite substituted for *Co* and *Fe* as well both in stoichiometric and non-stoichiometric ratios, which might provide the correlation between lattice constant and magnetic moment and thus ability to tune magnetic properties.
- ii. The tunability by adjusting dopant content to an optimum value of anisotropic energy from where by the external agent like ambient or operating temperature, external magnetic field cause to flip from one state to other are not evident and conspicuous.
- iii. Size effects on the structural and magnetic properties have not been investigated so far for the *Mn* substituted cobalt ferrite nanoparticles.
- iv. The frequency response of permeability and dielectric constant for *Mn* substituted Cobalt ferrite nanoparticles demands in-depth investigations to ascertain their suitability in high frequency and microwave device applications.

- v. The magnetostriction shows a strong dependence on chemical composition and the nature and level of substitution. But the temperature dependence of magnetostriction is still not conclusive.
- vi. The variation of electromagnetic parameters with the varying compositions over the high and very higher frequency ranges needs to investigate for ascertaining the suitability for high frequency and microwave components and device applications on non-stoichiometric composition.

CHAPTER – III

EXPERIMENTAL DETAILS

3.1. Introduction

In this chapter, the synthesizing technique for the preparation of the investigated samples and their characterization has been discussed elaborately. Besides, a brief description of the apparatus used in synthesizing and experimental measurement has been explained.

3.2. Synthesize Technique

3.2.1 Steps in the preparation of sample

The samples of the present research work were prepared by the solid-state reaction route using a ball milling technique. The milling time was varied to optimize the particle size. The desired amounts of high purity Co_2O_3 , MnO_2 , and Fe_2O_3 were hand-mixed followed by grounding by a mortar and pestle for 1 hour. The mixed sample was then ball milled for 8 hours, 10 hours, and 12 hours respectively to make separate samples for comparative studies. The milled samples were then calcined in a furnace at 550°C for 1 hour to complete the solid-state reaction through the diffusion of particles by thermal decomposition. The sample powder of each composition was pelletized using a hydraulic pressure of 5000 PSI in a proper dice to obtain the required geometric shape. The samples were then be sintered at temperatures 750°C and 1050°C for 1 hour for characterization. The steps and flow chart for synthesizing the samples were:

Step-1: The amounts of raw materials with high purity (Co_2O_3 , MnO_2 , and Fe_2O_3) have been calculated and weighted (calculation is shown in annex-A). The compounds have then been mixed in mortar and ground by a pestle for 2 hours.

Step-2: The hand-mixed powder of each composition has been ball milled using a planetary ball milling machine for 8 hours, 10 hours, and 12 hours individually. The speed of the milling has been kept 230 rpm during milling.

Step-3: The ball-milled mixer has been calcined in a furnace at temperature 550°C and 900°C for 1 hour, which is an important step for making materials to be homogeneous, leading to complete the solid-state reaction through the inter-diffusion of particles by thermal decomposition [63].

Step-4: The pellet/disc and toroid shaped sample of each composition has been prepared from the calcined powder using hydraulic pressure of 5000 PSI.

Step-5: Finally all the samples in the shape of pellet/disc and toroid have been sintered at temperatures 750° and 1050° C for 1 hour to reduce pores and release stress and then cooled over a long time around 4 hours in the air. The whole process is shown in the pictorial flow chart as depicted in Fig.3.1.

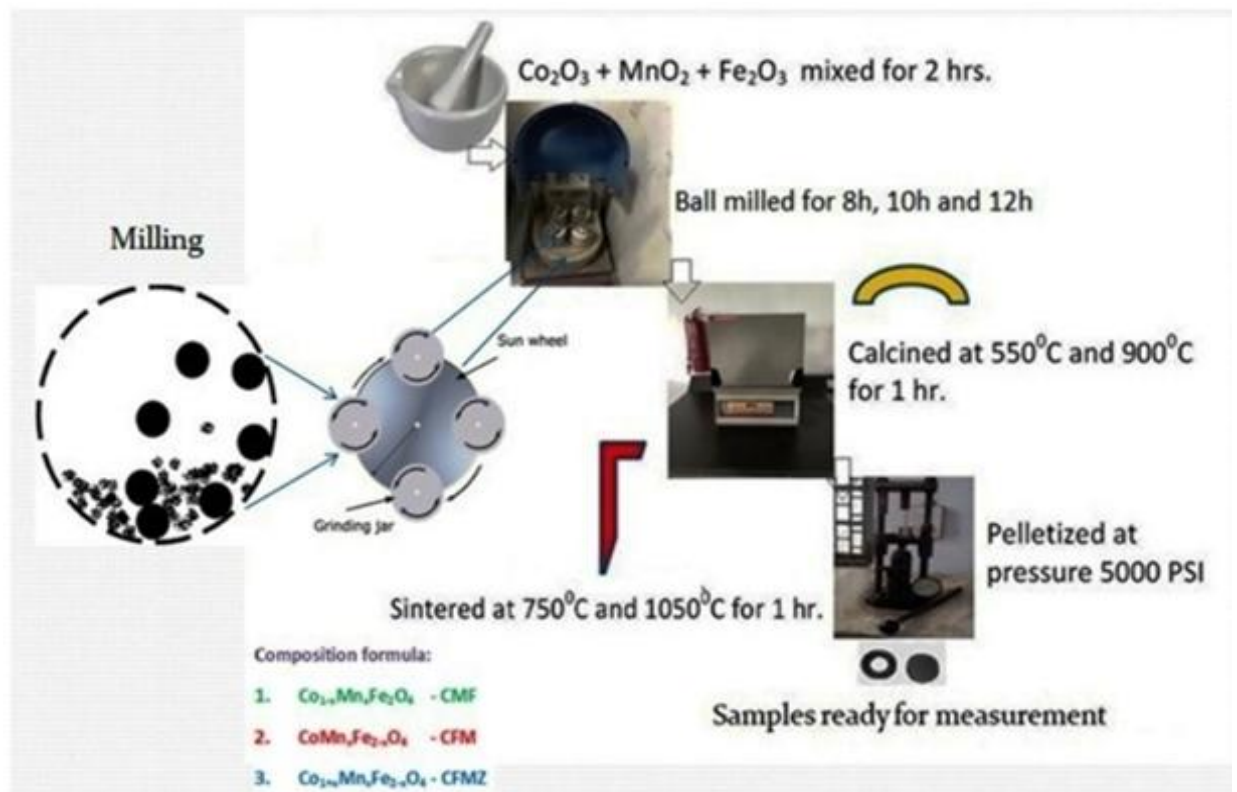


Fig.3.1: Pictorial flow chart of sample preparation method by solid-state reaction route using ball milling

3.2.2. Conventional solid-state reaction method

There are many methods of preparing spinel ferrites like the solid-state reaction method, ceramic method, chemical method, sol-gel method, combustion method, etc. Among them, the solid-state reaction method is popularly used. In the

solid-state reaction method, the general solid-state reaction leading to a ferrite may be represented as $eO + Fe_2O_3 \rightarrow MeFe_2O_4$, where Me is the divalent ions. The sample of the present research has been prepared by this solid-state reaction method using the Ball milling technique. The technique has been considered to be used based on the following principles [64]:

- i. Selecting the right powder oxide fineness which does not affect the purity. In this case, Co_2O_3 , MnO_2 , and Fe_2O_3 have been chosen.
- ii. Homogenizing the mixture during the drying process to get a very good mixture of powders that will increase the chemical reactivity.
- iii. Sintering at low temperatures to ensure chemical homogeneity according to chemical and granular characteristics of the materials.

The high fineness will be obtained using long-duration milling time and high chemical homogeneity will be achieved by low-temperature long-duration or high-temperature short-duration sintering. These will ensure the proper ionic distribution among the sites to form the good quality of the sample.

3.2.2. Hand mixing and ball milling

The laboratory graded powders of raw materials in the first step have been mixed in the mortar with pastel as shown in Fig.3.2. A ball mill a type of grinder is a cylindrical device used in grinding materials like ores, ceramic raw materials, etc. A ball mill consists of a hollow cylindrical shell rotating about its axis, partially filled with the material to be ground plus the ceramic balls as grinding medium. During the milling process, solid-state reactions are initiated through repeated deformation, cold-welding, and fracture of the raw powder particles. A planetary ball mill of the model MSK-SFM-1 benchtop as shown in Fig. 3.2 has been employed in the preparation of an investigated sample for this present research work. The schematic drawing of the planetary ball mill is also shown in Fig.3.3 [65]. 8 grinding balls (10 mm diameter and 4 g each) and an amount of 15 g starting materials, hand-mixed beforehand with appropriate proportions were used in ball milling for synthesizing nanoparticles of the investigated samples.



Fig.3.2: Ball mill and its cross-section picture(MSK-SFM-1benchtop planetary ball mill)-step-1-2

During the milling process, the sample material is primarily crushed by the high-energy impact of grinding balls together with friction between the balls and the wall of the grinding bowl. The grinding bowls with material and balls rotate around their axis on a counter-rotating supporting disc. The centrifugal forces caused by the double rotation of the grinding bowls and supporting discs work on the contents of the grinding bowls. The force, which can reach 10 times the earth's gravitational force, causes the rotating balls to crash against the inside wall of the bowl and thus crushing the material. The grinding process takes place in an argon gas or atmosphere with the adjustable rotation speed (30 - 400 rpm) and milling time. The samples of the present research work have been prepared by using this mill(MSK-SFM-1benchtop planetary ball mill). The obtained fine powder has then been calcined at temperature 550⁰C and 950⁰C for the duration of 1 h and cooled to the room temperature at the rate of 5⁰C/minute. The calcined powder was then pressed into small pellets and toroid under the pressure of 5000 PSI using hydrostatic pressing mechanize, and sealed in quartz ampoules with the atmosphere. Finally, the samples have been sintered at 750⁰, and 1050⁰C for 1 h before being furnace cooled to room temperature to characterize. Fig. 3.4 (a) shows a typical graph for the variation of particle size with the milling time. The particle size was found to decrease very rapidly from 53 nm (0h) to 21 nm (4h) during the first 4 hours from this graph. The rate of decrease in size was found to decrease with the milling time. It is found from the graph that it takes around 32 hours to decrease the particle size

from 8nm to 10 nm. So, there is a minimum possible size below of which it is very difficult to obtain nanoparticles using this ball milling technique.

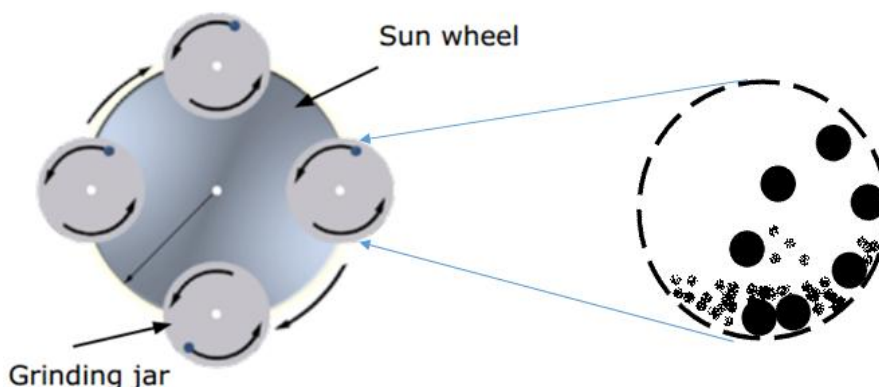


Fig.3.3: Schematic drawing of planetary ball milling machine. Adopted [95]

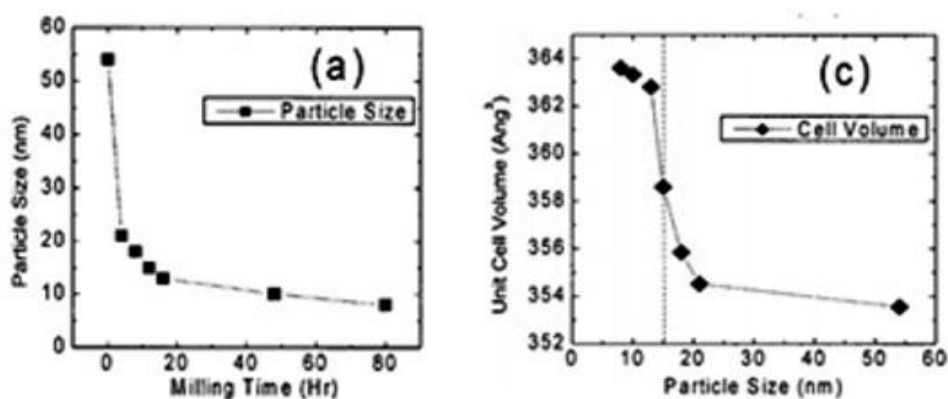
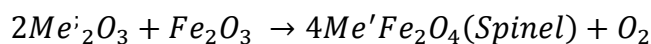
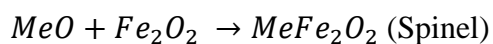


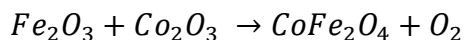
Fig. 3.4: (a) Particle size as a function of ball milling time (b) Unit cell volume as a function of particle size

3.2.3 Calcination

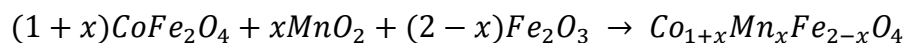
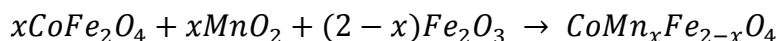
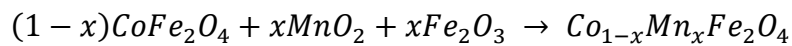
Calcination is defined as the heat treatment process of obtaining a homogeneous and phase pure composition of mixed powders by heating them for a certain time at high temperature and then allowing it to cool slowly. During the calcination stage, the reaction of Fe_2O_3 with metal oxide (say, MeO or Me'_2O_3) takes place by thermal decomposition in the solid-state to form spinel according to the reactions [66]:



The Co_2O_3 creeps into Fe_2O_3 as below to form an intermediate phase $CoFe_2O_4$ at room temperature



After those Mn ions introduced by



The purpose of calcination is to start the process of forming the spinel ferrite lattice. This process is essentially one of the inter-diffusion phenomena of substituent oxides into a chemically and crystallographically uniform structure. The driving force for the inter-diffusion is the temperature and concentration gradient. As the individual oxides inter-diffuse, some ferrite is created at the interface. This complete phase reduces further diffusion because the concentration gradient is no longer present to act as a driving force. The material in the center of each oxide particles remains as such, as they experience the difficulty in diffusing through the ferrite since the diffusion distance becomes larger. Since some shrinkage occurs in concentration, one advantage of the process is to reduce the shrinkage in the final sintering. This allows better control of the final dimension of the sintered ferrite. Besides, concentration helps in evaporation of the volatile impurities and homogenization of the powder mixer. During this process, the powder coarsens considerably, and the color changes from red to grey or black. Hence, Calcination is the process in which a material is heated to a temperature below its melting point to effect the thermal decomposition or the phase transition other than the melting point, or removal of a volatile fraction. In the present work, the ball-milled powders were calcined at 550⁰C and 900⁰C for 1 hour (step-3) in the WiseTherm furnace shown in Fig.3.5.



Fig.3.5: WiseTherm Furnace used for the calcination of the ball-milled powders in step-3

3.2.4. Pellets and rings



Fig.3.6: The pelletization in the form of pellet/disc and toroid in step-4

The calcined powders have been used to palletize the samples in the form of pellet/disc and toroid for each composition under investigation. The polyvinyl alcohol (PVA) was mixed in the powder as a binder. Finally, the powders were pressed into pellet and ring under a pressure of 5000 PSI for about 5 to 10 minutes using a uniaxial hydraulic press as shown inFig.-3.6.

3.2.5. Sintering

In the present work, the pellet/disc and toroid shaped samples as shown in Fig.3.7 were sintered in the same WiseTherm furnace as shown in Fig. 3.6 at 750°C and 1050°C for 1 hour (step-5) for electrical and magnetic measurements in the materials laboratory of the department of physics, Bangladesh University of Engineering and Technology (BUET).

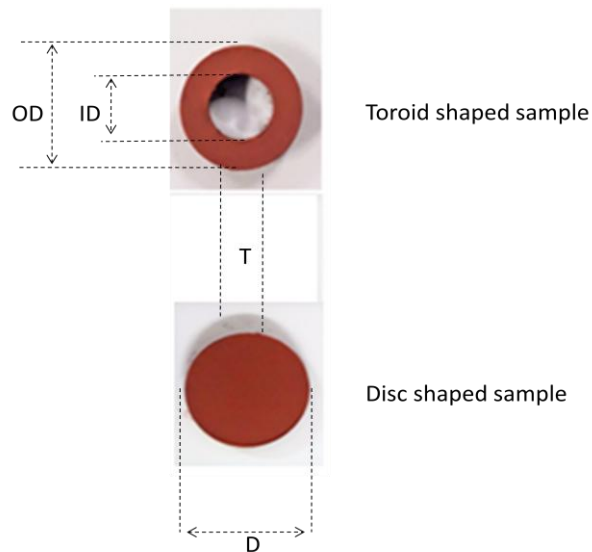


Fig.3.7: Sintering of pellet/disc and toroid shaped samples in the WiseTherm furnace in step-5

In its operation, when thermal energy is applied to a powder compact, the compact is densified and the average grain size increases. Sintering is a heat treatment process used to produce density-controlled materials and components from metal or/and ceramic powders by applying thermal energy. Hence, sintering is categorized in the synthesis/processing element among the four basic elements of materials science and engineering, as shown in Fig.3.8 [67]. As material synthesis and processing have become crucial in recent years for materials development, the importance of sintering is increasing as a material processing technology. Sintering is, in fact, one of the oldest human technologies, originating in the prehistoric era with the firing of pottery. The production of tools from sponge iron was also made possible by sintering. Nevertheless, it was only after the 1940s that sintering was studied fundamentally and scientifically. Since then, remarkable developments in sintering science have been made. One of the most important and beneficial uses of

sintering in the modern era is the fabrication of sintered parts of all kinds, including powder-metallurgical parts and bulk ceramic components. Fig.3.9 (a) [67] illustrates the general fabrication pattern of sintered parts. Unlike other processing technologies, various processing steps and variables need to be considered for the production of such parts. For example, in the shaping step, one may use simple die compaction, isotactic pressing, slip casting, injection molding, etc., according to the shape and properties required for the end product. Depending on the shaping techniques used, not only the sintering conditions but also the sintered properties may vary considerably. In the sintering step, too, there are various techniques and processing variables; variations in sintered microstructure and properties can result. Sintering aims, in general, to produce sintered parts with a producible and, if possible, designed microstructure through control of sintering variables. Microstructural control means the control of grain size, sintered density, and size and distribution of other phases including pores. In most cases, the final goal of microstructural control is to prepare a fully dense body with a fine grain structure.

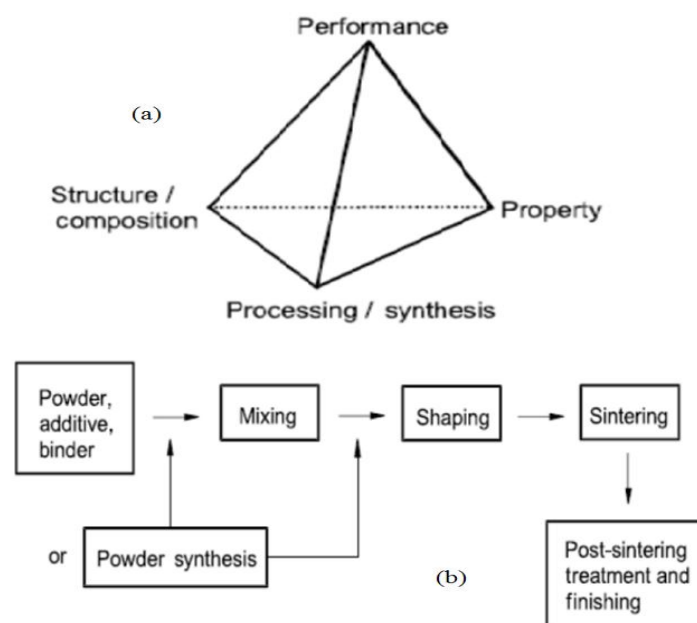


Fig.3.8: (a) The four basic elements of materials science and engineering, (b) General fabrication the pattern of sintered parts [67]

The Driving force and basic phenomena: The driving force of sintering is the reduction of the total interfacial energy. The total interfacial energy of a powder compact is expressed as γA , where γ is the specific surface (interface) energy and A

the total surface (interface) area of the compact. The reduction of the total energy can be expressed as:

$$\Delta(\gamma A) = \Delta\gamma A + \gamma\Delta A$$

Here, the change in interfacial energy (DC) is due to densification and the change in interfacial area is due to grain coarsening. For solid-state sintering, DC is related to the replacement of solid/vapor interfaces (surface) by solid/solid interfaces.

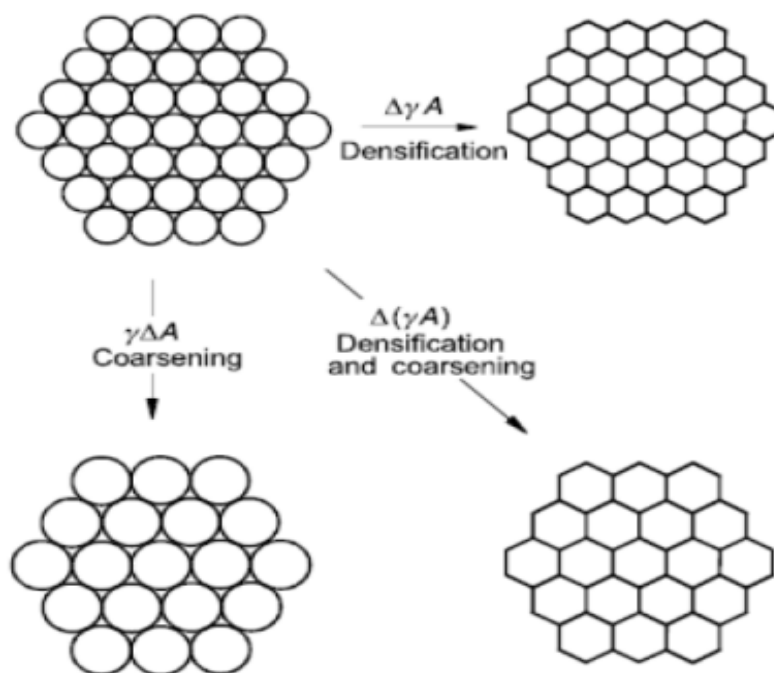


Fig-3.9: Basic phenomena occurring during sintering under the driving force for sintering, $\Delta(\gamma A)$ [67]

As chemically shown in Fig.3.9 [67], the reduction in total interfacial energy occurs via densification and grain growth, the basic phenomena of sintering. In general, the size of powders for sintering is in the range between 0.1 and 100 μm ; the total surface energy of the powder is 500–0.5 J/mole. This energy is in considerably small, compared with the energy change in oxide formation which is usually in the range between 300 and 1500 kJ/mole. If the desired microstructure of the sintered body concentration to be achieved by the use of such a very small amount of energy, it is necessary to understand and control the variables involved in the sintering processes.

3.3. Characterization Technique

3.3.1 Sample characterization

The samples of the present work were characterized in respect of structural, magnetic, electrical, and magneto-mechanical properties as appended below:

3.3.1.1 Structural properties:

- i. The crystal structure was analyzed by an EMPYREAN PANanalytical X-ray diffractometer (XRD) in the Department of Glass and Ceramic Engineering, BUET. The X-ray data were used for the determination of lattice parameters, crystallite size, and also for phase identification of the investigated samples by using X'pertpro High ScorePlus software/JPIDC card and usual formulas.
- ii. Morphological and microstructural analysis was performed in a JEOL, JSM-7600F, Field Emission Scanning Electron Microscope (FESEM) in the Department of Glass and Ceramics Engineering, BUET. The FESEM images were used for the morphological analysis and the determination of particle size by using Image-J software.
- iii. Analysis of elemental composition was done by using the Energy Dispersion Spectroscopy (EDS), which was integrated with the JEOL-FESEM instrument from the Department of Glass and Ceramics Engineering, BUET to confirm the presence of all the constituents in the samples and checking the presence of any impurities.

3.3.1.2 Magnetic and electrical properties:

- i. The dc magnetization of the prepared samples was measured in a Vibrating Sample Magnetometer (VSM) at the Department of Physics, BUET. The saturation magnetization, magnetic coercivity, and remnant magnetization were determined from the hysteresis (M-H) curves. The secondary magnetic properties e.g., the bulk magnetic anisotropy and the magnetoresistance of the samples were determined

and a correlation of these parameters with the structural and electrical properties was analyzed. Curie temperature and temperature derivative of magnetization with the variation of Mn content were determined to explore their suitability in the detection of varying electromagnetic fields.

- ii. Frequency and temperature-dependent complex permeability and permittivity of the prepared samples were measured in a Waynekerr Impedance Analyzer of model 6500B coupled with a C1000 Eurotherm PID controlled Oven. The measured parameters were used to explore the applicability of the material in the filter and antenna design over a wide range of temperatures.
- iii. Temperature-dependent capacitance, impedance, and ac resistance measurements of the prepared samples were performed with the same Impedance Analyzer. These measurements were performed at different selective frequencies to determine the optimum condition for its use in the fabrication of multilayer capacitors and bio-electronic sensor devices.
- iv. Both the temperature and magnetic field dependent dc resistivity of the prepared samples were measured by using the standard 4-probe technique. The measured parameters are used to confirm the desired magnetic semiconducting nature of the material. The magnetic field dependent resistivity is used to calculate the magnetoresistance and hence investigate its potential use in the magneto-mechanical sensor devices, which operate on the principle of thermo-magnetic properties of the material.

3.3.2 X-ray diffraction (XRD) for structural properties

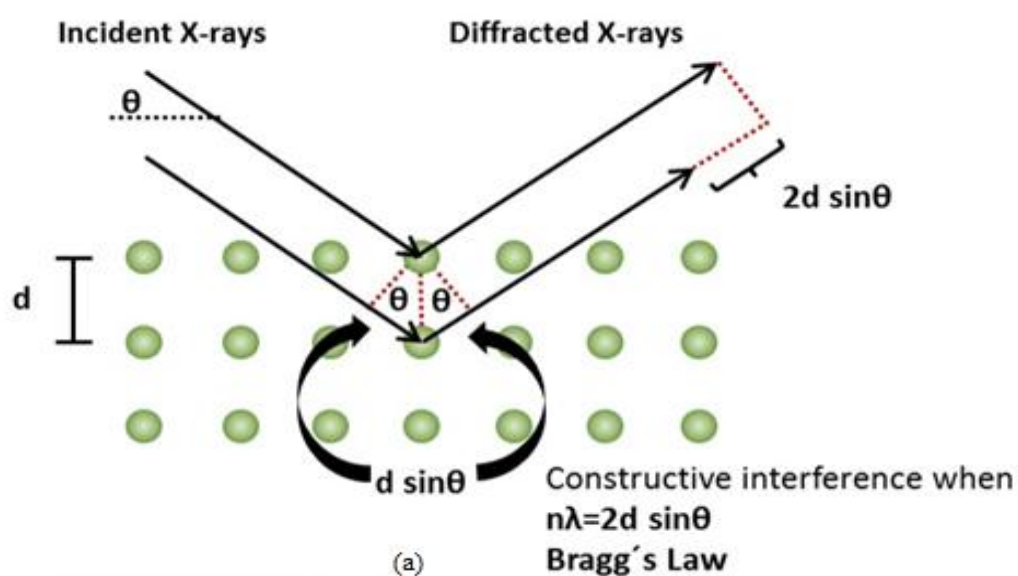
General: The X-ray diffraction technique is commonly used in the analytical characterization to gain crystallographic information of crystals. The main function of an XRD instrument is to determine the crystallographic structure, phase structure, atomic and molecular structure of crystalline materials. Since each material possesses

its own unique XRD spectra, hence quantitative and qualitative analysis can be carried out from this technique. A wealth of information about crystallographic parameters can be extracted. In the XRD technique, the crystalline structure of crystalline material causes a beam of incident X-rays to diffract into many specific directions. Powder XRD is extensively used for the identification of phases by measuring the intensities and diffraction angles of these diffracted beams. The XRD is a versatile, non-destructive materials analysis method that provides detailed information about the crystallographic and microstructure of all types of natural and synthetic materials. Bragg reflection is a coherent elastic scattering in which the energy of the X-ray is not changed on reflection. If a beam of monochromatic radiation of wavelength λ is incident on a periodic crystal plane at an angle θ and is diffracted at the same angle, then the Bragg's diffraction condition for X-rays is given by, $n\lambda = 2d \sin \theta$, which is one of the keystones in understanding X-ray diffraction. In this equation, n is an integer (order), λ is the characteristic wavelength of the X-rays impinging on the crystalline sample, d is the interplanar spacing between rows of atoms and θ is the angle of the X-ray beam to these planes as shown in Fig.3.10 (a). The diffracted X-rays will interfere constructively or destructively depending upon the path difference between the X-rays. When the path difference is an integral multiple of the wavelength of x-rays, constructive interference will take place and a characteristic diffraction pattern is produced. This diffraction pattern can be thought of as a chemical fingerprint, and chemical identification can be performed by comparing this diffraction pattern to a database of known patterns. In the present work, the XRD data were taken at the Department of Glass and Ceramic Engineering, BUET by using a PAN analytical Empyrean system. The major components of the X-ray diffractometer include: (a) an X-ray tube with Cu-K α source ($\lambda = 1.540598 \text{ \AA}$), (b) an X-rays detector, (c) a Goniometer with sample holder, and (d) Computer control. In an X-ray source used in the laboratory a beam of electrons is emitted from a heated tungsten filament in a vacuum tube, operated at 45kV and 40 mA, with X-ray wavelength, $\lambda=1.540598\text{\AA}$. Samples were scanned over the range between 10-80°. The XRD patterns were drawn by the Origin-6 software. The X'pertpro High Score Plus software was used to index the observed peaks, determine the full-width at half (FWHM) and interplanar distance, d . Then the lattice

parameters were estimated using the equation, $d = \frac{a}{\sqrt{h^2+k^2+l^2}}$, where a is the lattice constant and (hkl) the miller indices of the reflecting planes. The following stainly's equations [] have been used to estimate the bond lengths and hopping lenth considering thevalule of oxygen parameter (u) at 0.375 [6].

$$A - O = \left(u - \frac{1}{4}\right) a\sqrt{3} \text{ \AA} \text{ for tetrahedral} \quad B - O = \left(\frac{5}{8} - u\right) a \text{ \AA} \text{ for octahedral}$$

$$(L) = \frac{a\sqrt{3}}{4} \text{ \AA} \text{ for tetrahedral} \quad [L] = \frac{a\sqrt{2}}{4} \text{ \AA} \text{ for octahedral}$$



(b)

Fig-3.10: (a) The schematic diagram of Bragg's diffraction for X-ray
(b) EMPYREAN PANalytical X-ray diffractometer

3.3.3 Scanning electron microscopy (SEM) for structural properties

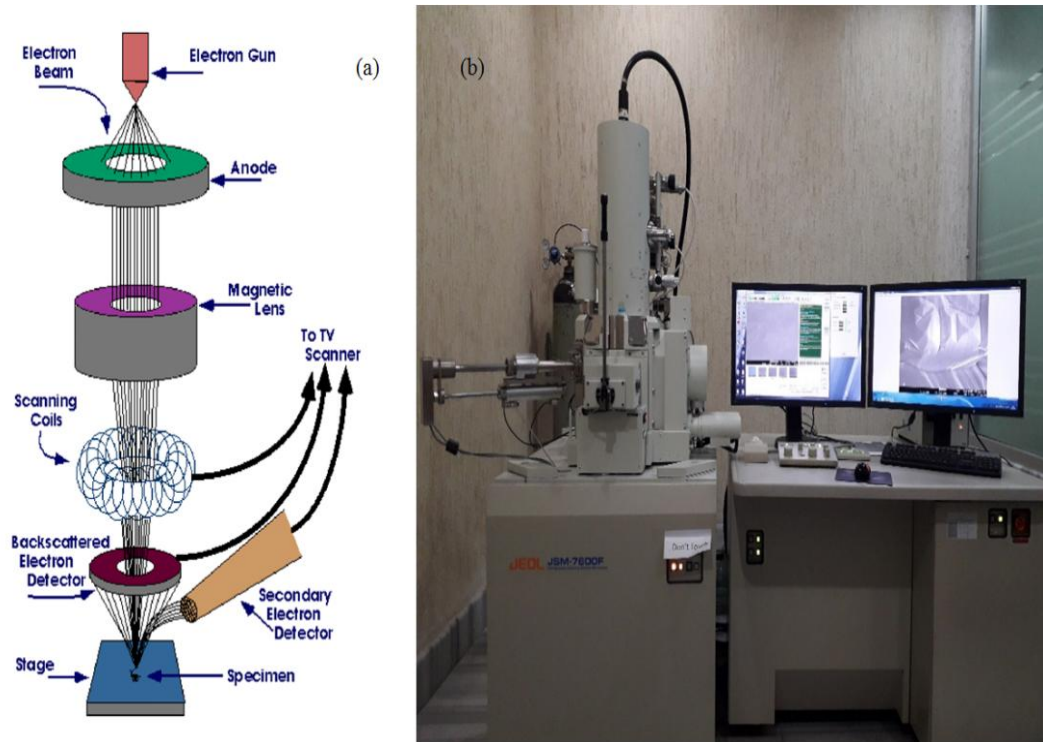


Fig.3.11: (a) The ray diagram of FESEM, (b) FESEM model JSM-7600F

The Field emission scanning electron microscopy (FESEM) is a widely used technique that provides topographical and elemental information at a magnification of 10 x to 300,000 x with virtually unlimited depth of field. The FESEM is a type of microscopy compared to other conventional scanning electron microscopy, gives more clear and magnified images scanning with high energy electrons. Electrons are liberated from a field emission source and accelerated in a high electrical field gradient. Within the high vacuum column, these so-called primary electrons are focused and deflected by electronic lenses to produce a narrow scan beam that bombards the object. As a result, secondary electrons are emitted from each spot on the object. The angle and velocity of these secondary electrons relate to the surface structure of the object. A detector catches the secondary electrons and produces an electronic signal. This signal is amplified and transformed into a video scan-image that can be seen on a monitor. In the present work, the SEM micrographs of the investigated have been taken in a FESEM of model JEOL JSM 7600F at the Department of Glass and Ceramic Engineering, BUET. Fig.3.11 shows both the ray diagram and the FESEM (JEOL model JSM-7600F) instrument.

3.3.4 Energy dispersive X-ray spectroscopy

The Energy-dispersive X-ray spectroscopy (EDX) is an analytical technique used for the elemental analysis or chemical characterization of a sample. It relies on an interaction between electromagnetic radiation and a sample. Its characterization capabilities are due to the fundamental principle that each element has a unique atomic structure allowing a unique set of peaks on its electromagnetic emission spectrum. To stimulate the emission of characteristic X-rays from a specimen, a high-energy beam of charged particles is focused into the sample being studied. At rest, an atom within the sample contains ground state (or unexcited) electrons in discrete energy levels bound to the nucleus. The incident beam may excite an electron in an inner shell, ejecting it from the shell while creating a hole. An electron from an outer, higher-energy shell then fills the hole, and the difference in energy between the higher-energy shell and the lower energy shell may be released in the form of an X-ray. The number and energy of the X-rays emitted from a specimen can be measured by an energy-dispersive spectrometer. As the energies of the X-rays are characteristic of the difference in energy between the two shells and of the atomic structure of the emitting element, EDX allows the elemental composition of the specimen to be measured. The four basic components of the EDX setup are the excitation source (electron beam or x-ray beam), the X-ray detector, the pulse processor, and the analyzer. In practice, a detector is used to convert X-ray energy into voltage signals; this information is sent to a pulse processor, which measures the signals and passes them onto an analyzer for data display and analysis. Thus, the EDX microanalysis collects the X-rays, sorts and plots them by energy, and automatically identifies and labels the elements responsible for the peaks in this energy distribution. In the present work, the compositional analysis was performed by using the EDX system attached to the FESEM (JEOL JSM 7600F).

3.3.5 Vibrating sample magnetometer (VSM) for magnetic properties

A vibrating sample magnetometer (VSM) is a scientific instrument that measures the dc magnetization of materials. The vibrating component causes a change in the magnetic field of the sample, which generates an electrical field in a coil based on Faraday's law of Induction. Faraday's law of induction states that the

induced electromotive force in a circuit is proportional to the time rate of change of magnetic flux. Mathematically, it can be written as $e.m.f = -\frac{d\phi}{dt}$ [68]. If the sample is placed within a uniform magnetic field H , a magnetization M will be induced in the sample. Magnetization is the magnetic moment per unit volume. A sample is first magnetized in a uniform magnetic field. When the magnetized sample is mechanically vibrated perpendicular to the field, a time-varying magnetic flux is created which induces an emf in the pick-up coil. The induced voltage in the pick-up coil is proportional to the sample's magnetic moment. In a typical setup as shown in Fig.3.12, the induced voltage is measured with a lock-in amplifier using the piezoelectric signal as a frequency reference. Therefore by detecting the induced voltage, the magnetic field dependent magnetization hysteresis curve of the material is measured. A known standard sample (generally Ni) is usually used to calibrate the VSM to obtain calibration constant relating the moment to the induced voltage. In the present work, the Agilent homemade vibrating sample magnetometer was used to determine the magnetization M of powder samples at room temperature and in the low-temperature regime up to 77K. This homemade VSM can provide a magnetic field in the range $-10kOe \leq H \leq +10kOe$. The sample holder used for magnetic measurement is made up of quartz. With a VSM, the magnetic moment of a sample as a function of the external magnetic field strength can be measured. Fig.3.13 illustrates (schematically) a typical result of such a measurement. The demagnetized sample ($H = 0$) is firstly magnetized to saturation in an applied field (virgin curve, see Fig. 3.13(a)).

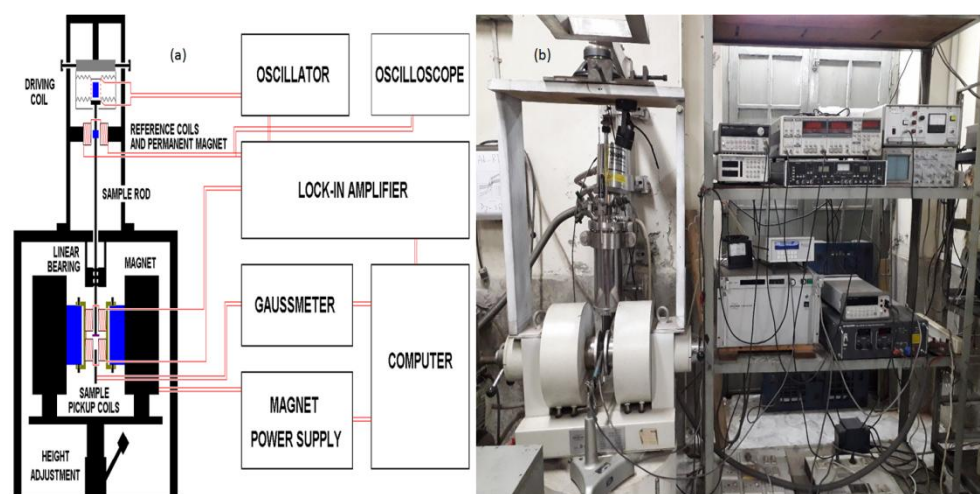


Fig.3.12: (a) The block diagram of VSM, (b) Homemade VSM

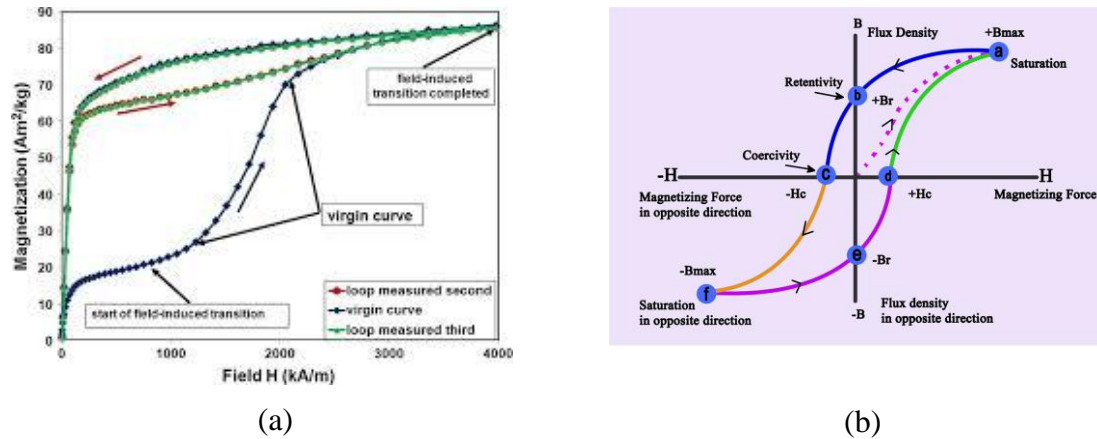


Fig.3.13: (a) Virgin curve, (b) Hysteresis loop of ferromagnetic material; [69]

As seen in Fig.3.13(a), it is indicated that there are two commonly used parameters, such as initial permeability μ_i and maximum permeability μ_{max} , defined in terms of a ratio of magnetic flux to field strength B/H . Permeability is not the slope of the virgin curve itself, but the slope of a line between the origin and a particular point on the curve (e.g. the upper inflection point before saturation for μ_{max}). Increasing and decreasing the external field from the demagnetized state to positive saturation to negative saturation and back gives a ferromagnetic hysteresis loop, which is shown in Fig. 3.13(b) [69]. Here, the predominant, underlying mechanisms for each region are indicated. The region of highest permeability is governed by domain wall motion whereas magnetization rotation occurs rather at higher magnetic fields. When the applied field is reduced to zero the remnant magnetization M_r remained. A magnetic field of opposite direction called coercivity field H_c is needed to macroscopically demagnetize the sample. Thus, the hysteresis loop contains important information about the magnetic properties of the sample. Characteristic quantities include the saturation magnetization M_s , the remnant magnetization M_r , the coercivity field H_c , permeability μ , and the dissipated energy that is necessary to magnetize the sample in the opposite direction. The dissipated energy can be calculated from the area that is included by the hysteresis loop. A pure Ni was used as a standard sample to obtain calibration constant for magnetization measurement.

3.3.6 Complex permeability measurement for frequency response

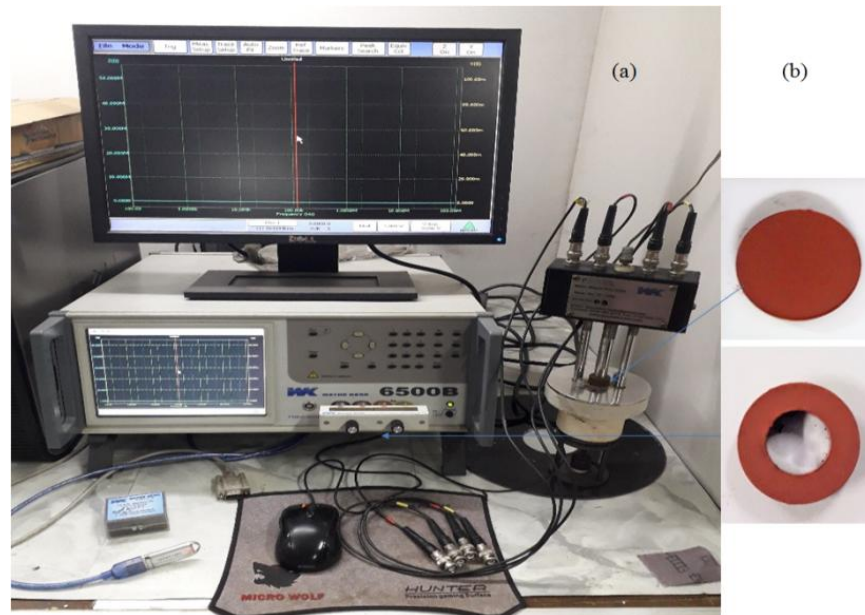


Fig.3.14:(a)The Waynekerr Impedance Analyzer 6500B (b)Toroid and disc-shaped sample for permeability measurement

The Waynekerr Impedance Analyzer 6500B series as shown in Fig.3.14 (a) was used to measure both the real part, μ' and imaginary part, μ'' directly in a series connection using the toroid shaped samples over the frequency band 100Hz – 120 MHz. In this measurement, the turn number was kept 4 turns as shown in Fig. 3.14 (b). The C1000 Eurotherm PID controlled Oven was used to measure temperature dependent permeability at different selected frequencies in the high-temperature regimes. The liquid nitrogen was used to measure the permeability in a heat shield chamber wherein the thermocouple temperature controller was used.

3.3.7 Dielectric constant measurement

To investigate the dielectric properties of the sample, the Waynekerr Impedance Analyzer 6500 B series was used using disc-shaped samples(as shown in Fig.3.14). In this investigation, complex permittivity will be directly measured using the aforesaid analyzer at room temperature in the frequency range of 100 Hz to 120 MHz. Besides, for temperature dependence, dielectric measurement, capacitance, impedance, and resistance in series connection were done by using the same impedance analyzer at selected frequencies both in the low and high-temperature

regions. The calculation of the relative dielectric constant was done by the following formula:

$$\epsilon_r = \frac{C}{C_0}$$

Here, C = the measured capacitance and

$$C_0 = \frac{\epsilon_0 A}{d}$$

Where d is the thickness of the sample and A is the area of the sample and ϵ_0 is the permittivity in free space whose value is $8.854 \times 10^{-12} \text{ Fm}^{-1}$.

3.3.8 IV measurement for magnetoresistance

The technique that was used here to measure the resistance of the sample is I - V measurement by the conventional 4-probe technique. A constant current was passed through the sample and the corresponding voltage was measured. The resistance was then calculated from the slope after fitting the trend (straight) line to the I - V curve. In this method, two of the 4 probes were used to measure the potential difference between two points, while the other terminals used to pass current through the sample as shown in Fig.3.15. For the electrical contacts, both silver glue and capacitor discharge technique can be used. Although the capacitor discharge technique is preferable for its low contact resistance, silver paste has been used in the present work to avoid the difficulty in selecting the contact discharge voltage in the capacitor discharge technique. In this case, the spacing between inner probes has been taken as effective length, l to calculate the resistivity as:

$$\rho = R \times \frac{A}{l} \Omega\text{-m}$$

Where, R is the resistance of the sample, determined from the slope of the I - V curve as shown in Fig.3.15, A is the cross-sectional area, which is the product of the width and thickness. However, to measure the resistivity as a function of the magnetic field in all the temperatures (room temperature, low and high temperatures), this 4-probe method will be used with the following experimental setup as shown in Fig. 3.16:

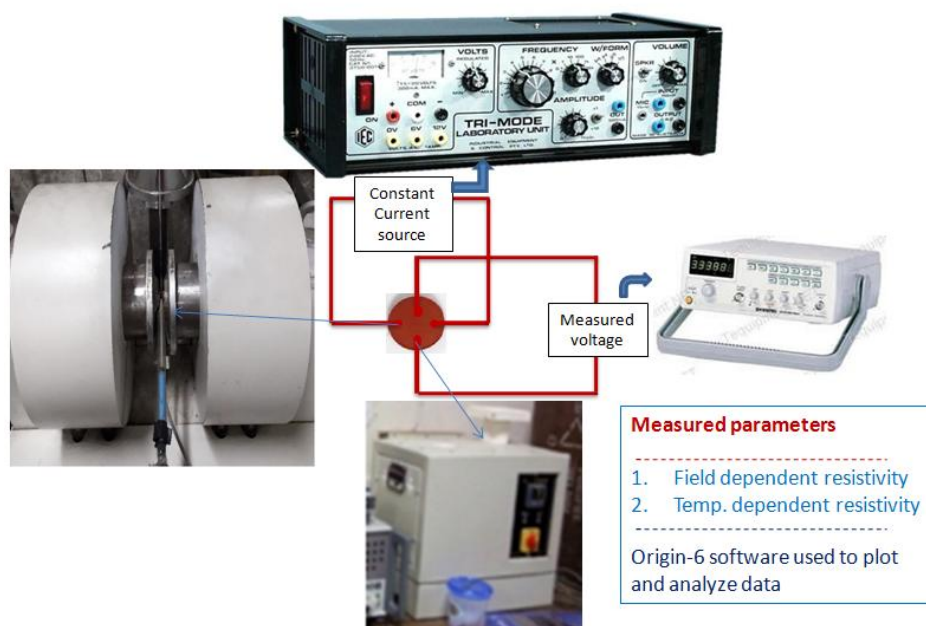


Fig.-3.15: 4-probe technique to measure resistivity; adopted [99]

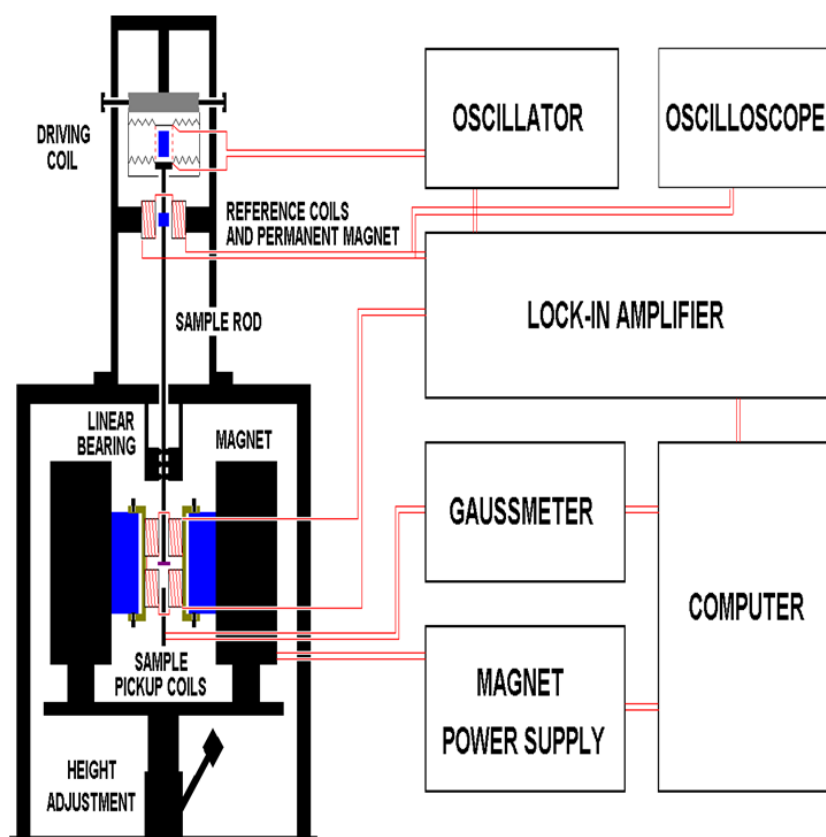


Fig.3.16: Experimental setup the measurement of field dependent resistivity[99]

3.3.8.1 Magnetoresistance determination

Magnetoresistance is determined by the calculation method from the resistivity, measured by the standard 4-probe method as discussed in section 3.3.8. By the definition of magnetoresistance, it is given by

$$MR\% = \frac{\rho_{H=x} - \rho_{H=0}}{\rho_{H=0}} \times 100$$

Where $\rho_{H=0}$ is the resistivity at the magnetic field, H=0 KG and $\rho_{H=x}$ is the resistivity at the magnetic field, H=x (x=1 ~ 4 KG with an interval of 0.5 KG)

CHAPTER – IV

RESULT AND DISCUSSION

4.1 Introduction

This chapter describes and explains the significant results of the both non-stoichiometric and stoichiometric compositions. Section-4.2 deals with the non-stoichiometric compositions, Section-4.3 and section-4 deal with the stoichiometric compositions.

4.2 Non-stoichiometric composition $Co_{1+x}Mn_xFe_{2-x}O_4$

The formula of non-stoichiometric composition is $Co_{1+x}Mn_xFe_{2-x}O_4$ where x refers to the concentration level. In this composition manganese (Mn) is substituted for iron (Fe) at x = 0.125, 0.25, 0.375, 0.5 and by the same amount in weight percent cobalt (Co) added to this composition to make this a non-stoichiometric composition.

4.2.1 Structural properties

The PANalytical X-ray diffractometer was used to record the X-ray diffraction (XRD) data as well as patterns of investigated samples for crystallographic analysis. The calcined powders of the samples were analyzed for scaling their particle size and confirm their elemental presence from the energy dispersion spectrum (EDS) by the JEOL FESEM (Field Emission Scanning Electron microscopy) instrument. In this section, the significant findings on crystallographic analysis, cation distribution, and morphological and elemental analysis have been presented in a logical sequence for analyzing structural properties in a quest of exploring their correlation with other properties.

4.2.1.1 Crystallographic analysis

Fig.4.1 shows the Rietveld refined X-ray diffraction (XRD) patterns for the samples of non-stoichiometric manganese doped cobalt ferrite nanoparticles with the composition formula $Co_{1+x}Mn_xFe_{2-x}O_4$, where $0.125 \leq x \leq 0.5$. The intense sharp peaks as observed in their XRD patterns confirm their crystallinity. They are found to well match with the standards JCPDS card No. 22-1086 for $CoFe_2O_4$ and the planes

of Mn substituted cobalt ferrite nanoparticles corresponding to Miller indices (111), (220), (311), (222), (400), (422), (511), (440) and (533) as reported in the literature [100, 102, 103]. They are also closely resembled the standard crystalline structure of CoFe_2O_4 from the International Centre for Diffraction Data (ICDD) number 221084, which belongs to the face-centered cubic spinel-type (Fd-3m) [70]. These planes exhibit the formation of a single-phase spinel structure in the investigated sample without any impurity phase. The X'pertpro High Score Plus software used for Rietveld refinement and estimation of structural parameters such as lattice constant (a) cell volume (V), X-ray density (ρ_x), the crystallite size (D_x), and strain (ϵ). The strongest peaks corresponding to the Miller plane (311) were used to estimate these parameters by the usual formulas. Besides, Stanley's equations were also used to estimate hopping lengths and bond lengths [6, 71]. In the calculation of both the hopping and bond lengths, the ideal condition of oxygen position parameter has been taken into account whose value is 0.375. All these structural parameters are listed in the following Table-4.1 as the outcome of crystallographic analysis:

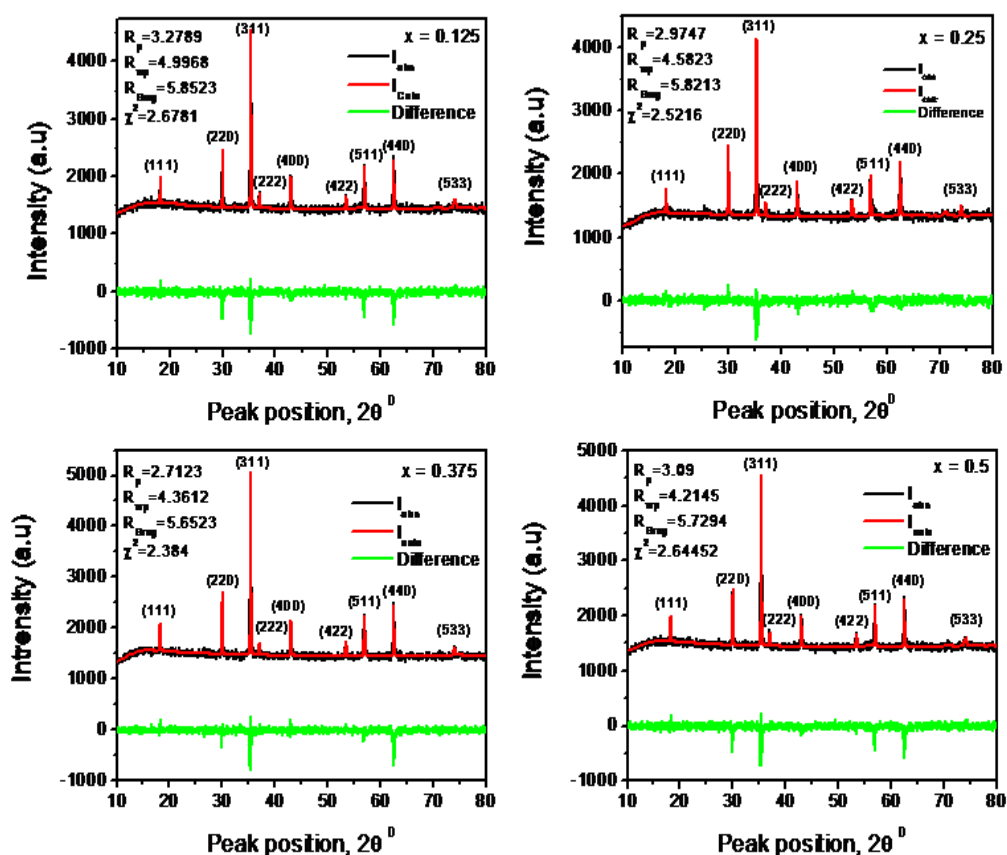


Fig.4.1: Rietveld refined X-ray diffraction (XRD) patterns of non-stoichiometric manganese doped cobalt ferrite nanoparticles at $x=0.125, 0.250, 0.375, 0.500$

Table-4.1: Different structural parameters of $\text{Co}_{1+x}\text{Mn}_x\text{Fe}_{2-x}\text{O}_4$ system at room temperature (RT)

Structural Parameters	Concentration level, x			
	x = 0.125	x = 0.25	x = 375	x = 0.5
$a(\text{Å})$	8.4100	8.4058	8.4033	8.4003
$V(\text{Å}^3)$	594.8233	593.9427	593.4132	592.7720
$\rho_x \text{ gm cm}^{-3}$	3.351	3.355	3.358	3.362
$D_x(\text{nm})$	253.22	217.72	117.14	116.13
$L_A(\text{Å})$	3.64153	3.63971	3.63863	3.63733
$L_B(\text{Å})$	2.973356	2.971871	2.970987	2.969926
$A-O(\text{Å})$	1.82085	1.81994	1.81940	1.81875
$B-O(\text{Å})$	2.10250	2.10145	2.10082	2.10007
Microstrain ϵ	0.14561	0.13036	0.11828	0.10833

From Table-4.1, a very small decrease in a , V , D_x , L_A , L_B , $A-O$, $B-O$, and ϵ are observed with the concentration levels (x) (i.e. Mn content). This trivial decreasing trend in the aforesaid parameters may arise from the relatively smaller ionic radius of Mn^{2+} (0.66Å) that replaces Fe^{3+} (0.67Å) in the B-site [72]. This monotonically linear decrease in lattice constant a is also found to follow the Vegard's law depending on the relative concentrations of Mn (54.93 g mol^{-1}) that replaces Fe ($55.84 \text{ g mole}^{-1}$) in the composition [73]. However, this small decreasing trend in the lattice constant implies the correlation between the lattice constant and ionic radius of dopant. This correlation may be expressed by an empirical equation (straight line) $a(x) = a_0 \pm mx$; where x represents the concentration level, a_0 the lattice constant at $x = 0$, m the slope that determines the rate of change in lattice constant with x , and $a(x)$ the lattice constant at any value of x [6, 73]. The lattice constant a , as determined by this equation at $x = 0$ for CoFe_2O_4 is found to be 8.4127Å , which is almost in agreement with the literature value [71, 72]. But, the X-ray density ρ_x is observed to increase with the concentration levels x and may be attributed to the decrease in volume. However, the magnitudes of D_x and ϵ are marked to differ on a large scale from corresponding previous reported values for the similar materials of composition $\text{CoMn}_x\text{Fe}_{2-x}\text{O}_4$ [72]. This enhanced size of D_x may be ascribed to the concurrent addition of Co^{2+} ions due to their non-stoichiometry and the higher calcination

temperature (900°C) that led to the growth of crystallites by fusing the particles and then changes the individual particles to the formation of granules [73, 74].

4.2.1.2 Cation distribution

In the present work, the cation distribution has been performed by X'pert pro-High Score Plus software from the Rietveld refined XRD patterns of the investigated samples as shown in Fig.4.1. From where the best information on cation distribution is achieved by comparing the experimental and calculated intensity ratios for reflections whose intensities vary with the cation distribution in opposite ways, and do not significantly differ [72, 73,75]. The final results of cation distribution are listed in the Table-4.2:

Table-4.2: Cation distribution of $\text{Co}_{1+x}\text{Mn}_x\text{Fe}_{2-x}\text{O}_4$ system as determined from Rietveld refined XRD patterns

Concentration level (x)	Cation distribution $\pm 1\%$ error	
	Tetrahedral (A) site	Octahedral (B) site
0.125	$\text{Co}_{0.016}\text{Mn}_{0.034}\text{Fe}_{0.95}$	$\text{Co}_{1.109}\text{Mn}_{0.091}\text{Fe}_{1.05}$
0.25	$\text{Co}_{0.065}\text{Mn}_{0.074}\text{Fe}_{0.88}$	$\text{Co}_{1.185}\text{Mn}_{0.174}\text{Fe}_{1.09}$
0.375	$\text{Co}_{0.053}\text{Mn}_{0.095}\text{Fe}_{0.89}$	$\text{Co}_{1.322}\text{Mn}_{0.28}\text{Fe}_{1.11}$
0.5	$\text{Co}_{0.12}\text{Mn}_{0.12}\text{Fe}_{0.87}$	$\text{Co}_{1.38}\text{Mn}_{0.38}\text{Fe}_{1.13}$

From the Table-4.2, it is seen that the Co^{2+} and Fe^{3+} ions have occupied both the A and B sites almost in equal proportionate. The Mn^{2+} ions are found to replace Fe^{3+} ions in both the sites almost at the estimated weight percent but a very small fraction of Co^{2+} ions are found to occupy A site, which may be due to their bi-valance [72]. The occupancy of Co^{2+} ions in both the sites in aggregation is observed to follow the estimated weight percent and thus the Co^{2+} and Fe^{3+} ions have been observed to redistribute in both the sites according to the non-stoichiometry of their composition. As the Co^{2+} ions occupy both sites, the cation redistribution is found to deviate from their idealistic situation [72, 73].

4.2.1.3 Morphological and elemental analysis

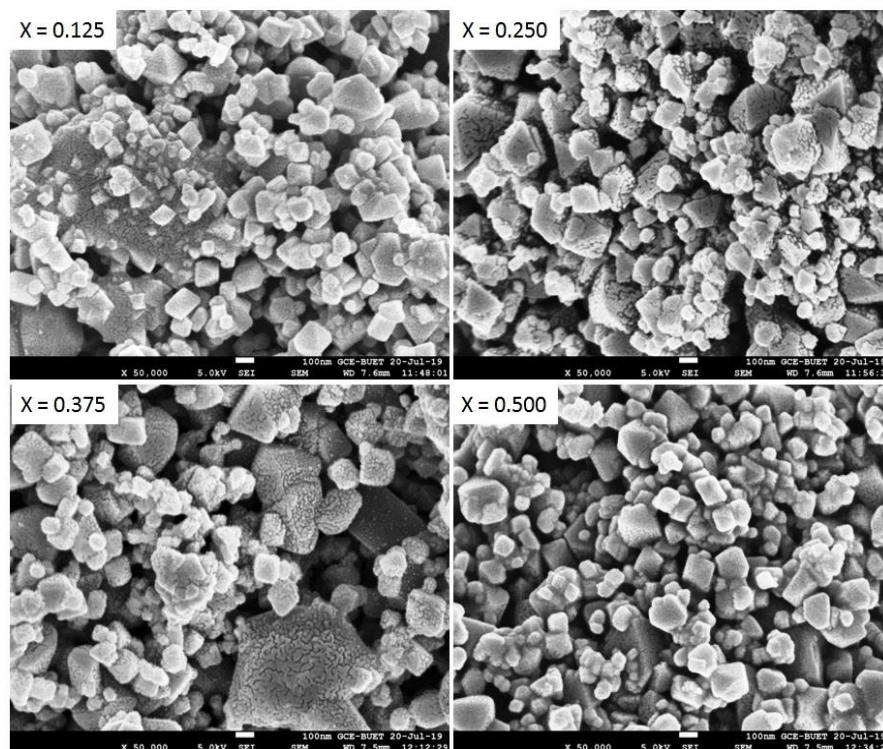


Fig.4.2: FESEM micrographs of $\text{Co}_{1+x}\text{Mn}_x\text{Fe}_{2-x}\text{O}_4$ at $x=0.125, 0.250, 0.375, 0.500$

Fig.4.2 shows the FE-SEM (FESEM, JEOL model JSM-7600F) micrographs for the investigated samples at different concentration levels, $x = 0.125, 0.25, 0.375, 0.5$. All the FESEM images in this study were taken at the same magnification of $\times 50,000$. The micrographs demonstrate randomly dispersed and several agglomerated particles with a nearly spherical shape. This agglomeration is expected to occur from the dipolar antiferromagnetic interactions between Co and Mn ions in both the sites because of the non-stoichiometry and their cation redistributions as reported in the literature [73, 76]. Besides, the formation of granules is also noticed, which may cause by the aggregation of individual particles due to the elevated calcination temperature (900°C). Fig.4.3 shows the corresponding particle size distribution histogram as enumerated by the line method using the Image-J software and found to be in the nanoscale range. The marked pores as seen in their FESEM micrographs are assumed to occur from two sources; (i) the uneven sizes and non-spherical shape of their particles due to agglomeration arising from their non-stoichiometry, and (ii) the changes of individual particles to the formation of granules due to the elevated calcination temperature [73, 77]. The presence of constituent

elements and the absence of traceable impurities are confirmed from their corresponding EDS spectrum as shown in Fig.4.4. The average particle size, particle diameter, and the elemental composition are listed in the Table-4.3 for morphological and elemental analysis. As seen from the Table-4.3, the average particle size and particle diameter are found to decrease with the concentration levels, x . This decrease in average particle size and particle diameter may arise from the effect of relatively smaller ionic size of Mn^{2+} (66 \AA) ions replacing Fe^{3+} (67 \AA) ions in both the A and B sites due to their redistribution because of comparatively higher calcination temperature (900°C) [72, 73] as evident from the Table-6.2. Moreover, their average particle size and particle diameter are observed to be larger compared to the previously reported values for the similar kind of material of the composition $CoMn_xFe_{2-x}O_4$ where Mn^{2+} ions substituted only for Fe^{3+} ions both in the A and B sites [72, 78]. This enlargement of average particle size and diameter may be assumed due to the presence of Co^{2+} (78 \AA) ions in both the sites because of their non-stoichiometry and the higher calcination temperature that evolves band-gap due to quantum confinement of their particles [73, 79].

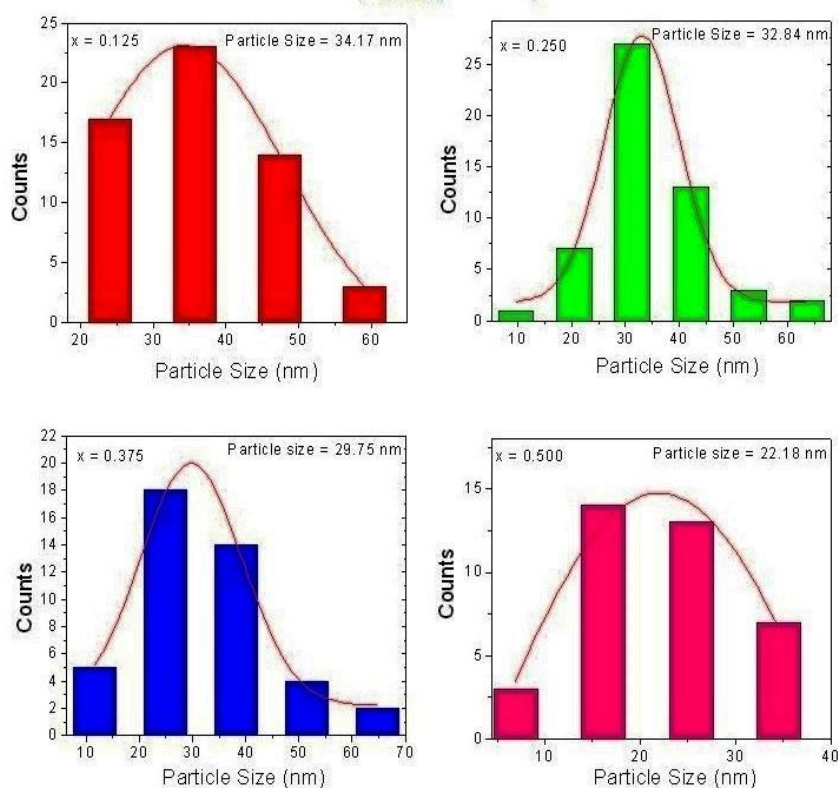


Fig.4.3: Particle size distribution histogram of $Co_{1+x}Mn_xFe_{2-x}O_4$ at $x=0.125, 0.250, 0.375, 0.500$

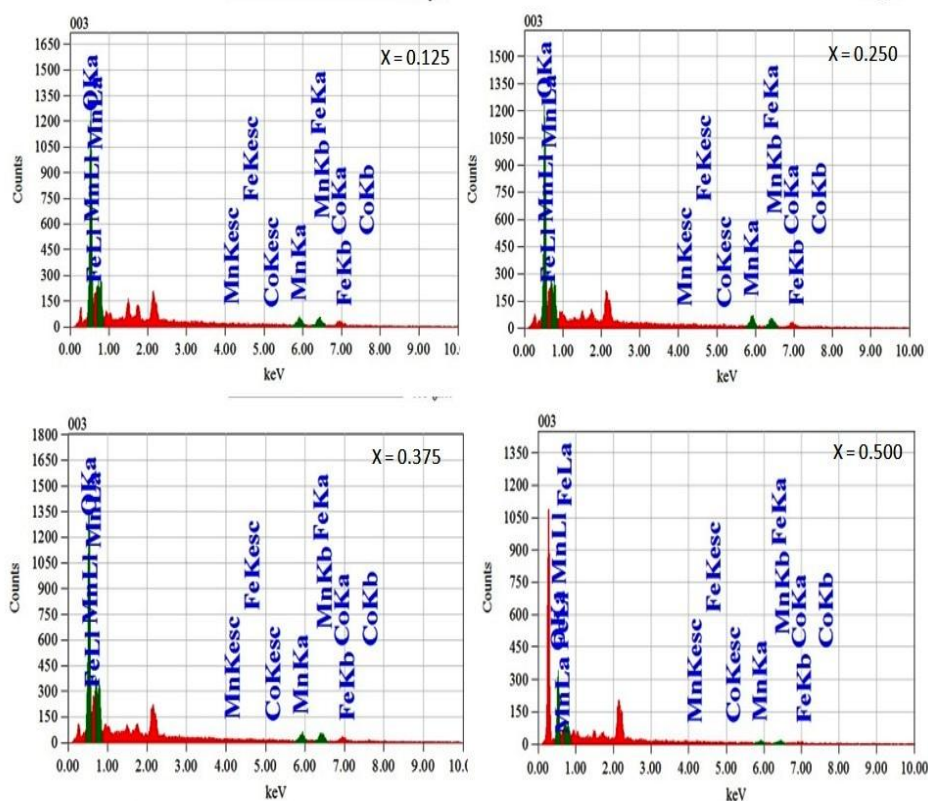


Fig.4.4: EDS spectrum of $\text{Co}_{1+x}\text{Mn}_x\text{Fe}_{2-x}\text{O}_4$ at $x=0.125, 0.250, 0.375, 0.500$

Table-4.3: Average particle sizes, particle diameter, and elemental composition of $\text{Co}_{1+x}\text{Mn}_x\text{Fe}_{2-x}\text{O}_4$ system at room temperature (RT)

Parameters	Concentration level, x			
	x = 0.125	x = 0.25	x = 375	x = 0.5
Average particle size (nm)	34.17	32.84	29.75	22.18
Diameter(nm)	43.25	40.96	39.87	28.08
Co	37.50	35.34	39.77	40.73
Mn	13.47	17.71	10.38	10.17
Fe	18.71	19.13	20.59	17.67
O	30.32	27.82	29.26	31.43
Total	100	100	100	100
Co/Fe	2.0032	1.8483	1.9315	2.3050

4.2.1.4 Effects of calcination and milling time on structural properties

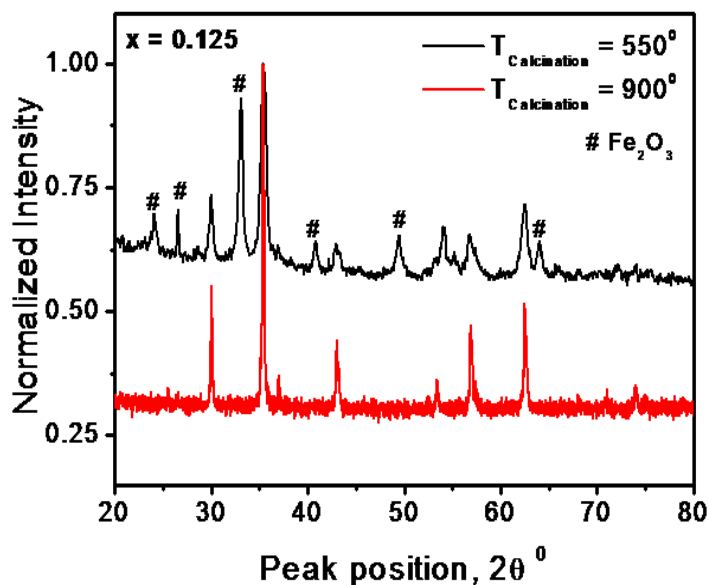


Fig.4.5: X-ray diffraction patterns for the representative samples of $\text{Co}_{1+x}\text{Mn}_x\text{Fe}_{2-x}\text{O}_4$ with concentration level, $x = 0.125$ at different calcination temperatures ($T_{\text{Calcination}}$)

Fig. 4.5 shows the X-ray diffraction patterns of a representative sample of $\text{Co}_{1-x}\text{Mn}_x\text{Fe}_2\text{O}_4$ with the concentration level, $x = 0.125$ at different calcination temperatures ($T_{\text{Calcination}}$) 550°C and 900°C to understand the effect of calcination temperature on structural properties. The peaks obtained in the XRD pattern for the sample, calcined at 550°C , exhibit the mixed secondary Fe_2O_3 phases at the peak position, $2\theta = 24, 26, 33, 41, 49, 64$ as marked with a hash (#) in the pattern [73,80]. Whereas no such secondary Fe_2O_3 phase is observed in the XRD patterns for the same sample while calcined at 900°C rather the sharp peaks are found to well match with the planes of Mn substituted cobalt ferrite nanoparticles corresponding to Miller indices (111), (220), (311), (400), (422), (511) and (440) as mentioned above [73,81]. These planes indicate that the sample exhibits a single-phase cubic spinel structure. The dissolution of such an oxide phase may have originated from the enhanced diffusion rate during their phase formation due to the elevated calcination temperature [80]. Thus it is seen that the calcination temperature has a direct effect on the diffusion rate and solid solution within the solubility limit in the solid-state reaction.

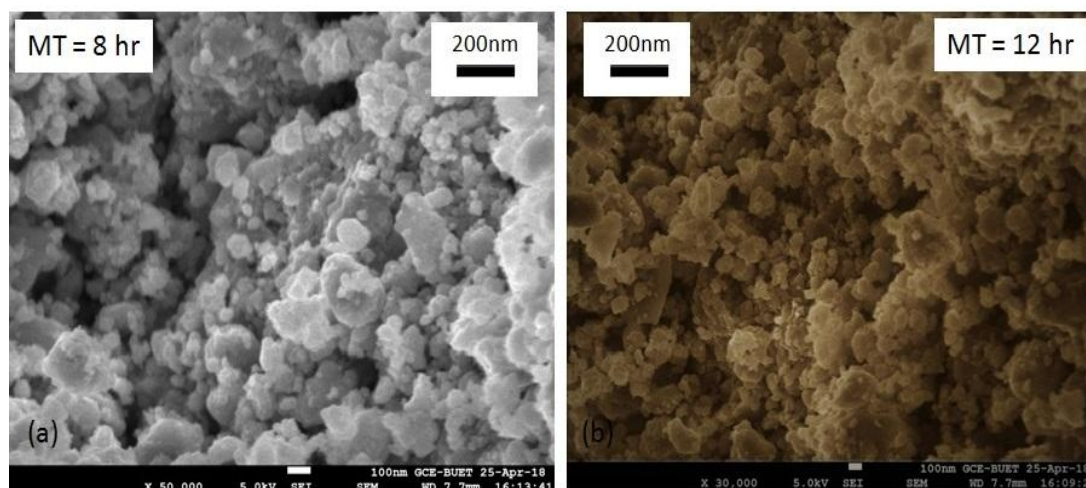


Fig.4.6: FESEM micrographs for the representative sample of $\text{Co}_{1+x}\text{Mn}_x\text{Fe}_{2-x}\text{O}_4$ with $x = 0.125$ at milling time (MT) (a) MT = 8 h (b) 12 h

Fig.4.6 shows the FESEM micrographs of the $\text{Co}_{1+x}\text{Mn}_x\text{Fe}_{2-x}\text{O}_4$ for $x = 0.125$ to demonstrate the effect of milling time. The samples were synthesized in a similar process but at different milling times (a) MT= 8h (b) MT=12h, and calcined at temperature 550°C for 1h. As seen in Fig.4.6, both the micrographs exhibit agglomerated and nearly spherical shaped particles with pores. The average particle size as enumerated from the size distribution by the line method using Image-J software is found to differ with the milling time (MT). The average particle size is found to be 19nm and 16nm for the investigated samples, ball milled for 8h and 12h respectively. This variation of particle size is as usual and assumed to be within the limit of minimum possible particle size that can be obtained from the ball milling depending on milling speed and the rate of decreasing particle size [82]. This decreasing rate again depends on the crushing and cold welding rate. So the decrease in particle size with the increase in milling time indicates that the crushing rate surpasses the cold welding. The respective EDS spectrum (not shown) confirms the presence of Co, Mn, Fe, and O without any traceable amount of impurities in the composition, and the estimated mass% of those constituents are listed in the Table-6.4 as shown below:

Table-4.4: Mass% and Estimated average particle size of the composition $\text{Co}_{1+x}\text{Mn}_x\text{Fe}_{2-x}\text{O}_4$ at $x = 0.125$

MT	Mass %				Co: Fe	Average Particle Size (nm)
	Co	Fe	O	Mn		
8 Hours	35.76	24.62	31.52	8.10	1.452	19
12 Hours	32.84	19.56	43.14	4.54	1.675	16

From Table 4.4, it is seen that the mass% of Mn content decreases with the milling time in the composition. This may have an effect of reducing the average particle size due to comparatively less amount of Fe^{3+} (67\AA) ions are substituted by the relatively smaller ionic size of Mn^{2+} (66\AA) ions in the tetrahedral (B) site of the sample of milling time 12h. Besides, the mass% of Co/Fe ratio is found to increase that may have arisen from the decreased mass% of Mn in the composition and lead to disappear off the secondary oxide phase (Fe_2O_3), produced in the sample of milling time 8h, as evident from its XRD patterns (not shown). Besides, the particle size is found to be more than twice for the same sample, calcined at temperature 900°C (34 nm) compared to that of the sample, calcined at temperature 550°C (16 nm) as evident from the Table-6.3 and Table-6.4. This increasing trend of particle size with the calcination temperature may be assumed for the band-gap evolution [72, 73, 83].

4.2.2 Magnetic Properties

To analyze the magnetic properties of the materials, the Waynekerr impedance analyzer (model 6500B) was used to measure/determine the permeability using the toroid shaped samples of $\text{Co}_{1+x}\text{Mn}_x\text{Fe}_{2-x}\text{O}_4$ at different concentration levels, $0.125 \leq x \leq 0.5$ under the variations of both frequency (1kHz – 1MHz) and temperature (323K – 573K) in the high-temperature regime, and 77K – 247K in low-temperature regime). The dc magnetization was measured using the vibrating sample magnetometer (VSM) both at room temperature (RT) and liquid nitrogen temperature (LNGT) by a thermocouple temperature controller. A comparative study is made on the permeability of the subject materials under varying conditions like sintering temperatures and milling times. However, the significant findings on the analysis of the magnetic properties of the materials are elaborately explained in this section for our purpose:

4.2.2.1 Permeability

4.2.2.1.1 Frequency response of permeability

The permeability is an important parameter governing the electromagnetic properties. This permeability is a complex quantity in the a.c. field and described by the relation, $\mu = \mu' - j\mu''$, where μ' and μ'' are the real part and imaginary parts respectively. The real part is related to the storing of magnetic energy and the imaginary part to the dissipation of magnetic energy in the form of heat[73,80,84,85]. Fig.4.7(a) shows the dispersion of μ' for the investigated samples (toroid shaped) with varying concentration level ($x = 0.125, 0.250, 0.375$ and 0.5) at room temperature (RT). The initial rise in μ' with the applied frequency up to around 2 kHz may cause from the collective effect of the domain wall motions and spin rotations.

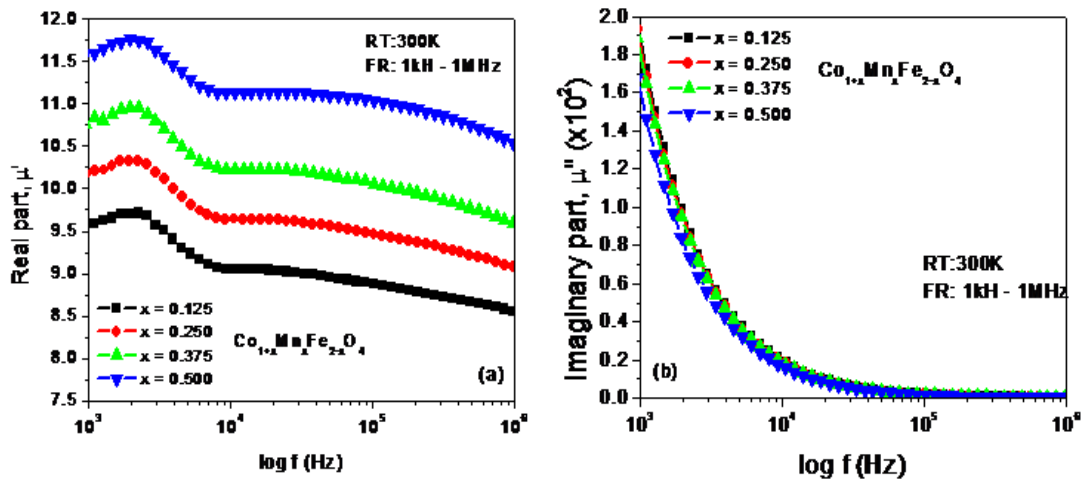


Fig.4.7: (a) Real part of complex permeability, μ' as a function of frequency for the samples of $\text{Co}_{1+x}\text{Mn}_x\text{Fe}_{2-x}\text{O}_4$, (b) Imaginary part of complex permeability, μ'' as a function of frequency for the samples of $\text{Co}_{1+x}\text{Mn}_x\text{Fe}_{2-x}\text{O}_4$

The decrease in μ' with the applied frequency over the band 2kHz – 10 kHz may originate from the lagging of dipolar orientations behind the applied frequency [73, 85]. However, a slight linear decrease in μ' with the applied frequency seems to be almost independent over the frequency band 10 kHz – 1MHz and may be attributed to the damping mechanism of spin only rotations due to nanosized particles [73, 86]. Besides, the critical frequency is found to be 2 kHz that indicates the onset of resonance. This onset of resonance resulted in a lower frequency by the natural frequency of precession. A pragmatic enhancement of μ' with the concentration

level, x at any selected frequency over the whole band is assumed to cause from the concurrent contributions of Co^{2+} and Mn^{2+} ions across the grain boundaries in the B-site due to their non-stoichiometry. Fig.4.7 (b) shows the dispersion of μ'' for the same samples. A sharp decrease in μ'' up to around 2 kHz is observed in its dispersion that may be due to the damping mechanism of dipolar orientations. This implies the domain revolution and wall movements. Afterward, μ'' becomes non-responsive to the increase of applied frequency over the band 2 kHz –1 MHz and expected to cause from the spin only rotations [73, 87].

4.2.2.1.2 Temperature response of permeability

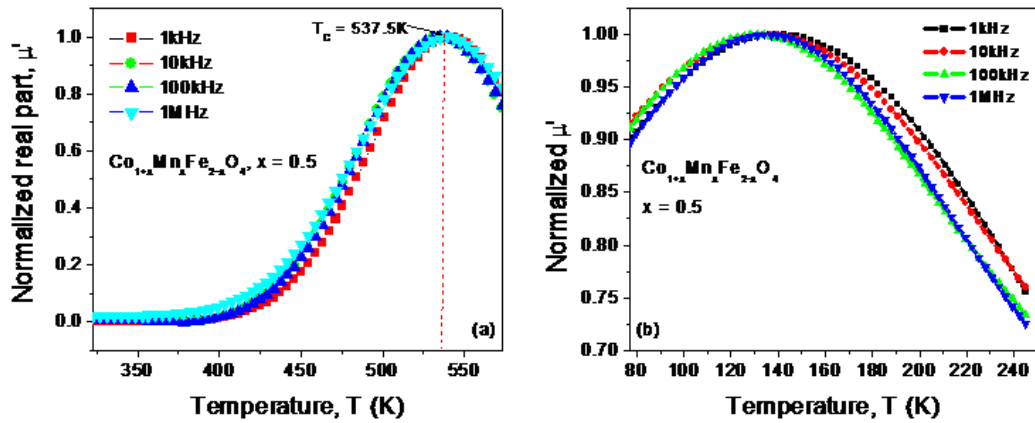


Fig.4.8: (a) Normalized real part, μ' as a function of temperature (T) above room temperature (323K–573K), (b) Normalized real part, μ'' as a function of temperature (T) below room temperature (77K–245K) for the samples of $\text{Co}_{1+x}\text{Mn}_x\text{Fe}_{2-x}\text{O}_4$ with $\text{Mn}(x) = 0.5$ at different selected frequencies

To explain the temperature dependence of ac permeability, a representative sample of concentration level ($x = 0.5$) of the $\text{Co}_{1+x}\text{Mn}_x\text{Fe}_{2-x}\text{O}_4$ system has been taken in to account. The normalized values of the real part, μ' is presented as a function of temperature both in the low-temperature regime (77K-245K) and high-temperature regime (323K – 573K) at different selected frequencies in Fig. 4.8 (a) and (b) respectively. Fig.4.8 (a) shows the temperature variation in the normalized real part, μ' of ac permeability in the temperature range 323K– 573K (above RT) for a representative sample of the concentration level, $x = 0.5$ at selected frequencies 1kHz, 10kHz, 100 kHz, 1 MHz. The value of μ' is observed for them to increase non-linearly with the increase in temperature, T (K) over the temperature range 323 – 537.5K. This increasing trend in μ' at the selected frequencies may be assumed to

cause by the dipolar orientations due to increased crystallite/grain size [6, 104]. The appearance of their relaxation peaks at around 537.5K for all selected frequencies may be related to their spin resonance [73]. However, the sudden drop in μ' from the relaxation peaks mark their ferrimagnetic-to-paramagnetic phase transition and therefore may correspond to their Curie temperature, $T_C(K)$, which is almost in agreement with the literature value for the similar kind of materials. This sudden fall in μ' from T_C may cause by the dipolar disorderliness due to their thermal agitation with the further increase in temperature and negligible anisotropy energy. As seen in Fig.6.8 (b) the normalized real part of permeability μ' is found to increase up to a certain plateau with the drop in temperature from RT and then falls. The increasing trend may arise by the dominance of magnetic energy (MH) over the thermal energy (κT) due to an increase of effective anisotropy in the low-temperature regime [73, 85]. The declining trend is expected to cause by the ceasing of dipolar orientations due to their freezing effect [73].

4.2.2.2 Magnetic modulus

4.2.2.2.1 Frequency response of magnetic modulus

In general, the permeability is associated with the domain wall relaxation (wall motion) and rotational resonance (spin rotation) [73, 88]. The driving force is responsible for causing the wall motion and rotational spin in the material. This driving force comes out from the externally applied magnetic field and thermal energy. At room temperature, the driving force remains homogeneous in all the grains in the ferromagnetic/ferromagnetic materials [89]. Under this condition, the permeability of the ferrites mostly depends on the grain size and the pores. In the ac field, the variation of domain wall relaxation and rotational resonance gives rise to the complex permeability as described by the relation, $\mu = \mu' - j\mu''$, where μ' and μ'' are the real and imaginary part of the complex permeability respectively. To understand and analyze the effect of Mn content in the complex permeability of $Co_{1-x}Mn_xFe_{2-x}O_4$, the magnetic modulus has been used to separate the local behavior of defects from any other effects (air gap, etc.). The magnetic modulus has been determined by the formula $M'_m(\omega) = \frac{\mu'(\omega)}{\mu'(\omega)^2 + \mu''(\omega)^2}$ and $M''_m(\omega) = \frac{\mu''(\omega)}{\mu'(\omega)^2 + \mu''(\omega)^2}$ from the measured values of μ' and μ'' [73]. This formalism also provides

information about inductance and magnetic resistance. Fig.6.9 shows the dispersion of the real part M'_m , it's an extended view, dispersion of imaginary part M''_m and Nyquist plots of the magnetic modules. As seen in Fig. 6.9 (a), a non-linear (almost exponential) increase in M'_m is observed with the increase of the applied frequency that signifies the contributions of both the wall motion (wall relaxation) and the spin rotations (rotational resonance) in the magnetization. Afterward, M'_m is found to a slight linear increase to a single asymptotic value, which implies the ceasing of wall motions but the only presence of spin rotations. To understand the microstructural correlation, Fig. 6.9 (b) shows an extended view of $M'_m - f$ curves at room temperature. As seen in this Fig. 6.9 (b), a cross over of the real part M'_m is noticed at a particular frequency around 58 kHz. It is interesting to note that the value of M'_m increases below this frequency (58 kHz) but decreases above it with the concentration, x i.e Mn content.

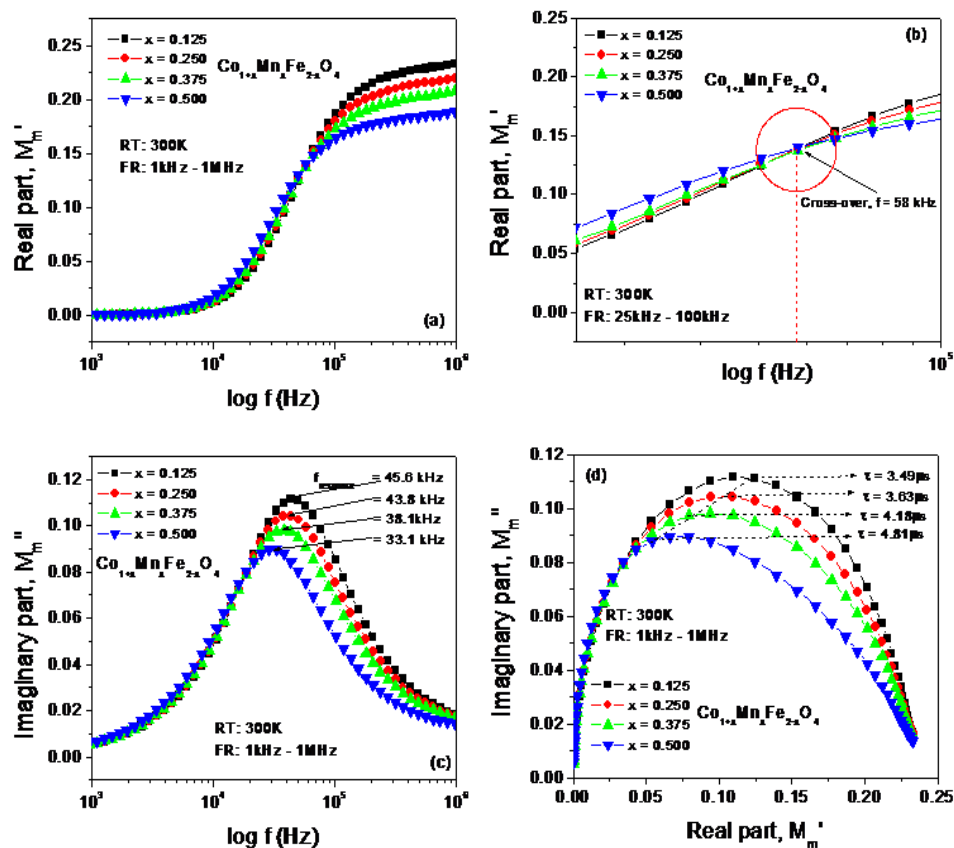


Fig.4.9: (a) M'_m vs $\log f$ curves (b) Extended view of M'_m vs $\log f$ (c) M''_m vs $\log f$ curves (d) Nyquist plot at room temperature for the samples of $\text{Co}_{1-x}\text{Mn}_x\text{Fe}_{2-x}\text{O}_4$

This increasing nature in M_m' may be attributed to the dominance of wall relaxation or dipolar orientation across the grain boundaries and the decreasing trend may be correlated to the decreasing crystallite/grain size due to non-stoichiometric composition [73]. The similar variation in the dispersion of M_m'' is observed with the increase in the applied frequency as shown in Fig.6.9 (c). However, the well-resolved peaks are observed in the $M_m''(f)$ spectra and found to shift leftward with the concentration level, x. The frequency corresponding to the peak is known as resonance frequency, $f_{resonance}$ and is observed to decrease with the concentration level, x i.e. Mn content, which also follows the decreasing trend in the crystallite/grain size [73]. Fig. 6.9 (d) shows the Nyquist plot to understand magnetic relaxation. A single semicircle of non-ideal shape is observed that exhibits the magnetic relaxation is of a single relaxation type i.e. domain wall relaxation. So an equivalent circuit is expected to be a series combination of inductance and resistance. The calculated values of relaxation time constant as enumerated from the formula $\tau_m = 1/2\pi f_{resonance}$ are listed in Table 4.5:

Table- 4.5: Resonance frequency, $f_{resonance}$ and relaxation time constant (τ) of $Co_{1+x}Mn_xFe_{2-x}O_4$

Parameters	Concentration level, x			
	x = 0.125	x = 0.25	x = 0.375	x = 0.5
Critical frequency, $f_{resonance}$	45.6 kHz	43.8 kHz	38.1 kHz	33.1 kHz
Critical relaxation time constant $\tau = 1/2\pi f_{resonance}$	3.49 μ s	3.63 μ s	4.18 μ s	4.81 μ s

From Table-4.5, it is seen that the relaxation time constant increases with the Mn content. This signifies the decrease in the damping of domain walls that results in both dipolar orientations and more spin rotations to increase the permeability of the material due to change in the metal chemistry. This implies that the porosity decreased due to the additional contribution of Co^{2+} ions, which in turn removes the pinning sites of the wall motion in the material [90].

4.2.2.2.2 Temperature response of magnetic modulus

To explain the damping mechanism below room temperature that causes the increase in the ac permeability, the imaginary part of the magnetic modulus M_m'' has

been taken into account. Fig.4.10 (a) shows the spectrum of M_m'' on a logarithmic scale. The observed well-resolved peaks correspond to the spin resonance and are found to depend on the temperature. The magnetic relaxation time for each temperature has been calculated using the formula, $\tau_{max} = 1/2\pi f_{max}$ and have been plotted their fitted values as a function of temperature as shown in Fig.4.10 (b). The relaxation time constant, τ_{max} is found to increase with the drop in temperature up to a certain peak temperature at around 131.59K, which may be termed as spin glass transition temperature, T_{trans} [73]. Afterward, τ_{max} is marked to decrease with a further drop in temperature. This increasing trend in τ_{max} implies the decrease in damping of the domain walls that increases permeability due to both the dipolar orientations and spin rotations. Conversely, the declining trend in τ_{max} signifies the ceasing of dipolar orientations due to the increased damping of wall motion that results in decreased permeability. However, in this situation, the spins may get spatially randomized in the grains due to the dominance of anisotropy energy over the thermal energy that may cause the formation of the spin-glass state [104].

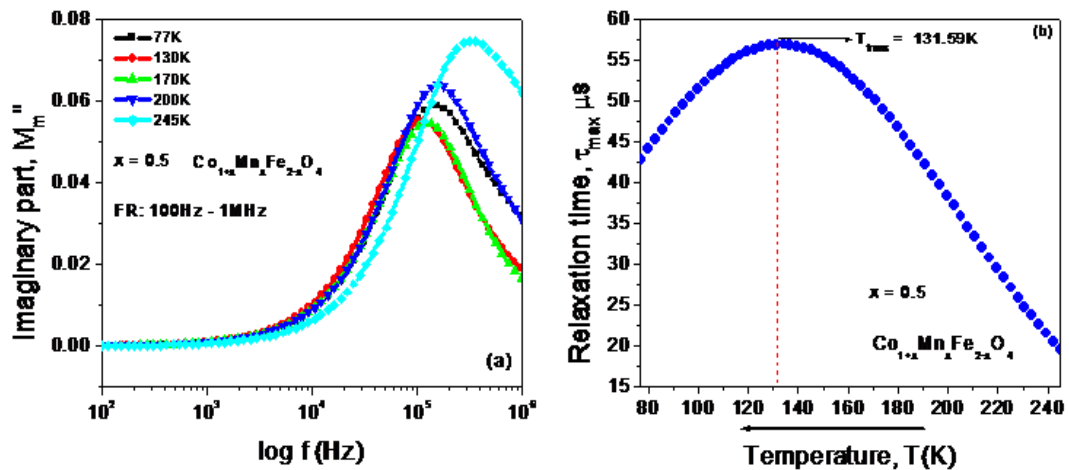


Fig.4.10: (a) Imaginary part M_m'' as a function of frequency at selected temperature, (b) Relaxation time, τ_{max} as a function of temperature (T) in the temperature range 77K – 245K for the sample of $\text{Co}_{1+x}\text{Mn}_x\text{Fe}_{2-x}\text{O}_4$ with $\text{Mn}(x) = 0.5$

4.2.2.3 Magnetization

4.2.2.3.1 Magnetization at the room temperature (RT)

Fig.4.11 (a) and (b) shows the initial magnetization (M–H) and hysteresis curves for the samples of the non-stoichiometric composition ($\text{Co}_{1+x}\text{Mn}_x\text{Fe}_{2-x}\text{O}_4$) with the concentrations levels, $x = 0.125, 0.250, 0.375$ and 0.5 at room temperature under the influence of dc magnetic field 0–4 kOe, respectively. The magnetization as found to remain constant after applying a certain amount of magnetic field is considered here as the saturation magnetization and designated as M_S . The value of M_S is determined at 4 kOe from the initial magnetization curves as shown in Fig.4.11 (a) for better comparison and analysis. The initial permeability μ_i is determined from the respective slope of the initial magnetization curve as shown by the dotted line in Fig.4.11 (a). As usual, the initial increase of magnetization with the applied magnetic field is due to the dominant effect of the domain wall motion. The saturation condition of magnetization arises from the perfect alignment of spins with the external applied magnetic field, where the domain wall motion stops. The irreversibility of the domain wall in its motion with the removal of the applied magnetic field generates the coercivity, H_C , and remnant magnetization, M_R , which are determined from the hysteresis curves as shown in Fig.4.11 (b). The values of magnetization (M_S), coercivity (H_C), remnant magnetization (M_R), and initial permeability (μ_i) are presented in the following Table-6.6 to analyze the effect of manganese (Mn) thereon.

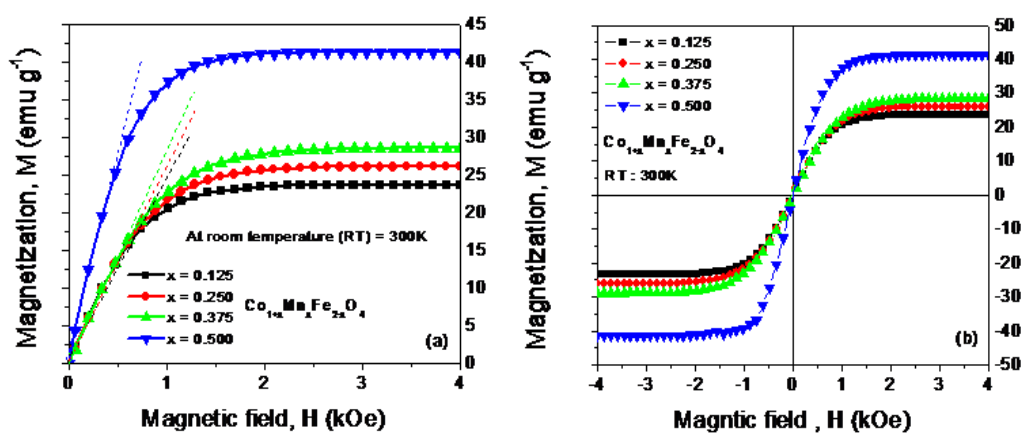


Fig.4.11: (a) Initial magnetization curves for the non-stoichiometric composition (b) Hysteresis curves for the non-stoichiometric composition at room temperature in the magnetic field range 0 – 4 kOe

Table-4.6: Values of M_S , H_C , M_R and μ_i for the investigates samples of $Co_{1+x}Mn_xFe_{2-x}O_4$ at room temperature (RT)

x	M_S (emu g ⁻¹)	H_C (Oe)	M_R (emu g ⁻¹)	μ_i	M_R/M_S
0.125	23.63	24.87	1.96	29.63	0.083
0.25	26.26	37.04	2.23	30.20	0.085
0.375	28.60	49.21	2.49	31.34	0.087
0.5	41.38	18.41	1.32	58.97	0.032

From the Table-4.6, it is seen that the saturation magnetization, M_S and initial permeability, μ_i increases with the concentration levels, x , which may have come out from the dilution effect of Mn^{2+} in the A site according to Neel's two sublattice model [91]. The value of this initial permeability μ_i is found to be maximum for the sample of $x = 0.5$ and significant as compared to the other similar materials, which is an important magnetic parameter to be taken into account in the field of high-frequency applications. However, the remnant magnetization ratio (M_R/M_S) and coercivity, H_C are found to increase up to $x = 0.375$ and then decreased at $x = 0.5$, which demonstrates the unusual magnetic behavior due to the migration of Co^{2+} ions to the A-site during cation redistribution [28] as seen in the Tabl-4.2.

4.2.2.3.2 Temperature dependent magnetization

Fig.4.12 shows the hysteresis curves (along with fitted curves) for the composition $Co_{1+x}Mn_xFe_{2-x}O_4$ at the concentration level, $x = 0.125$ (a), $x = 0.375$ (b) and $x = 0.5$ (c) in the temperature range 77 – 300 K (low-temperature regime). All the curves demonstrate the usual variation of temperature-dependent magnetization, M (T) with the increase of the magnetic field for each temperature according to Neel's two sublattice models as stated above. The temperature-dependent magnetization (M) at the magnetic field of 4 kOe is found to increase almost linearly as shown in Fig.4.13 (a) while the temperature drops down from the room temperature (RT = 300 K) to 77 K (LNG temp). This variation nature in M is consistent with the previously reported observations and expected to cause from the dominance of effective uniaxial anisotropy constant (K_{ef}) due to the additional presence of Co^{2+} ions in the B site as seen in the Table-4.2 because of the non-stoichiometric composition as explained in the literature[92].

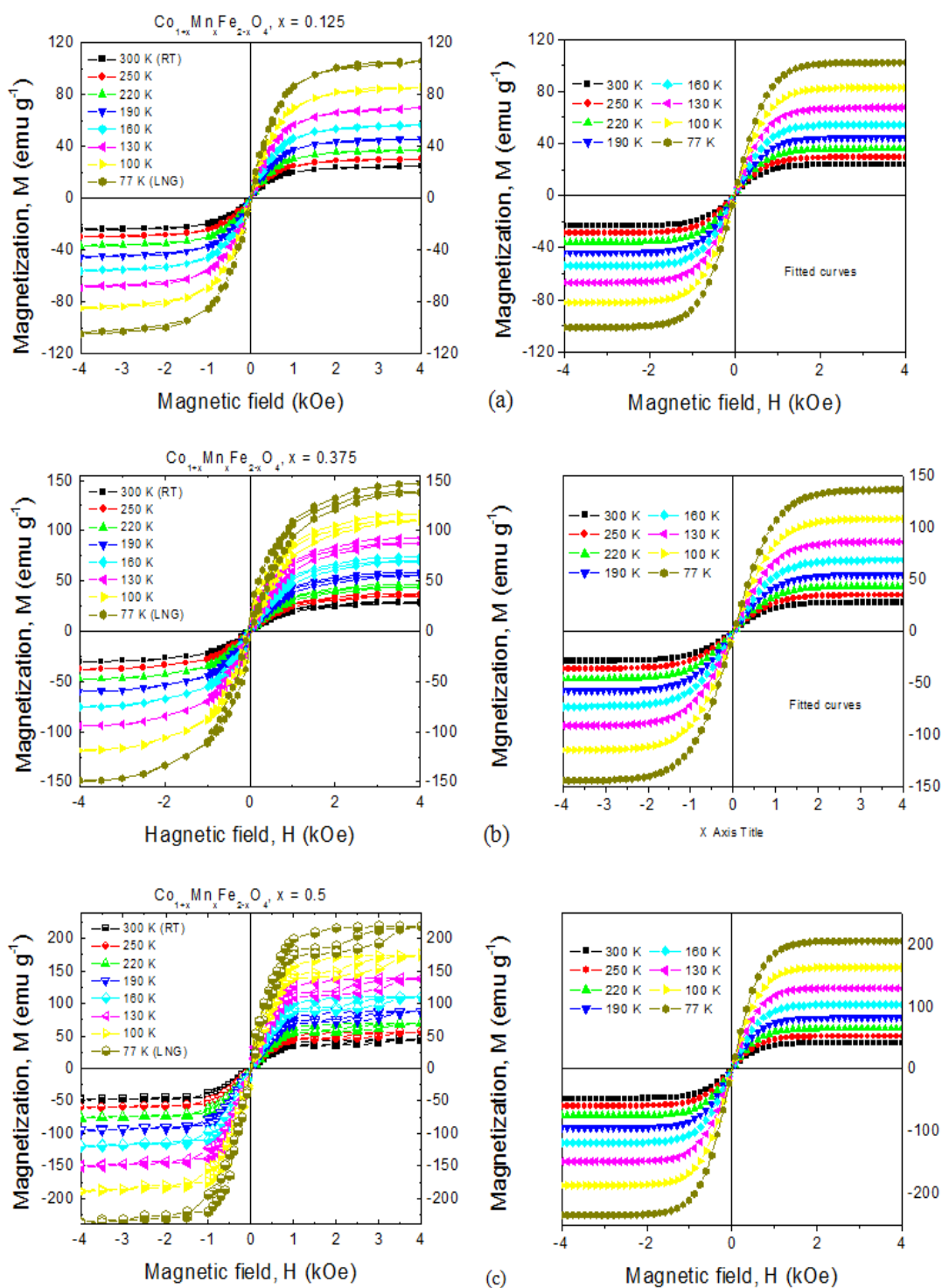


Fig.4.12: Hysteresis curves in the temperature regime 77 – 300K (left: non-fitted and right:fitted) for the samples (a) $x = 0.125$, (b) $x = .375$, (c) $x = 0,5$

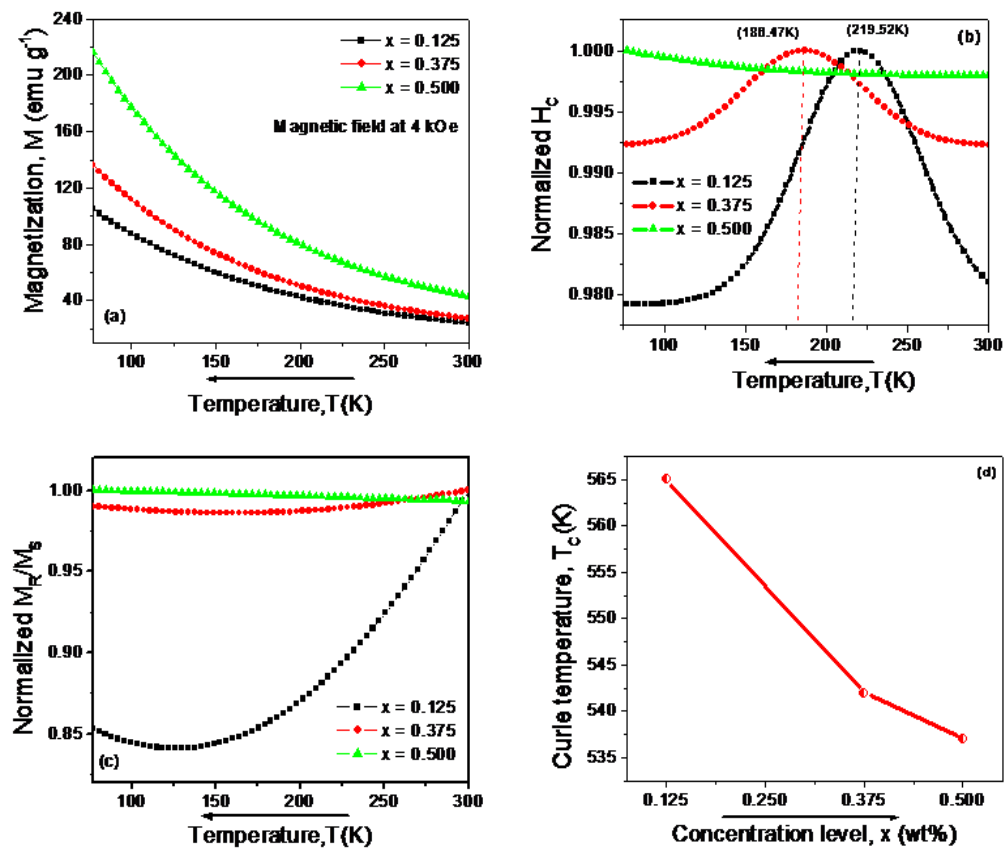


Fig.4.13: (a) $M - T$ curves (b) $H_c - T$ curves (c) $M_R/M_S - T$ curves for the investigated samples of composition, $\text{Co}_{1+x}\text{Mn}_x\text{Fe}_{2-x}\text{O}_4$ in the temperature range 77K – 300K (d) $T_c - x$ curve of $\text{Co}_{1+x}\text{Mn}_x\text{Fe}_{2-x}\text{O}_4$

As seen in the Fig.4.13 (b), the coercivity, H_c is found to increase with the drop in temperature, T for the samples of $x = 0.125$ and 0.375 up to a certain peak at 219.52K and 186.47K respectively and decrease up to around 125K. But, a continual increase in H_c is noticed for the sample of $x = 0.5$. This increasing trend in H_c for all the samples is the normal behavior according to Kneller's law [93]. It implies that the smaller the particle size is the greater is the surface-to-volume ratio which leads to originate surface disorder and contributes to an increase in anisotropy of the ferri/ferromagnetic materials [94]. So, while the temperature drops down from RT, this anisotropy energy becomes dominant over the thermal energy, which increases the coercivity, H_c . However, the decrease in H_c for the samples of $x = 0.125$ and 0.375 as mentioned above demonstrate a signature of superparamagnetic behavior which may have originated from the nanoparticles confinement effect and also is evident from the decreasing nature of remnant magnetization ratio, M_R/M_S with the

drop in temperature, T as seen in Fig.4.13 (c). The Curie temperature (T_C) has been estimated by extrapolating $M-T$ curves as shown in Fig.6.13 (a) for each sample of the investigated composition and found to decrease almost linearly with the increase of the concentration levels, x as presented in Fig.4.13(d). This nature in the variation of T_C is consistent with the observations as reported in the literature [95].

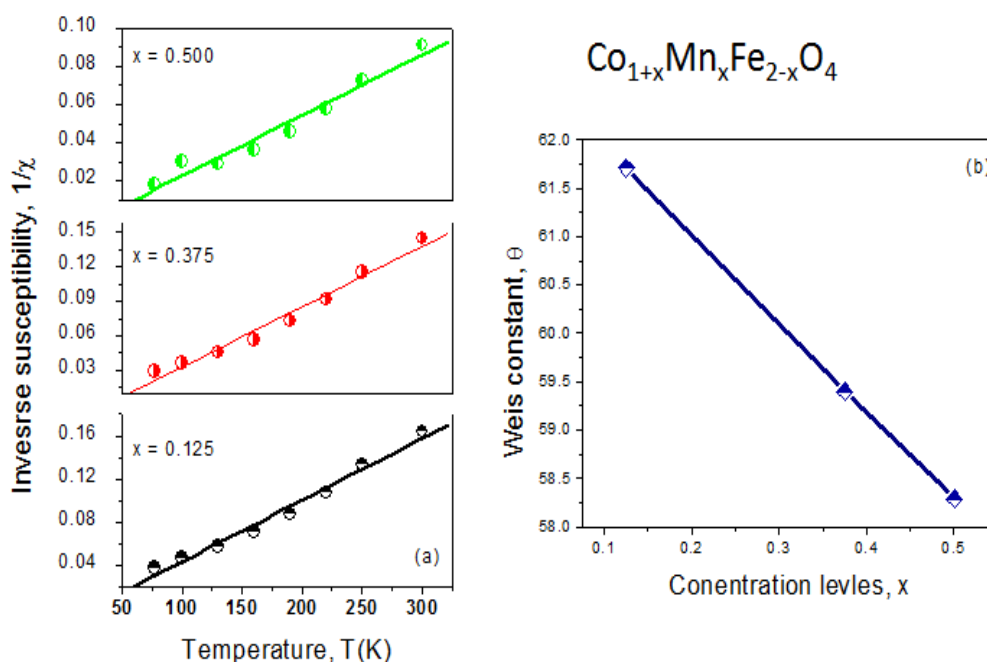


Fig.4.14: (a) $1/\chi - T$ curves (b) $\theta - x$ curves for investigated samples of composition $\text{Co}_{1+x}\text{Mn}_x\text{Fe}_{2-x}\text{O}_4$

Fig.4.14 (a) shows the Curie-Weiss plot, which represents $1/\chi$ as a function of temperature. The inverse of susceptibility i.e. $1/\chi$ is found to be almost linear with the increase in temperature. The inverse of the slope of $1/\chi$ vs. T curve (Curie-Weiss plot) represents the Curie constant (C) and the intercept at the temperature axis indicates the Weiss constant (θ). After linear fitting, the Curie constants of the investigated samples for all three Mn content (x) have been determined from their respective slope and found to be independent of Mn content (x). The Weiss constant, θ has also been evaluated from their corresponding intercepts on their temperature (T) axis and observed to be greater than 0 i.e. $\theta > 0$, which are the ferri/ferromagnetic signature of the material [96]. It is known that when the value of θ becomes zero i.e. $\theta = 0$, the material exhibits paramagnetic behavior [85]. Fig.4.14(b) shows the variation of Weiss constant, θ as a function of Mn content (x). From this Fig.4.14 (b),

the Weiss constant, θ is found to decrease linearly with the increase of Mn content (x) and demonstrating that the magnetic behavior of the investigated samples tending towards the paramagnetic behavior, which is expected to cause from the dilution effect of Mn^{2+} in the B site. However, a similar variation in μ_i is marked with the drop in temperature as in M. All the magnetic parameters as estimated from the dc magnetization measurements are listed in the Table-4.7:

Table 4.7: The magnetic parameters for samples of $Co_{1+x}Mn_xFe_{2-x}O_4$ in the low temperature regime (77- 3K)

Magnetic Parameters	300 K	250 K	220 K	190 K	160 K	130 K	100 K	77 K
<u>For x = 0.125</u>								
M_S emu/g	23.63	30.23	37.25	45.89	56.54	69.66	85.82	105.73
H_{COe}	24.87	25.25	25.28	25.26	25.00	24.66	24.91	24.88
M_R emu/g	1.96	1.18	1.45	1.79	2.20	2.70	3.34	4.09
K_{eff} erg/Oe	612.16	795.33	981.28	1207.9	1472.7	1789.8	2227.3	2740.5
n_B	1.02	1.31	1.61	1.98	2.44	3.01	3.71	4.57
T_C	565 K							
<u>For x = 0.375</u>								
M_S emu/g	28.60	34.83	43.79	55.04	69.19	86.97	109.32	137.42
H_{COe}	49.21	49.39	49.58	49.60	49.68	49.36	49.10	49.56
M_R emu/g	2.49	3.12	3.90	4.91	6.17	7.73	9.73	12.29
K_{eff} erg/Oe	1466	1792.6	2261.7	2844.1	3581.2	4472.7	5592.2	7095.6
n_B	1.31	1.59	2.01	2.52	3.17	3.99	5.01	6.30
T_C	542 K							
<u>For x = 0.500</u>								
M_S emu/g	41.38	55.29	69.50	87.36	109.82	138.04	173.52	218.12
H_{COe}	18.41	18.18	18.40	18.43	18.33	18.29	18.42	18.36
M_R emu/g	1.31	1.65	2.08	2.59	3.349	4.11	5.22	6.56
K_{eff} erg/Oe	793.5	1047.2	1332.5	1677.29	2097.47	2631.43	3330.65	4172.74
n_B	1.95	2.61	3.28	4.12	5.18	6.51	8.19	10.29
T_C	537 K							

4.2.3 Electric Properties

To analyze the electric properties of the materials, the Waynekerr impedance analyzer (model 6500B) was used to measure/determine the dielectric constant and resistivity using the disc-shaped samples of $\text{Co}_{1+x}\text{Mn}_x\text{Fe}_{2-x}\text{O}_4$ at different concentration levels, $0.125 \leq x \leq 0.5$ under the variations of both frequency (1kHz – 1MHz) and temperature (77k – 300K in the low-temperature regime and 320K – 390K in high-temperature regime). Their dc resistivity was also measured by the conventional 4-probe technique as a function of both temperature and magnetic field. A comparative study is made on dielectric constant and resistivity of the subject materials under varying conditions like sintering temperatures and milling times. However, the significant findings on the analysis of the electrical properties of the investigated samples of $\text{Co}_{1+x}\text{Mn}_x\text{Fe}_{2-x}\text{O}_4$ composition are presented in a quest for finding their suitability to be used in diversified applications.

4.2.3.1 Dielectric constant

4.2.3.1.1 Frequency response of dielectric constant

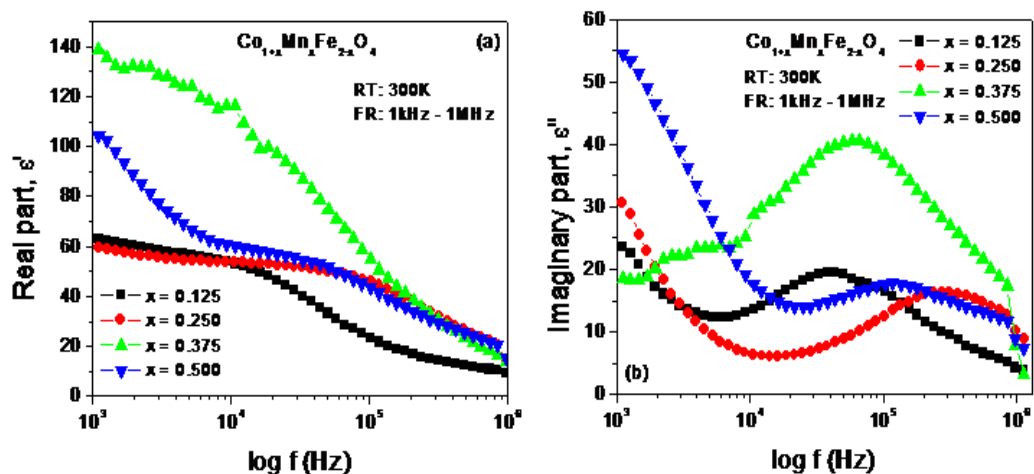


Fig.4.15: (a) Real part of complex dielectric constant, ϵ' as a function of frequency (b) Imaginary part of complex dielectric constant, ϵ'' as a function of frequency at room temperature in the frequency range 1 kHz – 1MHz

The dielectric constant is one of the electromagnetic parameters, which arises in the material from the four mechanisms of polarization such as dipole polarization, interfacial (space charge) polarization, ionic polarization, and electronic polarization. In the a.c. electric field, the dielectric constant becomes a complex quantity as

described by the relation $\varepsilon = \varepsilon' - j\varepsilon''$, where ε' is the real part responsible for storing electrical energy, and ε'' is the imaginary part related to the dissipation of electrical energy in the form of heat [97]. So the frequency and temperature response of complex dielectric constant in the material may govern their electromagnetic behavior. Fig.4.15 shows the variation of both the ε' and ε'' of complex dielectric constant as a function of applied frequency in the frequency band 1kHz – 1MHz at room temperature (RT). In the low-frequency regime, ε' is found to decrease non-linearly with the increase of applied frequency up to around 400 kHz and afterward, a slight decreasing trend is noticed with the further increase in frequency as seen in Fig.4.15(a). This decreasing trend in ε' implies that the material is ferrimagnetic nature. This is typical behavior of ferrites and it can be explained with the help of the Maxwell-Wagner model. According to this model, ferrites consist of two layers, first of which contain well-conducting grains (ferrous ions), and the second one is composed of poorly conducting grain boundaries. These grain boundaries are more active at lower frequencies; hence, the hopping frequency of electrons between Fe^{3+} and Fe^{2+} ions is less at lower frequencies. The dielectric properties of ferrites cause localized accumulation of charge under the influence of the electric field. The polarization in ferrites is similar to the conduction of electrons in Fe^{2+} and Fe^{3+} . At lower frequencies the conduction is favorable and, as a result, the dielectric constant is high but it continuously decreases with increasing frequency because the electron exchange between Fe^{2+} and Fe^{3+} cannot follow the higher AC field frequency [98]. The unpredictable and irregular variations in ε' is expected to arise from the presence of both Co^{2+} (low mobility) and Fe^{3+} (high mobility) charge carriers resulting in the random orientations of dipolar polarization across the grain boundaries according to Koop's phenomenological theory. However, the independency of ε' above 400 kHz may cause by the only contributions of electronic polarization. Fig.4.15 (b) shows the dispersion of ε'' and exhibits a normal frequency response from their broadened peaks. This implies a decrease in ε'' with the increase of applied frequency and may be assumed to cause by the decrease of relaxation [71]. On the left side of those peaks of ε'' in their dispersion demonstrate an anomalous behavior in the low-frequency regime due to the coexistence of antiferromagnetic and ferromagnetic interactions across the grain boundaries. However, the appearance of peaks in the $\varepsilon''(f)$ spectra show the grain boundary contributions to their

resistivity that in turn corresponds to the thermal energy dissipation. However, the prominent peak in the $\varepsilon''(f)$ spectra are observed at the concentration level, $x = 0.375$, which may have a possibility to be used in hyperthermia or related research in medical science [99].

4.2.3.1.2 Temperature response of dielectric constant

The temperature dependence of dielectric constant at the selected frequency of 10 kHz is illustrated in Fig.4.16 for the investigated samples in the low-temperature regime ranging from 77K – 300K. As seen in Fig.4.16 (a) and (b), the decreasing trend both in ε' and ε'' is observed with the drop in temperature up to around 150 K and down below they are seen to remain almost independent of temperature.

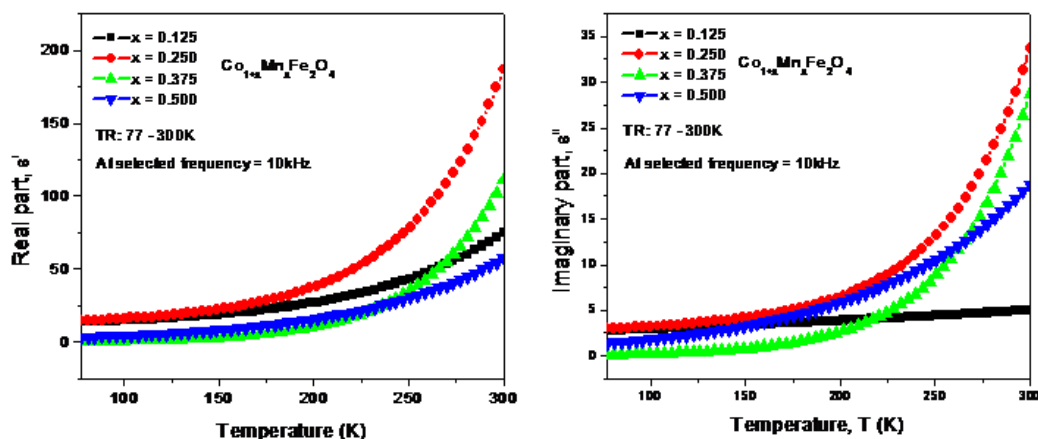


Fig.4.16: (a) Real part of dielectric constant, ε' as a function of temperature (b) Imaginary part of dielectric constant, ε'' as a function of temperature at selected frequency 10 kHz in the low-temperature regime (77K – 300K)

In general, the dielectric properties of the material is dominated by the grain boundaries and attributed to the Maxwell-Wagner space charge polarization (interfacial polarization contribution) following the Koop's phenomenological theory. So, the decrease in ε' while the temperature drop from the room temperature (RT) may be assumed to cause by the reduction of space charge polarization effect due to the lesser accumulation of charge carriers ($\text{Co}^{2+}/\text{Fe}^{3+}$) across the grain boundaries. However, its constancy may be due to the only presence of the electronic polarization, which is completely independent of temperature. The similar variations as observed in ε'' may originate from the lesser dipolar polarization and DC losses

across the grain boundaries. The variations in both ϵ' and ϵ'' with the concentration level, x are found to be irregular and unpredictable, which may have arisen from the coexistence of antiferromagnetic and ferromagnetic clusters [100] due to their non-stoichiometry. To understand and explain the high-temperature response of dielectric constant, a representative sample of concentration level $x = 0.125$ has been taken into consideration. Fig.4.17 shows the temperature dependence of dielectric constant for the said representative sample at selected frequencies 100Hz, 1kHz, 10kHz, 100kHz, and 1MHz in the high-temperature regime ranging from 320K–400K.

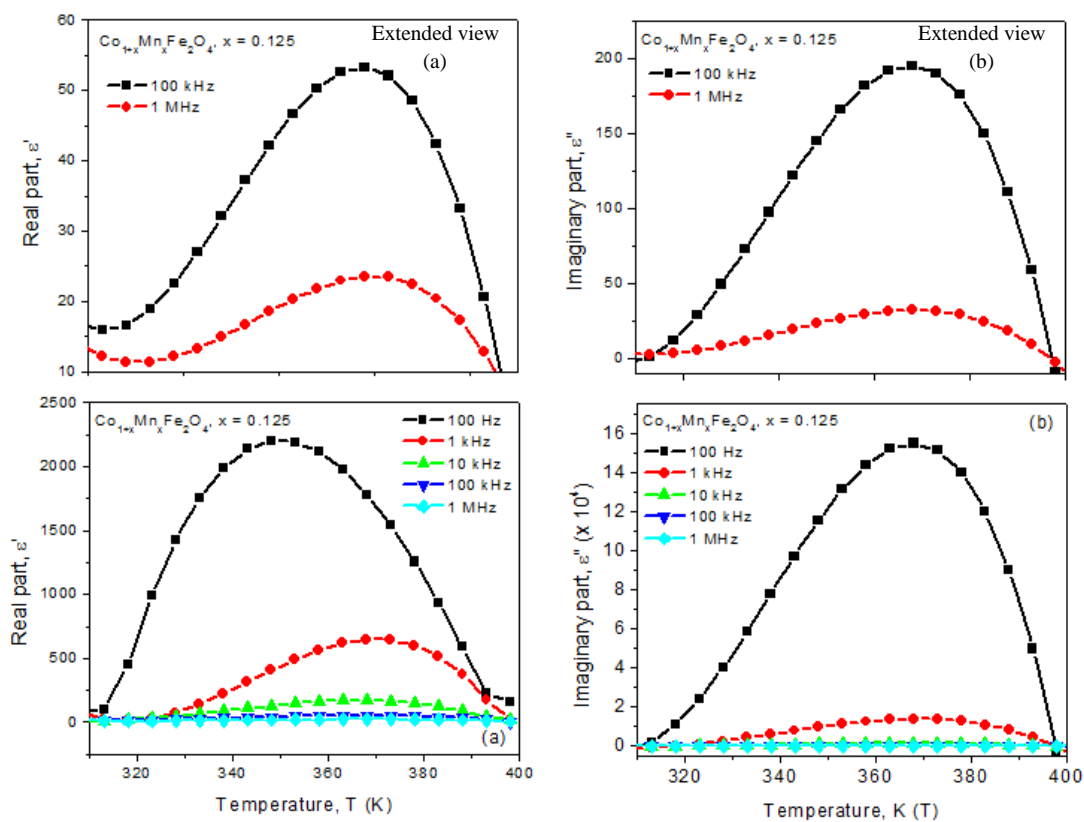


Fig.4.17: (a) Real part of dielectric constant, ϵ' as a function of temperature (b) Imaginary part of dielectric constant, ϵ'' as a function of temperature for $x = 0.125$ of $\text{Co}_{1+x}\text{Mn}_x\text{Fe}_{2-x}\text{O}_4$ in the high-temperature regime 310K – 400K

At lower temperature, both the real (ϵ') and imaginary (ϵ'') parts of dielectric constant are found to increase for all the selected frequencies as seen in Fig.4.17(a) and Fig. 4.17 (b). At higher temperatures, both of them are found to decrease from their different peak (temperature) points. This nature of variation in dielectric constant, ϵ' is contrary to the previous results of indium substituted cobalt ferrite as

reported in the literature [80, 101] and therefore unique and significant. At lower but above RT, the initial increase in ϵ' is likely to originate from the additional contributions of interfacial and dipolar polarization, strongly temperature-dependent, due to a larger concentration of p-type (Co^{2+}) carriers in the B site because of non-stoichiometric composition. At higher temperature, the thermal energy, supplied by the temperature boosts the mobility of charge carriers that enhances the hopping rate between A and B site and causing to reduce the interfacial polarization across the grain boundary [80, 102]. This phenomenon decreases both ϵ' and ϵ'' at higher temperatures. The behavior of both ϵ' and ϵ'' with frequency can be ascribed to the four mechanisms of polarization. At higher frequency, the electronic mechanism of polarization is only present in dielectric constant whereas at lower frequencies other three mechanisms contribute to the rapid increase of dielectric constant as explained in literature [103]. The relaxation time (τ) was estimated from the peaks of ϵ' in the ϵ' vs T curves as shown in Figure 4.17(a) using the values of ϵ'' at corresponding temperature from ϵ'' vs T curves as shown in Fig.4.17(b) at selected frequencies by the equation $\omega\epsilon'' = \epsilon'(\omega)$, modified from the Debye formula [104] since $\epsilon'_\infty \sim 0$. The estimated values are listed in Table-6.8.

Table 4.8: Relaxation time constant (τ) and activation energy, E_a for $x=0.125$ of $\text{Co}_{1+x}\text{Mn}_x\text{Fe}_{2-x}\text{O}_4$

Parameters	100 Hz	1kHz	10kHz	100 kHz	1 MHz
Relaxation time, τ	30.28 μs	6.70 μs	1.74 μs	0.47 μs	0.19 μs
Activation energy, E_a	0.27 eV	0.31 eV	0.34 eV	0.38 eV	0.40 eV

As seen in this Table-4.8, the relaxation time (τ) for the representative sample of $\text{Co}_{1+x}\text{Mn}_x\text{Fe}_{2-x}\text{O}_4$ (non-stoichiometric composition) decreases with the increase in applied frequency, which is normal and further confirmation of their dielectric behavior. The activation energy, E_a at room temperature (300 K) is estimated from the relaxation time, τ at different selected frequencies using Arrhenius equation $\tau = \tau_0 e^{\frac{-E_a}{kT}}$ considering $\tau_0 = 1$, and listed in Table-4.8. This activation energy, E_a is observed to increase with the applied frequency. This implies the possible reduction in the hopping rate across the grain boundaries with the frequency at room temperature due to the slower mobility of Co^{2+} (p-type carriers) ions [72, 73, 80].

4.2.3.2 Complex electric modulus

The complex modulus formalism is extensively used for the purposes such as (i) to identify and understand the bulk properties, electrical conductivity, and relaxation time (ii) to differentiate the grain and grain boundary conduction process from the electrode polarization effect, and (iii) microstructural correlation in both the electrical and magnetic properties of the materials [4]. The electric modulus of the samples was calculated from the values of their real and imaginary parts of permittivity (dielectric constant) using the formalism, $M' = \omega C_0 \epsilon'$ and $M'' = \omega C_0 \epsilon''$, where C_0 is the geometric capacitance, ϵ' , the real part, and ϵ'' the imaginary part of permittivity.

4.2.3.2.1 Frequency response of electric modulus

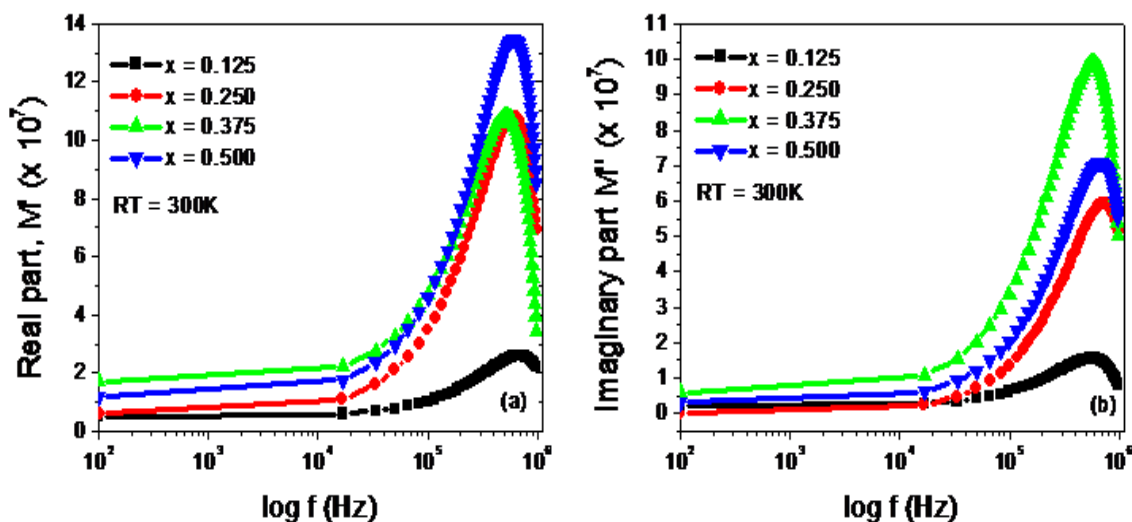


Fig.4.18: (a) M' vs $\log f$ curves (b) M'' vs $\log f$ curves at room temperature for the representative samples of $\text{Co}_{1+x}\text{Mn}_x\text{Fe}_{2-x}\text{O}_4$

Fig.4.18 (a) shows the variation in the real part of electric modulus, M' with the frequency. As seen in this figure, the real part M' approaches to almost zero and signifying the absence of electrode contribution and small polarons to the conduction mechanism for all the representative samples [72, 73]. A continuous increase in M' is observed up to a certain peak and then sharply falls. The sharp peaks are observed to separate the M' spectra into two wings. They may be designated as wing-I and wing-II respectively for better understanding. The wing-I corresponds to the frequency

band below the peak frequency and wing-II to a frequency band above it as evident in Fig.4.18 (a). The increasing trend in $M'(f)$ spectra with the frequency in the wing-I may be attributed to the combined effects of the slower mobility of p-type carriers and broadening of hopping lengths L_A and L_B in both sites due to the comparatively larger crystallite/grain size, D_x [73] from the previously reported values of the similar kind of materials [85]. This wing-I may accordingly correspond to long-range mobility, which refers to the slower process related to the migration of charge carriers by diffusion through the grain boundaries [105]. Conversely, the sharp decreasing trend of M' in the wing-II may be ascribed to the shortening of hopping length L_B that causes the faster hopping between charge carriers (p-type and n-type) across the grain boundaries in the B- site [106]. This wing-II may, therefore, imply short-range mobility, which is the faster process associated with the confinement of ions in their potential well, and localized motion of them [102]. Hence, the increasing trend in wing-I and decreasing trend in wing-II are the signature of the diminution and enrichment in conductivity respectively and found to well match to the dielectric behavior of the material. The well-resolved peaks are observed in M' spectra as seen in Fig.4.18 (a). The irregular changes in their peak positions are also marked with the concentration level x , which may be due to the redistribution of cations among the A and B sites during the phase formation that causes a small deviation from their presumed idealistic distribution. The irregular changes in their peak positions are also marked with the concentration level x . The frequencies correspond to the peaks in M' spectra may be defined as the critical frequency, f_c . This frequency may mark the boundary between the long-range mobility (wing-I) and short-range mobility (wing-II) of charge carriers. Thus it may determine the critical dielectric relaxation time by the formalism $\tau_c = 1/2\pi f_c$ at constant electric displacement in the material, which seems to set the boundary between the contributions of n-type (Fe^{2+}/Fe^{3+}) and p-type (Co^{2+}/Co^{3+}) charge carriers in their conduction/hopping mechanism of the material. Fig.4.18 (b) shows the variation of M'' with the increase in the frequency of the applied field on a logarithmic scale. This increasing trend implies the increase in the imaginary part of permittivity. As seen in this figure, the well-resolved peaks are observed in $M''(f)$ spectra in the high-frequency region due to the resonance effect, which implies equality in both the real part and imaginary part of complex permittivity at a particular frequency. This resonance occurs when the jumping

frequency of localized charge carriers (electrons) becomes equal to the frequency of the applied electric field [9, 73]. These peaks are also found to appear at different positions with varying concentration levels, x , because of cation redistribution similar to the reason as mentioned above. Besides, the enhancement in the magnitude of these peaks is marked to follow the increasing trend but not in a regular manner. This increased magnitude of M'' at their resonance implies the decreased density of oxygen ions in this non-stoichiometric composition and resulting in the faster hopping between Fe^{2+} and Fe^{3+} ions in the conductive grains. Thus the increased conductivity at resonance may cause eddy current loss as heat energy. However, the frequency corresponding to each peak in the $M''(f)$ spectra are known as maximum characteristic frequency, f_{max} for each composition, which governs the dielectric relaxation in the material at constant electric displacement and thereby determines their relaxation time by the formalism $\tau_{Max} = 1/2\pi f_{max}$ [102, 104]. Moreover, the activation energy E_a has also been calculated for different concentration levels x by using the relaxation decay law at room temperature. The estimated values of f_c , τ_c , f_{max} , τ_{Max} , and E_a are listed in Table-4.9:

Table-4.9: Critical frequency (f_c), critical relaxation time constant (τ_c), characteristic frequency (f_{max}), relaxation time constant (τ_{Max}), and activation energy (E_a)

Parameters	Concentration level, x			
	$x = 0.125$	$x = 0.25$	$x = 0.375$	$x = 0.5$
Critical frequency, f_c	661 kHz	664 kHz	537 kHz	594 kHz
Critical relaxation time constant, τ_c	0.241 μs	0.247 μs	0.296 μs	0.268 μs
Characteristic frequency, f_{Max}	628 kHz	774 kHz	580 kHz	678 kHz
Dielectric relaxation time, τ_{Max}	0.253 μs	0.206 μs	0.274 μs	0.235 μs
Activation energy E_a at RT	0.355 eV	0.408 eV	0.335 eV	0.374 eV

As seen in Table-4.9, the critical relaxation time constant (τ_c) and dielectric relaxation time constant (τ_{Max}) is found to depend on the concentration levels, x but not in a regular nature. However, the critical relaxation time constant τ_c sets the boundary below of which the n-type carriers may be dominant in hopping mechanism and above it p-type carriers for a particular composition. The activation energy E_a is found to depend on the concentration level x in a non-regular pattern.

However, the activation energy E_a is marked to be lowest for the sample of $x = 0.375$. This lowest value in E_a signifies faster hopping between Fe^{3+} and Fe^{2+} ions in the conductive grains according to Koop's phenomenological theory as evident also from the corresponding curve as seen in Fig.6.18(b), which may be associated with the deficiencies of oxygen ions in the B-site due to the additional density of Co^{2+} ions because of their non-stoichiometry [72].

4.2.3.2.2 Temperature response of electric modulus

The temperature dependence of dielectric relaxation behavior is illustrated by the normalized $M''/M''_{Max}(f)$ spectra for a representative sample of $\text{Co}_{1+x}\text{Mn}_x\text{Fe}_{2-x}\text{O}_4$ at constant $x=0.125$ at different selected temperatures 300K, 217K, 187K, 157K, 117K, and 77K as shown in Fig.4.19 (a). The shifting of peaks in $M''/M''_{Max}(f)$ spectra are found to depend on the temperature. The characteristic dielectric relaxation time constant τ_{Max} has been evaluated from their corresponding characteristic frequency and presented their fitted values as a function of temperature as shown in Fig.4.19 (b).

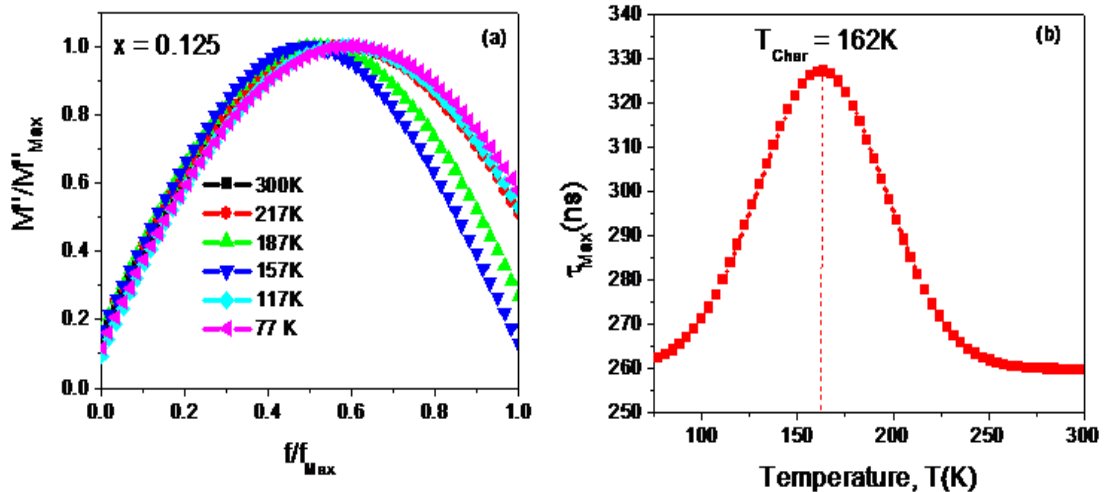


Fig.4.19: (a) M''/M''_{Max} vs f/f_{Max} curves (b) τ_{Max} vs f curves samples of $\text{Co}_{1+x}\text{Mn}_x\text{Fe}_{2-x}\text{O}_4$ for $x = 0.125$ in the temperature range 77K – 300K

As seen in this plot of Fig.6.19 (b) that there may be a characteristic temperature T_{Char} at around 162K that sets the possible boundary between long-range mobility and short-range mobility of charge carriers/ions [73]. Since the activation energy is the minimum energy required to provide conductivity in the

material, so there may be definite activation energy, E_a at this characteristic temperature T_{Char} . This activation energy has been enumerated from the Arrhenius equation $\tau_{Max} = \tau_0 \exp\left(-\frac{E_a}{kT}\right)$ taking τ_0 as prefactor ($=1$) at the characteristic temperature T_{Char} and found to be 0.15eV. Besides, two slopes are noticed to appear due to this characteristic temperature T_{Char} in τ_{Max} vs T curve as seen in Fig.6.19 (b). The slope in the lower temperature region from this characteristic temperature T_{Char} corresponds to wing-I, and the slope above the characteristic temperature T_{Char} to wing-II. Hence the value of the activation energy E_a has been estimated from the slope of each wing after linear fitting to $\ln \tau_{Max}$ vs T^{-1} curve (not shown), which are found to follow the Arrhenius equation. The estimated values of activation energy E_a are found to be 0.078 eV and 0.025 eV in the wing-I and wing-II respectively. The lower value of E_a in the wing-II implies the faster hopping of charge carriers in the conduction mechanism of materials, which may be due to the thermal agitation for comparatively increased temperature [73].

4.2.3.3 Resistivity

4.2.3.3.1 AC resistivity

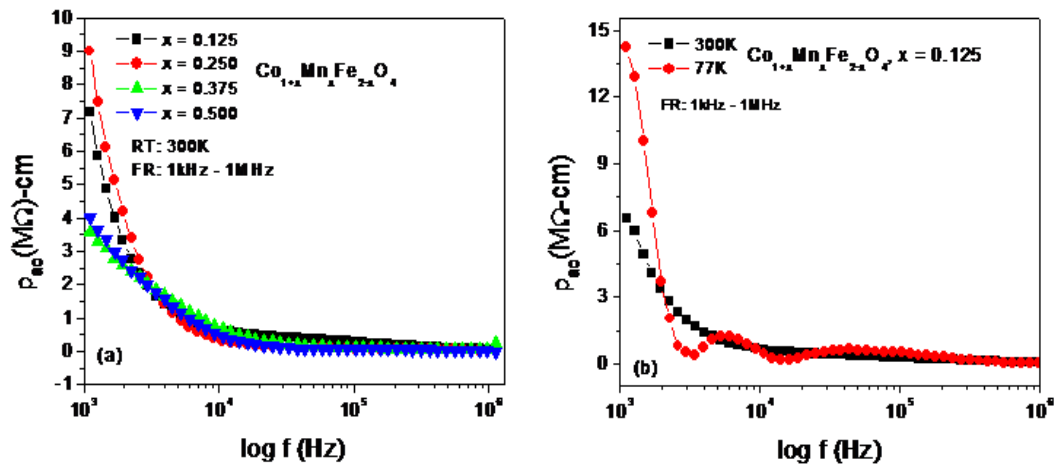


Fig.4.20: (a) AC resistivity as a function of frequency at room temperature (RT) (b) Normalized ac resistivity for the sample of $x = 0.125$ as a function of frequency at RT and liquid nitrogen temperature (LNGT) in the frequency range 1kHz – 1MHz

Fig.4.20 (a) shows the variation in ac resistivity of $\text{Co}_{1+x}\text{Mn}_x\text{Fe}_{2-x}\text{O}_4$, where $0.125 \leq x \leq 0.5$ with the increase in applied frequency on a logarithmic scale

at room temperature (RT). Almost an exponentially decreasing trend in their ac resistivity ρ_{ac} is observed with the increase in applied frequency up to around 18 kHz and afterward, it becomes independent of frequency as seen in Fig.4.20 (a). This decreasing trend may be attributed to the increasing effect of multilayer capacitances according to Koop's phenomenological theory [80]. However, in the low-frequency regime, the variation in ρ_{ac} with the concentration level, x is observed to be irregular and unpredictable, which may have caused by the deviation in their cation redistribution. To understand the temperature effect, Fig.4.20(b) shows the normalized resistivity ρ_{ac} as a function of frequency at selected temperatures 300K (RT) and 77K (LNGT) for the sample of $x = 0.125$. The similar nature in the variation of ρ_{ac} is marked with the applied frequency up to around 100 kHz and then to remain independent of frequency. However, the increased value of ρ_{ac} is found to occur at the liquid nitrogen temperature (LNGT) 77K compared to that at the room temperature (RT) 300K due to decreased hopping rate because of slower mobility of p-type carriers across the grain boundaries in the low frequency regime [107]. This variation nature of ρ_{ac} implies the negative temperature coefficient of resistnce (NTRC) and thus demonstrate the semiconducting behavior of the material in the low frequency and temperature regime. The wavy nature in the variation of ρ_{ac} in the lower frequencies at 77K is expected to arise due to the difference in the response to the applied frequencies between Fe^{2+} and Co^{2+} ions because of their coexistence in the grain boundaries [100].

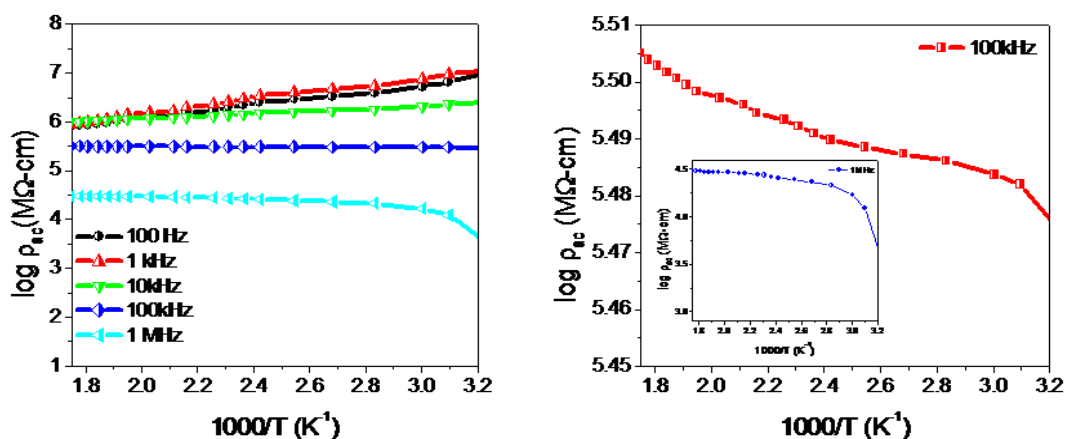


Fig.6.21: AC resistivity as a function of temperature for the sample of $x = 0.125$ (a) at selected frequencies 100Hz, 1kHz, 10kHz, 100kHz and 1MHz (b) at selected frequencies 100kHz (inset 1MHz) (300K-400K)

Fig.4.21 shows the ac resistivity (ρ_{ac}) in $\text{Co}_{1+x}\text{Mn}_x\text{Fe}_{2-x}\text{O}_4$ for $x= 0.125$ at selected frequencies in the temperature range 300K – 400K. The ac resistivity (ρ_{ac}) is found to decrease with the increase in temperature at selected frequencies 100 Hz, 1kHz, and 10 kHz as shown in Fig.4.21(a). This decrease in ρ_{ac} exhibits the semiconductor behavior whereas the same is found to increase with temperature at 100 kHz and 1 MHz as shown in Fig.4.21 (b), which implies the insulator behavior and displaying the signature of second-order phase transition from the ferrimagnetic-to-paramagnetic phase. The decrease in ρ_{ac} with temperature as usually can be attributed to the thermally activated increased mobility of charge carriers that results in more transfer of electrons from one ion to another as explained in literature [108]. However, the increase in ρ_{ac} with the temperature at 100 kHz and 1MHz is expected to cause by the slower mobility of the greater concentration of Co^{2+} ions (p-type carriers) in the B site due to its non-stoichiometry. These p-type carriers could not follow the ac field variation at higher frequencies (100 kHz and 1 MHz) and ultimately result in Warburg impedance in the grain boundaries due to their accumulation across the grain boundaries. These accumulated charge carriers prohibit the charge transportation by hopping mechanism and thus cause an increase in ρ_{ac} .

4.2.3.3.2 DC resistivity

The dc resistivity (ρ) of the $\text{Co}_{1+x}\text{Mn}_x\text{Fe}_{2-x}\text{O}_4$ at $x = 0.125$ was estimated from the measurement of resistance using the conventional 4-probe method at different temperatures ranging from 320K – 400K in the high-temperature regime. The estimated values of ρ are plotted as a function of temperature as shown in Fig.4.22 (a). An almost linear decreasing trend in ρ exhibit the materials to be semiconducting in the high-temperature regime. This nature of variation in ρ may be attributed to the concurrent contribution of both the n-type ($\text{Fe}^{2+}/\text{Fe}^{3+}$) and p-type ($\text{Co}^{2+}/\text{Co}^{3+}$) charge carriers accumulated across the grain boundaries due to their non-stoichiometry. These accumulated charges may cause their increased hopping by thermal agitation in the high-temperature regime. To understand the field dependence of resistivity, magnetoresistance (MR) was determined for a representative sample of $\text{Co}_{1+x}\text{Mn}_x\text{Fe}_{2-x}\text{O}_4$ at $x = 0.125$. The magnetoresistance is the change of a material's resistivity with an increasing magnetic field and described by the relation $MR = (\Delta\rho/\rho_{H=0})_T$, and

expressed in percentage. This magnetoresistance is an important magneto-transport property to identify the types of charge carriers and to probe the material's capability to control the electron transport properties in the sensor and spintronics applications. Fig.4.22 (b) shows the variations in MR of the investigated sample for the transverse and parallel field direction to the current at room temperature (RT). In both the direction, negative MR is obtained and found to increase with the increase of the magnetic field as shown in Fig. 4.22 (b). This variation nature in MR is found to exhibit normal behavior that implies the weak localized system [109, 110] and almost in agreement with the previously reported results of this kind of material. The negative value of MR entails the dominance of n-type carriers i.e. Fe^{3+} ions in the hopping process of this system. This fact is confirmed from the decrease of normalized resistivity with the increase of magnetic field as shown in Fig.4.22 (c), which may be ascribed to the weakening of spin-orbit coupling under the influence of the externally applied magnetic field. However, the observed large value of negative MR, compared to other such ferromagnetic materials is expected to arise from the spin-dependent electron scattering due to the field-induced change of the canting angle of manganese spins for the inherent antiferromagnetic effect of Mn^{2+} in the B site [102]. Besides, the marked difference in MR is observed between the transverse and parallel directions to the current, which can be explained based on the cross-section for scattering in the ferromagnetic materials. If the field and magnetization are oriented transverse to the current, then the electronic orbits are in the plane of the current, and there is a small cross-section for scattering, giving a low resistance state. Conversely for a field applied parallel to the current, the electronic orbits are oriented perpendicular to the current, and the cross-section for scattering is increased, giving a high resistance state [111]. Furthermore, the rate of change of resistivity with the increase of the applied magnetic field as shown in Fig. 4.22(d) is expected to cause by the combined effects of the faster hopping of Fe^{2+} ions (n-type carriers) across the grain boundaries and the higher mobility of n-type carriers. The higher rate of change of resistivity in the low field region may make this sample more suitable to be used in the field of position sensor and biosensor applications.

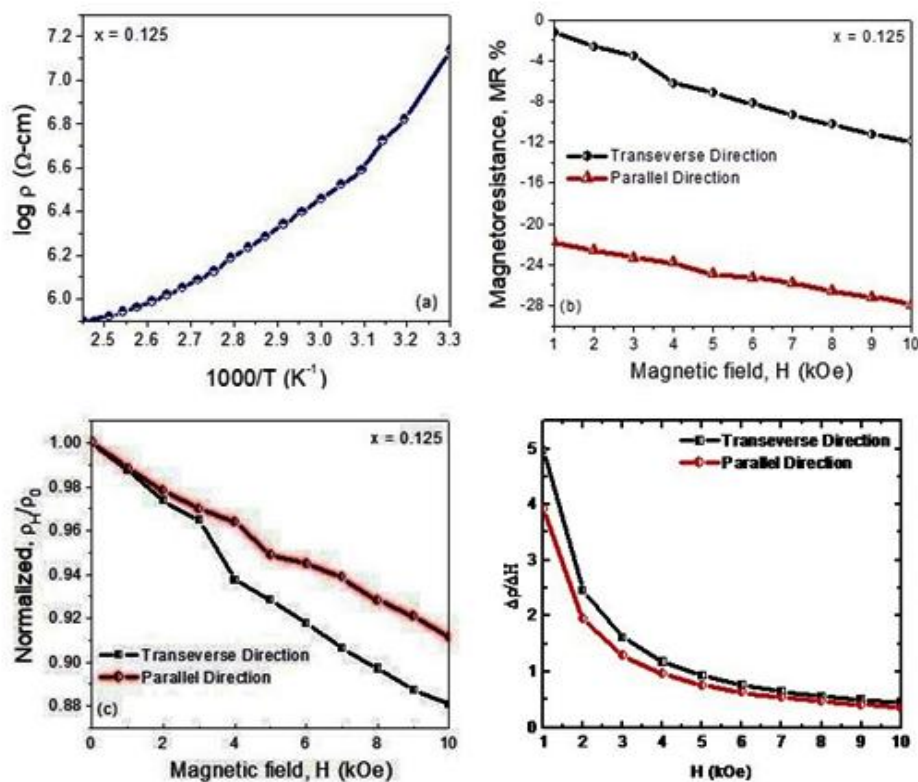


Fig.4.22: (a) Resistivity as a function of temperature (b) Magnetoresistance, MR% as a function of the magnetic field (c) Normalized resistivity as a function of the magnetic field at RT, and (d) Rate of change of resistivity to the magnetic field ($\Delta\rho/\Delta H$) of the investigated sample with $x = 0.125$

4.2.3.4 Impedance and reactance

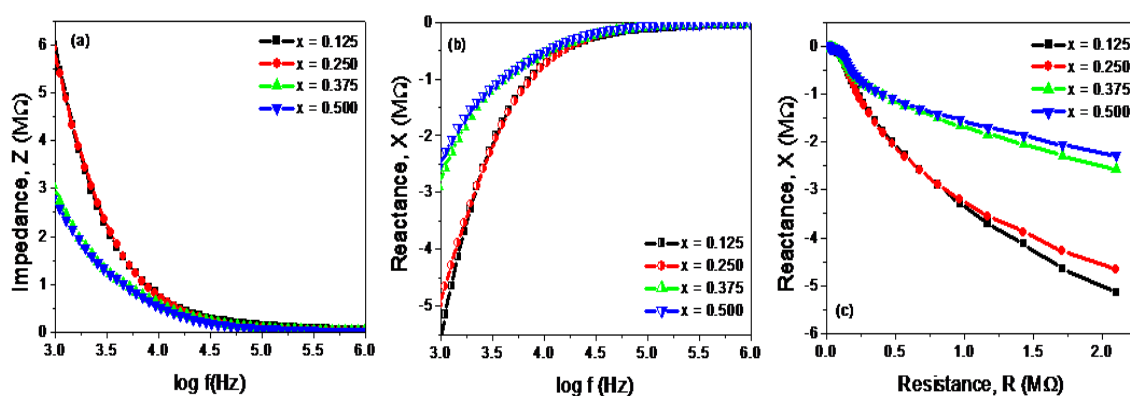


Fig.6.23: (a) Z vs $\log f$ curves (b) X vs $\log f$ curves (c) X vs R curves at room temperature for the samples of $x = 0.125, 0.25, 0.375, 0.5$ of $\text{Co}_{1+x}\text{Mn}_x\text{Fe}_{2-x}\text{O}_4$

Fig.4.23 shows the plot of (a) $Z - \log f$ (b) $X - \log f$ (c) $X - R$ for the non-stoichiometric samples of $x = 0.125, 0.25, 0.375, 0.5$ at room temperature to

understand the contribution of their grain boundaries and grains to the conduction mechanism. As seen in Fig.4.23 (a) the impedance, Z is found to decrease almost exponentially with the increase in applied frequency up to a certain frequency at around 45kHz and then merged to a single asymptotic value and seems to be independent of frequency in the higher frequency regime. This decreasing trend in impedance Z implies the higher conductivity of the material in the grains due to the higher mobility of charge carriers. Fig.4.23 (b) illustrates the reactance as a function of frequency, wherein it is seen that the negative value of reactance, X increases almost exponentially with the increase in applied frequency up to around 45 kHz and then remains independent of frequency. The negative values of X imply that the reactance, X is of capacitive type. The variation nature in X reflects the fact that the capacitance of the materials decreases with the increase in frequency due to increased hopping of charge carriers across the grain boundaries in the B- site. A plot of X vs R (equivalent to a plot Col-Col plot) is shown in Fig.4.23(c) which exhibits that both the reactance and resistance approaches to zero with the increase in applied frequency. This implies that the contribution of the grain to the electrical transport properties become dominant due to the higher mobility of charge carriers in the high-frequency regime. However, the reactance above a particular resistance at around 1.25 M Ω , is found to depend directly on the concentration levels, x , which demonstrates that the dielectric constant decreases due to short-range mobility in the lower frequency.

4.2.3.5 Cole-Cole Plot for structural correlation

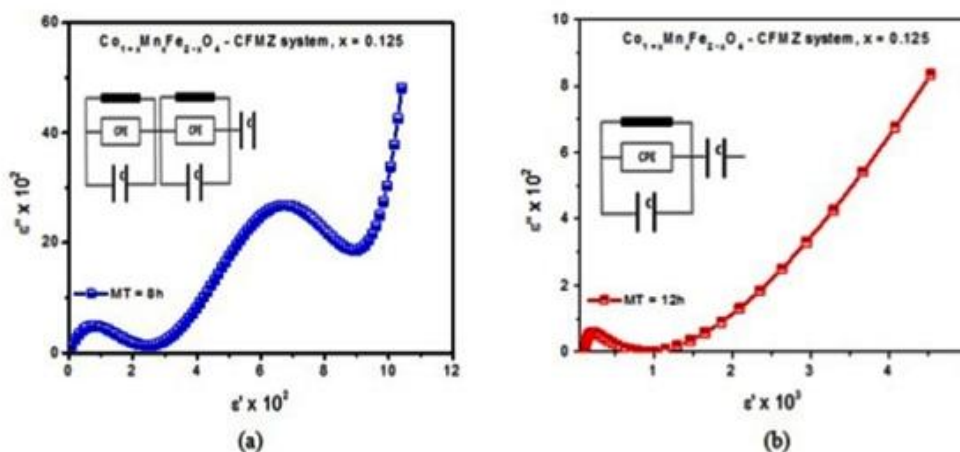


Fig.4.24: The Cole-Cole plot for (a) the sample of MT 8h (b) for the sample of MT 12h of the composition $\text{Co}_{1+x}\text{Mn}_x\text{Fe}_{2-x}\text{O}_4$ at $x = 0.125$

To analyze the structural correlation with the dielectric properties, the Cole-Cole plot for the representative samples of $\text{Co}_{1+x}\text{Mn}_x\text{Fe}_{2-x}\text{O}_4$ system at the same concentration level ($x=0.125$) but with different milling time (MT = 8h and 12h) are presented in Fig.6.26 along with their equivalent circuits (inset of respective figures). In Fig.4.24 (a) the Cole-Cole plot for the sample of milling time 8h shows the incomplete depressed two semicircles in the high-frequency regime. Two semicircles signify the contribution of grain boundary resistance and grain resistance with two different relaxation times of non-ideal Debye relaxation. The non-ideal Debye relaxation demands to include constant phase element (CPE) in parallel to the ideal resistor-capacitor (RC) circuit to fit the data. In the low-frequency regime, a straight line like spikes is observed, which may be thought of as another capacitance in series with the parallel combination of the RC circuit. Hence, for the two semicircles as obtained from the sample of MT 8h, the Cole-Cole equivalent circuit may be assumed of the series combination of two similar parallel RC circuits and a capacitor in series as shown in the inset of Fig.4.24 (a). However, as one semicircle corresponding to the grain resistance, along with a straight line like the spike is obtained for the sample of milling time 12h as shown in Fig.4.24(b). As such the corresponding Cole-Cole equivalent circuit may be thought of a single similar circuit in series with a capacitor as shown in the inset of Fig.4.24 (b). The appearance of double semicircles may have originated from the larger number of grain boundaries due to its larger particle size for the sample of milling time 8h as evident from the Table-4.4 [82, 106]. It is notable here that the presence of double semicircles indicates the mixed-phase spinel of the sample of milling time 8h whereas the single semicircle represents the single-phase spinel structure of the representative sample of 12h [82].

4.3 Stoichiometric composition $CoMn_xFe_{2-x}O_4$

In this composition, x refers to the Mn content that replaces Fe at the wt% 0.125, 0.25, 0.375, 0.5 that make this composition stoichiometric.

4.3.1 Crystallographic and Morphological analysis

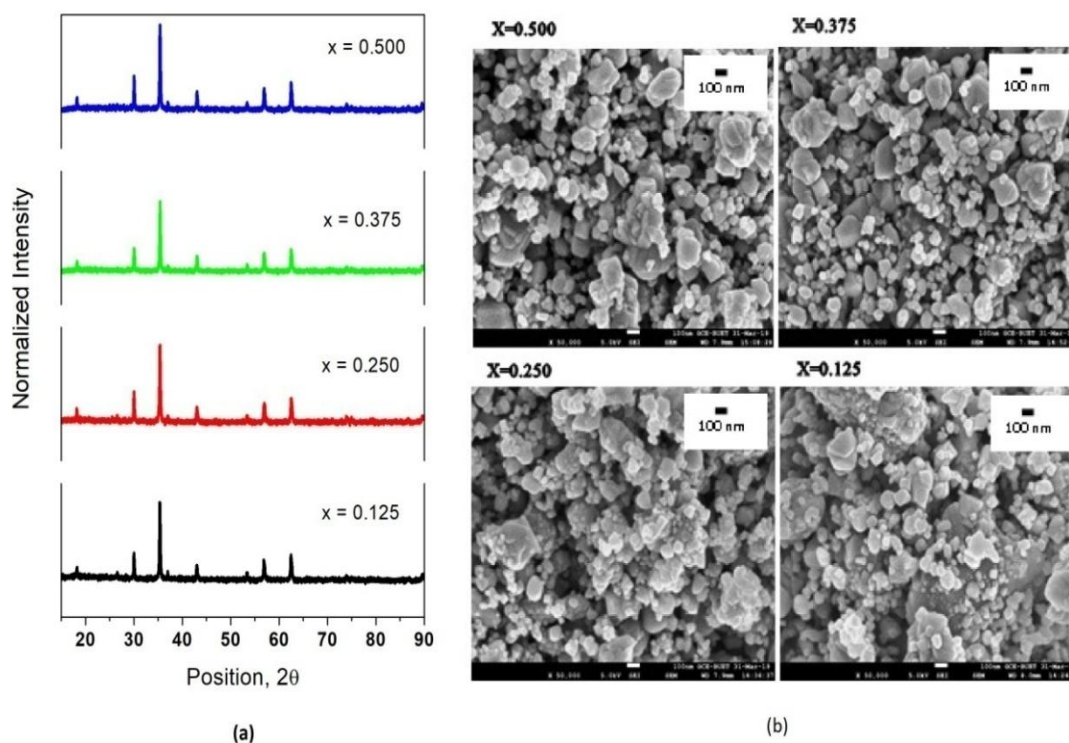


Fig.4.25: (a) X-ray diffraction patterns (b) FE-SEM Micrographs for the samples of $CoMn_xFe_{2-x}O_4$ within content (x) = 0.125, 0.25, 0.375 and 0.5

Fig.4.25 (a) shows the X-ray diffraction (XRD) patterns for the samples with different Mn content (x) = 0.125, 0.25, 0.375, 0.5. The observed peaks in the patterns are found to well match with the standards JCPDS card No. 22-1086 for $CoFe_2O_4$ and the planes of Mn substituted cobalt ferrite nanoparticles corresponding to Miller indices (111), (220), (311), (400), (422), (511) and (440) [72, 73, 82]. They are also closely resembled the standard crystal structure of $CoFe_2O_4$ from the International Centre for Diffraction Data (ICDD) number 221084, which belongs to the face-centered cubic spinel-type (Fd-3m) [112]. These planes indicate that the samples exhibit the single-phase cubic spinel structure. No impurity phase is observed in their EDS spectrum (not shown). The intense sharp peaks of the XRD

patterns confirm their crystallinity. The X'pertpro High Score Plus software was used to determine the peak position (2θ) and full width at half maximum (FWHM) of the strongest peak corresponding to the Miller plane (311). The strongest peak position, 2θ in their patterns is found to shift rightward (i.e. to slight increase) with the Mn content (x) but the full width at half maximum (FWHM) to remain the same as listed in the Table-4.10. This shift in the peak position signifies the changes in lattice constant associated with the d-spacing. The plane (311) has been used to estimate the lattice constant (a), the crystallite size (D_x), and the strain (ϵ) by using the usual formulas. Stanley's equations were used to estimate the hopping lengths and bond lengths [6, 82]. All these structural parameters are listed in the following Table-4.10 for crystallographic analysis:

Table-4.10: Different structural parameters of $\text{CoMn}_x\text{Fe}_{2-x}\text{O}_4$ as determined from the XRD patterns

Structural parameters	Concentration level, x			
	$x = 0.125$	$x = 0.25$	$x = 0.375$	$x = 0.5$
2θ of (311) plane	35.33	35.41	35.53	35.58
FWHM	0.156	0.156	0.156	0.156
$a(\text{\AA})$	8.415	8.397	8.370	8.358
$V_x(\text{\AA})^3$	596.07	592.17	586.38	583.99
D_x (nm)	53.424	53.436	53.454	53.462
ρ_x (gm cm^{-3})	4.750	4.779	4.824	4.842
$L_A(\text{\AA})$	3.644	3.636	3.624	3.619
$L_B(\text{\AA})$	2.975	2.969	2.959	2.955
A-O(\AA)	1.822	1.818	1.812	1.809
B-O(\AA)	2.103	2.099	2.092	2.089
Microstrain ϵ	0.002137	0.002132	0.002124	0.002121

From Table-4.10, the lattice constant (a) and other associated parameters such as unit cell volume (V_x), tetrahedral hopping length (L_A), octahedral hopping length (L_B), tetrahedral bond length (A-O), and octahedral bond length (B-O) are observed to decrease with the Mn content (x). The decrease in lattice constant, a , may be attributed to the combined effects of smaller ionic radius of Mn^{2+} (66\AA) that replaces

comparatively larger ionic radius of Fe^{3+} (0.67\AA) in the B-site [72, 73, 82, 83], and diminution of total molecular weight in their stoichiometry. The slight increase in the X-ray density (ρ_x) may arise from the decrease in the volume of the unit cell (V_x). However, the average crystallite sizes (D_x) are found to increase with the *Mn* content (x) as shown in Table-4.10. This increasing trend may originate due to the increase in 2θ at constant *FWHM* that arising from the relatively smaller ionic size of dopant (Mn) [72]. The strain (ϵ) is also found to decrease with the increase of Mn content (x) and to maintain the usual inverse relationship with the crystallite size (D_x) [82]. This decrease in the strain, ϵ , may have originated from the stress relaxation because of the relatively smaller ionic sized dopant (Mn) [72, 82]. In the present work, the Rietveld refinement and Bertaut methods are used to determine the cation distribution. The best information on cation distribution is achieved by comparing the experimental and calculated intensity ratios for reflections whose intensities vary with the cation distribution in opposite ways, and do not significantly differ [72, 79, 113]. The final results of cation distribution, obtained from the analysis of X-ray diffraction after Rietveld refinement, are listed in Table 4.11.

Table-4.11: Cation distribution of $\text{CoMn}_x\text{Fe}_{2-x}\text{O}_4$ as determined from Rietveld refinement of XRD patterns

x	Concentration level, x	
	Tetrahedral(A) site	Octahedral(B) site
0.125	$\text{Co}_{0.1}\text{Mn}_{0.01}\text{Fe}_{0.89}$	$\text{Co}_{0.9}\text{Mn}_{0.115}\text{Fe}_{0.985}$
0.250	$\text{Co}_{0.1}\text{Mn}_{0.02}\text{Fe}_{0.88}$	$\text{Co}_{0.9}\text{Mn}_{0.235}\text{Fe}_{0.885}$
0.375	$\text{Co}_{0.1}\text{Mn}_{0.03}\text{Fe}_{0.87}$	$\text{Co}_{0.9}\text{Mn}_{0.345}\text{Fe}_{0.755}$
0.500	$\text{Co}_{0.1}\text{Mn}_{0.04}\text{Fe}_{0.86}$	$\text{Co}_{0.9}\text{Mn}_{0.46}\text{Fe}_{0.64}$

From the Table-4.11, it is seen that Fe^{3+} ions occupy both the A and B sites, a very small fraction of Co^{2+} ions occupy the A-site due to their bivalence. The Mn^{2+} ions are found to replace Fe^{3+} ions in both the A and B sites, which may be assumed due to the higher calcination temperature. Thus the cations are observed to deviate from their assumed ideal occupancy and are redistributed in both the sites. Fig.4.25 (b) shows the FESEM micrographs for the samples with different Mn content ($x = 0.125, 0.25, 0.375, 0.5$). The micrographs demonstrate randomly agglomerated

particles with nearly spherical shaped of average diameter around 22 nm, 27nm, 28 nm, and 32 nm respectively as determined by the line method using the Image-J software. The particle sizes of the samples are observed to follow the increasing trend of crystallite size due to a similar reason as explained in the literature [72, 114]. Besides pores are also noticed in their FESEM micrographs and assumed to have originated from the uneven sizes and lack in complete spherical shapes of particles [72, 80].

4.3.2 Magnetic Properties

To analyze the magnetic properties of the materials, the Waynekerr impedance analyzer (model 6500B) was used to measure the permeability using the toroid shaped samples of $\text{CoMn}_x\text{Fe}_{2-x}\text{O}_4$ at different concentration levels, $x \cdot 0.125 \leq x \leq 0.5$ under the variations of both frequency and temperature. The dc magnetization was measured using the vibrating sample magnetometer (VSM) both at room temperature (RT) and liquid nitrogen temperature (LNGT) by a thermocouple temperature controller. However, the significant experimental findings on the magnetic properties of the investigated samples are explained in this section for our purpose:

4.3.2.1 Frequency response of permeability

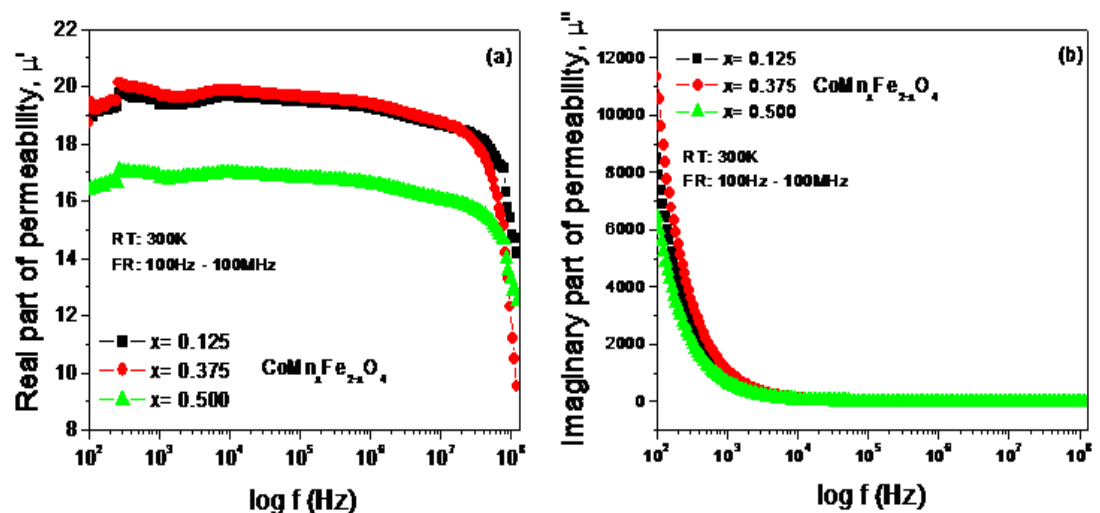


Fig. 4.26: (a) Real part (b) Imaginary part of ac permeability as a function of frequency for $\text{CoMn}_x\text{Fe}_{2-x}\text{O}_4$ sample with different Mn content (x) at room temperature in the frequency range 100 Hz–100 MHz

The real part μ' and imaginary part μ'' of ac permeability of the investigated samples with different Mn content ($x = 0.125, 0.375, 0.500$) are presented in Fig. 4.26 (a) and (b) as a function of frequency in the logarithmic scale. The real part, μ' of ac permeability is found to increase up to 265 Hz (snapshot) and a slight decrease over a wide band of frequencies up to around 30 MHz (snapshot) as seen from the Fig. 4.26 (a). The initial increase of μ' is expected to be caused by the combined effects of dipolar orientation (wall motion) and spin rotation [72]. The decrease in μ' is expected to originate from the fact that spin cannot follow the applied field at high frequency [72, 73, 85, 115]. However, the sudden fall of μ' at around 30 MHz exhibits anomalous behavior and is assumed to originate from the damping mechanism of spins under the influence of the applied ac magnetic field due to the dilution effect of Mn^{2+} on the B (octahedral) site [73, 85]. The imaginary part, μ'' of ac permeability is observed to decrease almost exponentially up to around 8 kHz (snapshot) and then to remain constant asymptotically over the whole measured frequency band as seen from Fig. 4.26 (b). The nature of the variation of μ'' demonstrates the normal behavior as reported in various works of literature. The variation of μ' with Mn content at any selected frequency below 25 MHz (snapshot) is found to be non-regular and unpredictable, but above 25 MHz, the same is noticed to be regular and predictable as seen from its dispersion as shown in Fig. 4.26 (a). The values of both μ' and μ'' are found to be large at $x = 0.375$ (Mn content) and least at $x = 0.5$ (Mn content) but for $x = 0.125$ (Mn content), it lies between them as seen from Fig. 5.2 (a) and (b), respectively. This situation in the values of both μ' and μ'' with Mn content may have originated from the heterogeneous particle size distribution due to calcination at elevated temperature. However, above 25 MHz, the value of μ' in its dispersion is found to maintain sequential variation with Mn content (x) where μ' decreases with the increase of Mn content (x) as seen from Fig. 5.2 (a), which is assumed to be caused by the dominance of the antiferromagnetic effect of Mn^{2+} ions in the B site [73, 73, 85].

4.3.2.2 Temperature response of permeability

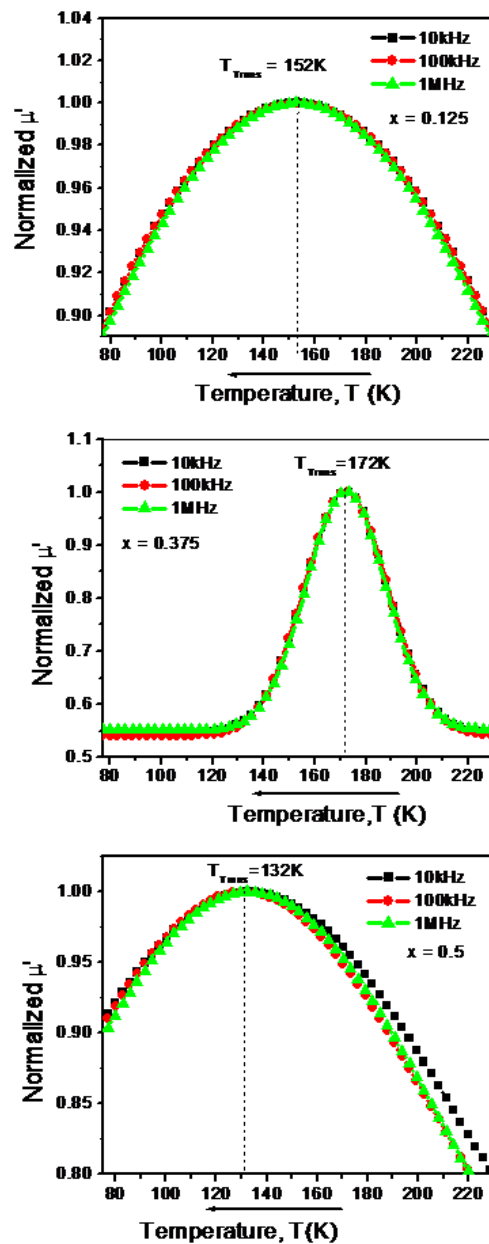


Fig.4.27: Normalized real part of permeability, μ' as a function of temperature for the samples of Mn content (x) = 0.125, 0.375, and 0.5 at different selected frequencies in the low-temperature regime

Fig.4.27 shows the variation of the real part, μ' of permeability as a function of temperature for the samples of $\text{CoMn}_x\text{Fe}_{2-x}\text{O}_4$ composition with Mn content (x) = 0.125, 0.375, 0.5 (as indicated in the figure) at selected frequency 10kHz, 100kHz and 1MHz in the low-temperature regime. As seen in the Fig.4.27, initially, the

normalized values of μ' increases with the drop in temperature up to a certain peak value of temperature and afterward, with a further drop in temperature μ' decreases. The increasing trend implies that the anisotropy energy becomes dominant over the thermal energy, which is the signature of ferrimagnetic-to-ferromagnetic phase transition. Conversely, the decreasing trend from the peak values (peak temperature points) with the further drops in temperature up to 77K may be thought of as a signature of transforming the ferromagnetic phase to the spin-glass state due to the frozen tendency of their spins in the lower temperature region [85, 100]. The peaks are observed at 152K, 172K, and 132K for the samples of $x = 0.125, 0.375,$ and 0.5 respectively at selected frequencies 10kHz, 100 kHz, and 1 MHz. The temperature corresponding to peaks may be assumed to be the transition temperature between ferromagnetic phase-to-spin glass state, T_{trans} . The transition temperature is found to vary with the Mn content (x) and almost independent of frequency [73, 85, 107]. No changes are observed in their imaginary part of permeability, μ'' (not shown).

4.3.2.3 Frequency response of complex magnetic modulus

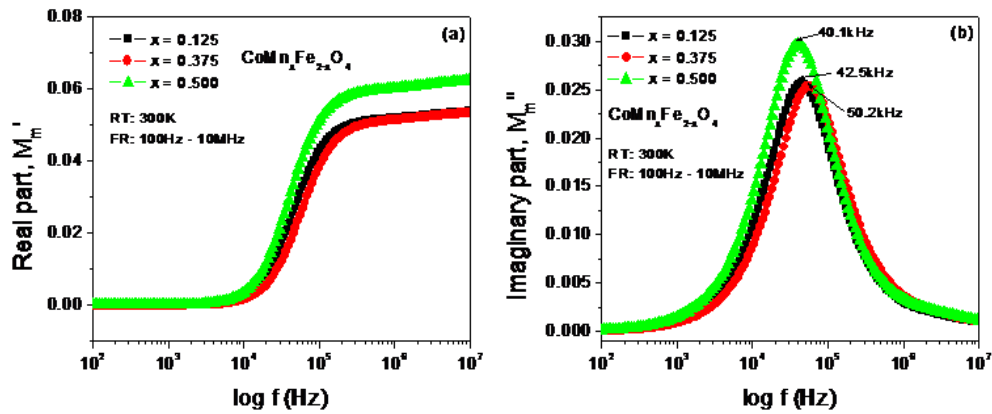


Fig.4.28: (a) M'_m vs $\log f$ curves (b) M''_m vs $\log f$ curves for the samples of $\text{CoMn}_x\text{Fe}_{2-x}\text{O}_4$ at room temperature (RT)

To understand the dynamics and effect of Mn content in the ac permeability of $\text{Co}_{1+x}\text{Mn}_x\text{Fe}_{2-x}\text{O}_4$, the magnetic modulus has been used to separate the local behavior of defects from any other effects (air gap, etc.). The magnetic modulus has been determined by the formula $M'_m(\omega) = \frac{\mu'(\omega)}{\mu'(\omega)^2 + \mu''(\omega)^2}$ and $M''_m(\omega) = \frac{\mu''(\omega)}{\mu'(\omega)^2 + \mu''(\omega)^2}$ [102, 104] from the measured values of μ' and μ'' . This formalism also

provides information about inductance and magnetic resistance. Fig.4.28 shows the dispersion of the real part M'_m , and, dispersion of the imaginary part M''_m of the complex magnetic modulus. As seen in Fig. 4.28(a), the real part of the magnetic modulus M'_m approaches to zero in the lower frequency-regime but it is found to increase almost exponentially with the increase in applied frequency to a single asymptotic value for each composition. The approaching to zero value of M'_m separates the local behavior of defects from any other external effects on the ac permeability. However, the increasing trend up to around 248 kHz may be due to the collective effects of wall motion and spin rotation. Afterward, almost constancy is observed over the frequency band 248 kHz – 10MHz, which can be attributed to the spin only rotations. As seen in Fig.4.28 (b), the well-resolved peaks are observed in the $M''_m(f)$ spectra and found to shift leftward with the Mn content but not in regular sequence. The frequency corresponding to the peak is known as resonance frequency, $f_{resonance}$ [72, 73] and is noticed maximum for Mn content (x) 0.375 and a minimum for 0.05. The calculated values of relaxation time constant as enumerated from the formula $\tau_m = 1/2\pi f_{resonance}$ are listed in table 4.12:

Table 4.12: Resonance frequency, $f_{resonance}$, and relaxation time constant (τ_m) and activation energy for x=0.125 of $\text{CoMn}_x\text{Fe}_{2-x}\text{O}_4$

Parameters	Concentration level,x		
	x = 0.125	x = 0.375	x = 0.5
Resonance frequency, $f_{resonance}$	42.5 kHz	50.2 kHz	40.1 kHz
Critical relaxation time constant, τ_m	3.74 μs	3.17 μs	4.18 μs

4.3.2.4 Magnetization at RT

The magnetic hysteresis (M - H) loops are recorded at room temperature (RT) for the samples of $\text{CoMn}_x\text{Fe}_{2-x}\text{O}_4$ composition with Mn content ($0 \leq x \leq 0.5$) and presented in Fig. 4.29 (a). The M-H curves exhibit almost line hysteresis and are found to be similar nature for each system at room temperature (RT). The saturation magnetization (M_s) is defined here as the magnetization at the field of 8 kOe for the explanation of the variation of magnetization with the Mn content. This saturation magnetization (M_s), remnant magnetization (M_R), and coercivity (H_C) have been determined from the hysteresis curves at RT [85, 117, 118]. The initial permeability (μ_i) has also been determined from the respective slope of the initial M – H (1st

quadrant) curves as shown in Fig.4.29 (b) for the investigated samples of $\text{CoMn}_x\text{Fe}_{2-x}\text{O}_4$. All these magnetic parameters are listed in Table 5.4. From this, it is seen that the saturation magnetization, M_s , and initial permeability, μ_i decreases with the Mn content, which may have come out from the antiferromagnetic effect of Mn^{2+} in the B site according to Neel's two-sublattice model.

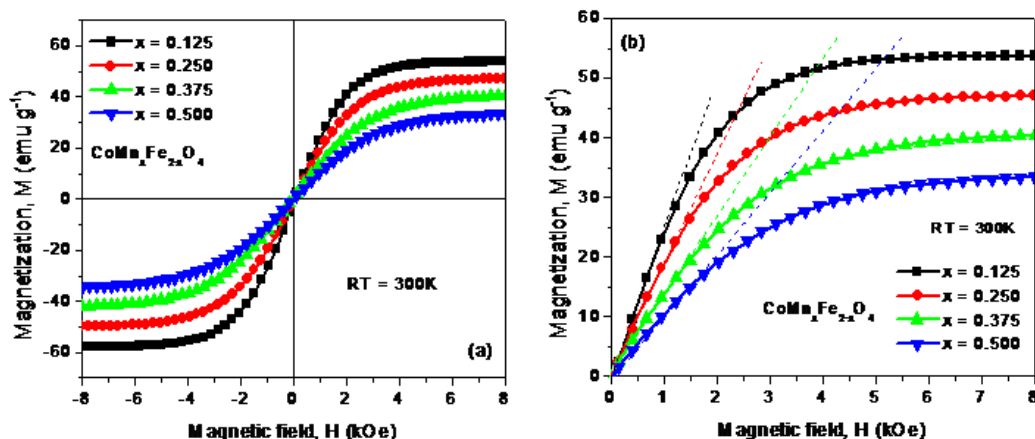


Fig.4.29: (a) Hysteresis Curves (b) Initial M-H Curves for the sample of $\text{CoMn}_x\text{Fe}_{2-x}\text{O}_4$ with Mn content ($0 \leq x \leq 0.5$) at RT

Table 4.13: The magnetic parameters of $\text{CoMn}_x\text{Fe}_{2-x}\text{O}_4$ (CFM) ferrite system at RT

x	M_s (emu g^{-1})	M_R (emu g^{-1})	M_R/M_s	H_c (Oe)	μ_i ($\text{emu g}^{-1}\text{kOe}^{-1}$)
0.125	53.92	0.517	0.0096	6.683	26.11
0.250	47.16	0.465	0.0098	8.785	16.47
0.375	40.49	0.495	0.0122	10.57	13.49
0.500	33.82	0.608	0.0208	11.14	9.53

However, the remnant magnetization ratio (M_R/M_s) and coercivity (H_c) are found to increase with the Mn content, which demonstrates the normal magnetic behavior due to the substitution of Mn^{2+} in place of Fe^{3+} ions in the B-site that causes a fall in the saturation magnetization. The remnant ratio (M_R/M_s) is found from Table 4.13 to be 0.0096 for the representative sample of the CFM system with Mn content ($x = 0.125$), which marks its superparamagnetic behavior [72, 119] and maybe suitable to be used in spintronics applications.

4.3.3 Electric Properties

To analyze the electric properties of the materials, the Waynekerr impedance analyzer (model 6500B) was used to measure/determine the dielectric constant and resistivity using the disc-shaped samples at different Mn content (x), $0.125 \leq x \leq 0.5$ under the variations of both frequency and temperature. Their dc resistivity was also measured by the conventional 4-probe technique as a function of temperature and magnetic field. However, the significant findings on the analysis of the electrical properties of the materials are elaborately explained in this section for our purpose:

4.3.3.1 Dielectric constant

4.3.3.1.1 Frequency response of dielectric constant

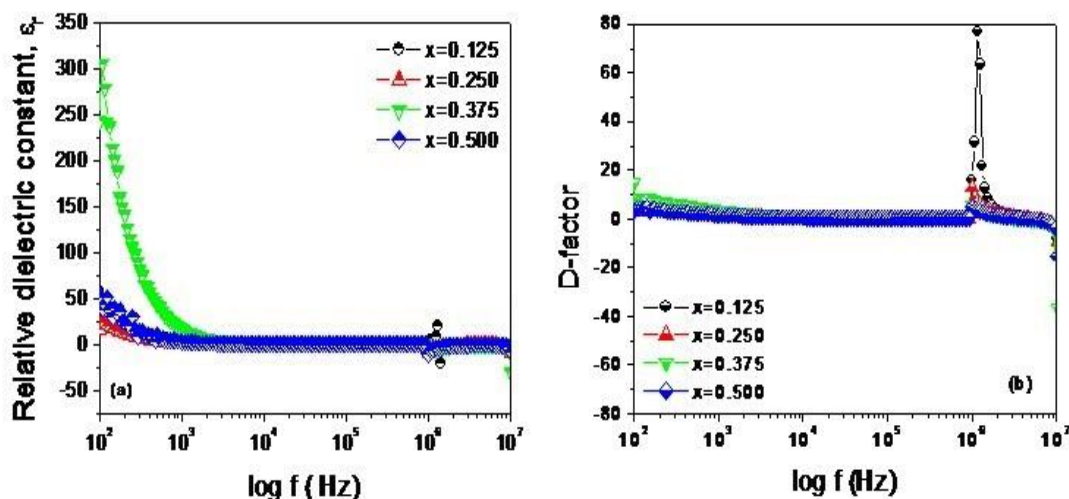


Fig. 4.30: (a) Relative dielectric constant, ϵ_r (b) D-factor as a function of frequency for the sample of $\text{CoMn}_x\text{Fe}_{2-x}\text{O}_4$ at room temperature in the frequency range 100 Hz–10 MHz.

Fig.4.30 (a) and (b) show the variation of the relative dielectric constant, ϵ_r and dissipation factor (D-factor) of the investigated samples with different Mn content ($x = 0.125, 0.25, 0.375$ and 0.5) as a function of frequency on a logarithmic scale at room temperature (RT), respectively. The frequency response of the relative dielectric constant, ϵ_r and D-factor demonstrate normal behavior up to around 2 kHz and after onwards anomalous behavior as seen from their corresponding graph of Fig. 4.30(a) and 4.30(b). The normal behavior implies the decrease of ϵ_r with the increase

in frequency, which may have originated from the lagging of hopping frequency of charge carriers behind the applied frequency according to Maxwell–Wagner interfacial polarization model and its constancy up to 1 MHz from the electronic contribution of polarizability because beyond a certain frequency of externally applied field the electron exchange between F^{3+} and Fe^{2+} cannot follow an alternating field [72, 85, 120]. The peaks of D-factor as observed at 1 MHz as seen from Fig. 4.30(b) may have arisen from the resonance effect due to the faster electron hopping between ferric and ferrous ions in the B-site [72, 80, 85, 97]. The variation in the value of ϵ_r with the Mn content is observed below 1 kHz and afterward, to remain asymptotic constant. The value of ϵ_r is found to be large for Mn content ($x = 0.375$) and least for Mn content ($x = 0.25$). The values of ϵ_r for the other two concentrations of Mn content ($x = 0.125$ and 0.5) are between them. This variation in the value of ϵ_r is assumed to cause from the inhomogeneity of charge carriers (p-type and n-type) across the grain boundaries [72].

4.3.3.1.2 Temperature response of dielectric constant

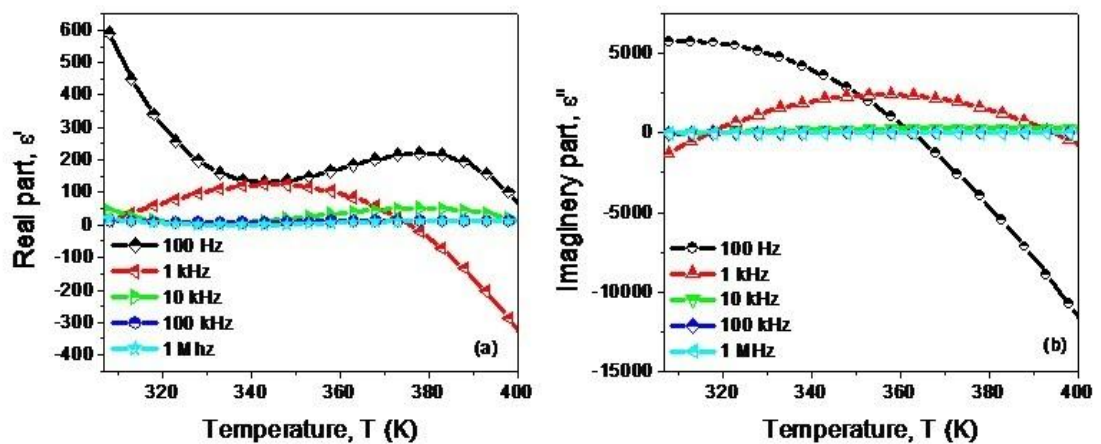


Fig. 4.31: Graphs for (a) Real part, ϵ' and (b) Imaginary part, ϵ'' of dielectric constant as a function of the temperature for the sample of $CoMn_xFe_{2-x}O_4$ at Mn content, $x = 0.125$

Fig. 4.31 shows the variation of dielectric constant as a function of temperature (320K – 390K) for the samples at Mn content, $x=0.125$ for selective frequencies as 100Hz, 1kHz, 10kHz, 100kHz, and 1MHz. The temperature dependence of dielectric constant at 100 kHz and 1 MHz is found to be independent of temperature. However, the variation in dielectric constant with the temperature at

100 Hz is found to be dissimilar to that of previously reported results of indium substituted cobalt ferrite [91]. As seen in Fig.4.31 (a), the decreasing trend of dielectric constant at 100 Hz may be a result of the transformation of interfacial polarization to ionic polarization due to the hopping of charges between Co^{2+} and Fe^{2+} ions in the B site at the lower temperature. At higher temperatures, the increase in dielectric constant is expected to be originated from the enhanced hopping rate resulted from the boosted mobility of charge carriers by the extra thermal energy from the higher temperature as explained in the case of indium substituted cobalt ferrite as reported in the literature [54,82, 72, 80, 85]. But the variation of dielectric constant at 1 kHz is found to exhibit anomalous behavior. From Fig.4.31 (b), it is observed that the nature of variation of ϵ'' is almost similar to that of ϵ' up to 90°C at 100 Hz, but its negative region implies the change of polarization direction due to increase of $\text{Co}^{2+}/\text{Fe}^{2+}$ ratio for the substitution of Mn^{2+} in the B site. The increase in dielectric constant at 10 kHz and 1 MHz as seen in Fig.4.31(a) and (b) is expected to cause from the only presence of electronic polarization, which is independent of temperature. The relaxation time (τ) was calculated from the peaks of ϵ' of dielectric constant from ϵ' vs T curves as shown in Fig.4.31(a) using the values of ϵ'' of dielectric constant at corresponding temperature from ϵ'' vs T curves as shown in Fig.4.31 (b) at selected frequencies by the equation $\omega\epsilon'' = \epsilon'(\omega)$, modified from the Debye formula [80, 85, 103] since $\epsilon'_\infty \sim 0$ and listed in Table-5.5.

Table 4.14: Relaxation time constant (τ) for the sample of $\text{CoMn}_x\text{Fe}_{2-x}\text{O}_4$ with $\text{Mn}(x) = 0.125$ at RT

Frequency	100 Hz	1kHz	10kHz	100 kHz	1 MHz
Relaxation time constant, τ	123.57 μs	8.52 μs	2.01 μs	0.08 μs	0.01 μs

It is seen from Table-4.14 that for this system the relaxation time (τ) decreases with the increase of frequency, which is normal and further confirmation of the dielectric behavior of the system.[78, 80, 82].

4.3.3.2 AC Resistivity

4.3.3.2.1 Frequency response of ac resistivity and ac conductivity

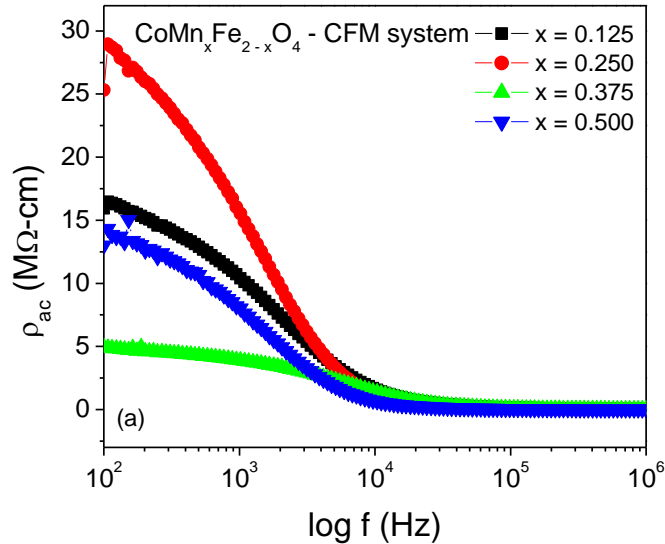


Fig. 4.32: Ac resistivity, ρ_{ac} as a function of frequency for the sample of $\text{CoMn}_x\text{Fe}_{2-x}\text{O}_4$ at room temperature in the frequency range 100Hz–1MHz

Fig.4.32 shows the variation of ac resistivity, ρ_{ac} as a function of frequency in a logarithmic scale of the investigated samples with different Mn content ($x=0.125, 0.25, 0.375, 0.5$) respectively. From Fig. 4.32, the ac resistivity, ρ_{ac} is found to decrease almost exponentially with the increase of frequency of the applied field. This decreasing behavior of ρ_{ac} is expected to cause by the increasing effect of multilayer capacitor with the increase of frequency according to Koop's phenomenological theory [72,84], which suggested that the ferrite compact acts as multilayer capacitors and also the grain and grain boundaries have accounted for possessing different properties. The irregular and unpredictable change in resistivity, ρ_{ac} is found with the Mn content (x) up to around 10kHz, which may be attributed to the cation redistribution arising from the replacement of Fe^{2+} by Mn^{2+} in the B site, and afterward, it becomes independent of both the frequency and Mn concentration. In the low-frequency region i.e. below 10kHz, the grain boundary is more responsive to contribute resistivity due to Maxwell-Wagner interfacial polarization because the hopping frequency of charge carriers can follow the applied field frequency in the grain boundaries. However, at higher frequencies i.e. above 10kHz, the hopping

frequency of charge carriers lag behind the applied field frequency in the grain boundaries due to random dipolar orientations [72, 73] and thus make the grain boundaries non-responsive.

4.3.3.2.2 Temperature response of ac resistivity and ac conductivity

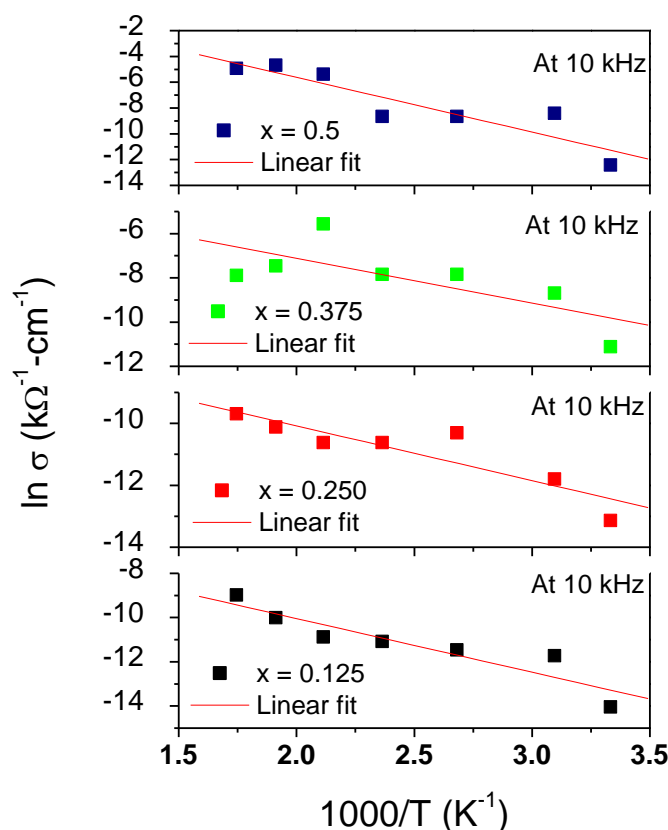


Fig.4.33: AC Conductivity, σ_{ac} as a function of inverse temperature ($1000/T$) for the sample of composition $\text{CoMn}_x\text{Fe}_{2-x}\text{O}_4$ at selected frequency of 10kHz over the temperature range (300–573)K

Fig.4.33 shows the variation ac conductive, σ_{ac} with the temperature at a selected frequency of 10kHz. In that Fig. 5.9 presents the curve for $\ln\sigma_{ac}$ vs $1000/T$ respectively. From Fig. 4.33, the ac conductivity σ_{ac} to increase with the increase in temperature (T). The increasing trend of σ_{ac} with the temperature demonstrate their semiconducting behavior of materials. The increase of σ_{ac} with the increase of temperature may be attributed to the enhanced ionic hopping due to the increased mobility of charge carriers across the grain boundaries in the B-site [1, 72, 121]. Since the frequency is kept constant at 10kHz, so the fitted trend lines to ac

conductivity curves may be thought to follow the usual Arrhenius relation $\sigma_{ac} = \sigma_0 e^{-E_a/kT}$ for conductivity. The activation energy, E_a for different Mn content (x) has been estimated in the ferromagnetic region from the slope of the trend lines of conductivity using its Arrhenius relation considering pre-factor as unity i.e. $\sigma_0 = 1$. The estimated activation energy, E_a has been listed in the following Table 4.15 to analyze the effect of Mn content (x) on the magnetic properties of the investigated samples at a particular selected frequency (10 kHz). The value of E_a in the ferromagnetic regime is lower than the paramagnetic regime due to magnetic spin ordering [72, 99]. From Table 4.15, it is found that the variation of activation energy, E_a follows the increasing trend with Mn content (x). This increasing trend in the activation energy, E_a implies a spin disorder phenomena leading to a possible ferrimagnetic-to-paramagnetic phase transition. Thus it is possible to tune the material to behave as a soft magnetic material above the room temperature. This behavior is expected due to the antiferromagnetic effect of Mn^{2+} in the B site [72, 80].

Table-4.15: Values of E_a at 10 kHz for the investigated samples of $CoFe_{2-x}O_4$ composition

Mn Content (x)	0.125wt%	0.250wt%	0.375wt%	0.500wt%
Activation Energy, E_a	0.11eV	0.15eV	0.17eV	0.37eV

4.3.3.3 Complex electrical modulus

Complex electric modulus analysis is usually used to determine and interpret the dynamical transport phenomenon (i.e. parameters such as carrier/ion hopping rate, conductivity, relaxation time, etc.). This electric modulus approach gives insight into the bulk response which can separate the local behavior of defects from the electrode effect. From the physical point of view, the electric modulus corresponds to the relaxation of the electric field in the material when the electric displacement remains constant. Therefore, it represents the real dielectric relaxation process [72, 122]. For the purpose, both the real and imaginary parts of complex electric modulus have determined from the measured real and imaginary parts of complex dielectric

constant using the usual formalism as $M'(\omega) = \frac{\varepsilon'(\omega)}{\varepsilon'(\omega)^2 + \varepsilon''(\omega)^2}$ and $M''(\omega) = \frac{\varepsilon''(\omega)}{\varepsilon'(\omega)^2 + \varepsilon''(\omega)^2}$. [102, 149]

4.3.3.3.1 Frequency response of electric modulus at RT

Fig. 4.34 (a) presents the variation of the real part of electric modulus (M') with the frequency in a logarithmic scale at room temperature (RT). From this Fig. 4.34 (a), it is observed that the values of M' for all the investigated samples approach to almost zero in the low-frequency regime. This fact marks the negligible contribution of electrode polarization in the materials [72, 123]. A continuous increase in M' with the increase of frequency is observed. The magnitudes in M' tend to saturate to an asymptotic single value that may have originated from the short-range mobility of charge carriers (p-type and n-type) [72, 85, 122, 124] due to shorted hopping length (L_B) in the B site. However, the maximum asymptotic value of M' at 1MHz is found to decrease with the Mn content, which may be due to the increased crystallite size (D). Fig.4.34 (b) shows the variation of M'' with the increase of frequency on a logarithmic scale at RT. The well-resolved peaks are found to appear at the characteristic frequency (f_{max}) in their $M''(f)$ spectra. These peak positions are found to depend on the Mn content but not sequentially and predictably, which are also evident from the Nyquist plot (M' vs. M'') as shown in Fig. 4.34 (c). The characteristic frequency (f_{max}) determined from the corresponding peak, and the relaxation time (τ) estimated from the equation ($\tau = 1/2\pi f_{max}$) [72, 82, 85, 124] are presented in Table-4.16. Two semicircles (semicircle-I and II) of non-ideal shape are found to occur in the Nyquist plot of electric modulus as shown in Fig. 4.34 (c) that separates the grain boundary and grain contributions to the electrical conductivity of the material. In the low-frequency range, the higher values of M'' indicates lower conductivity that signifies higher dielectric constant arising from the Maxwell-Wagner interfacial polarization in the grain boundaries. This polarization is expected to have originated from the hopping of electrons between Fe^{2+} and Fe^{3+} ions in the direction of the applied electric field, and between Co^{3+} and Co^{2+} ions in the opposite direction across the grain boundaries [72,80, 82, 125]. The semicircle-I corresponds to this grain boundary contribution to their material conductivity. Conversely, the lower values of M'' indicates higher conductivity in the

high-frequency regime due to increased hopping of localized carriers in the grain for the shorted-hopping length (L_B) in the B site. The semicircle-II corresponds to their grain contribution in material conductivity. As the Nyquist plot separates the components with different resistances and capacitances, so the equivalent circuit may be thought of as two RC parallel circuits corresponding to two semicircles for each sample with different values of capacitance and resistance as shown in Fig.4.34(d). The capacitances and resistances corresponding to the grain and grain boundaries have been estimated using the values of M' at respective peaks of the Nyquist plot from the equation $M' = \frac{C_0}{C}$ and $\tau = RC$ respectively [72, 85] and listed in Table 4.16.

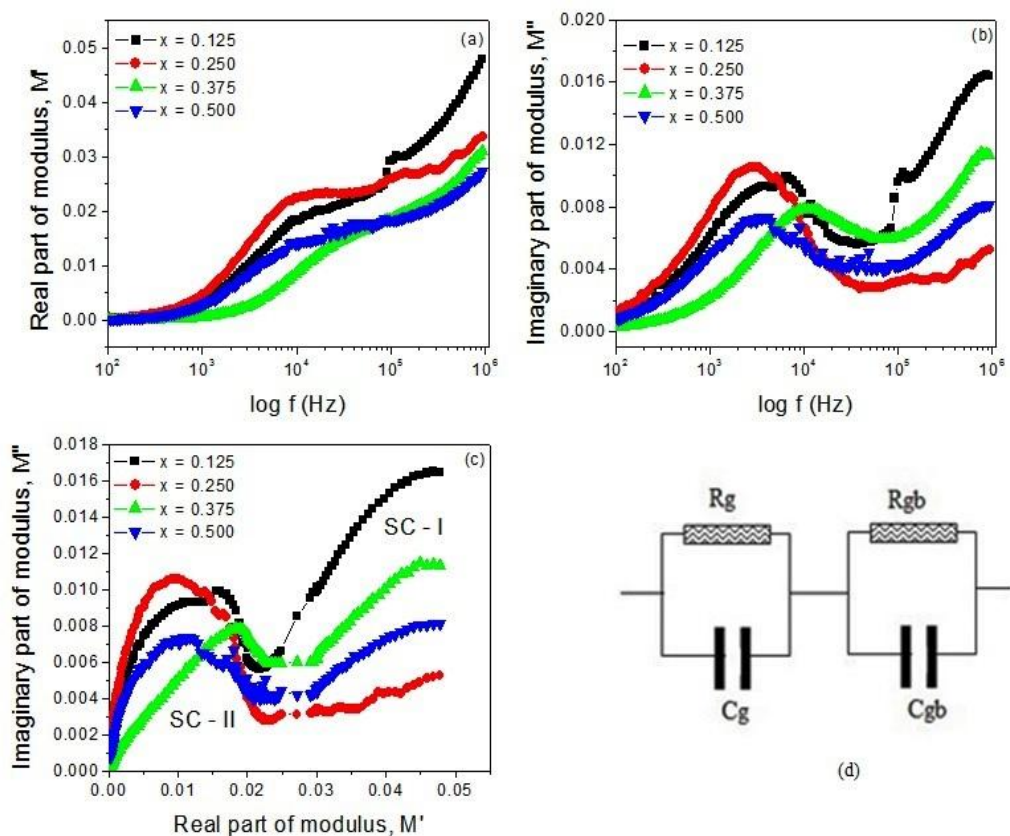


Fig. 4.34: (a) Real part, M' , (b) Imaginary part, M'' of electric modulus as a function of frequency, (c) Nyquist plot (M'' vs. M') for CFM system at RT in the frequency range 100Hz–1MHz, (d) Equivalent circuit

Table 4.16: Characteristic frequency (f_{max}), relaxation time (τ), grain-boundary capacitance (C_{gb}), grain capacitance (C_g), grain-boundary resistance (R_{gb}) and grain resistance (R_g) for the investigated samples

Parameters	x=0.125	x=0.250	x=0.375	x=0.500
f_{max} , determined from peaks	5817.56 Hz	2667.8Hz	10021.6Hz	4213.4 Hz
τ estimated by $\tau = 1/2\pi f_{max}$	0.273 μ s	0.596 μ s	0.129 μ s	0.378 μ s
$C_{gb}(Sc-I)$ (Grain boundary capacitance)	0.190nF	0.186 nF	0.197 nF	0.185 nF
$C_g(SC-II)$ (Grain capacitance)	0.573 nF	0.962 nF	0.473 nF	0.831nF
$R_{gb}(SC-I)$ (Grain boundary resistance)	0.144M Ω	0.320 M Ω	0.065 M Ω	0.204 M Ω
$R_g(SC-II)$ (Grain resistance)	0.047 M Ω	0.062 M Ω	0.027 M Ω	0.045 M Ω

4.3.3.3.2 Temperature response of electric modulus

Fig.4.35 shows the variation of the normalized value of both the real part and imaginary part of the electric modulus with the frequency of the representative samples of the $CoMn_xFe_{2-x}O_4$ composition with Mn(x) content=0.125 for different temperatures 423K, 473K, and 523K. From Fig.4.35(a), it is seen that the normalized value of M' (as scaled M'/M'_{max}) approaches to zero in the low-frequency range at all selected temperature indicating a negligible contribution of electrode polarization in the materials. However, the continuous increase of M' with the frequency can be attributed to the conduction process due to the short-range hopping of charge carriers. It can also be related to the absence of the restorative force which governs the mobility of charge carriers under the action of the induced electric field [72, 126]. Conversely, the value of M' is found to decrease with the increase in temperature. This decrease in M' signifies the increase of conductivity resulting from the faster hopping of both the charge carriers (p-type and n-type) due to thermal agitations as electric modulus formalism represents the real dielectric relaxation [72, 80, 85, 106], which is also evident from the Fig. 4.35 (b) for x=0.125 at RT. Fig. 4.35 (b) shows an asymmetric peak of the normalized value of M'' (as scaled M''/M''_{max}) at each temperature. The low-frequency wing represents the frequency band in which the

charge carriers can move over long distances whereas in the high-frequency wing the charge carriers are spatially confined to the potential well and can make an only localized motion in the well. The peaks of M''/M''_{\max} indicate the transition from long-range to short-range mobility of charge carriers at different temperatures [102, 113, 126]. This peak position is found to shift leftward with the temperature in the lower frequency regime, which corresponds to longer relaxation time and may result from the rotational dielectric relaxation by ionic hopping in the B site [102, 127, 128, 129].

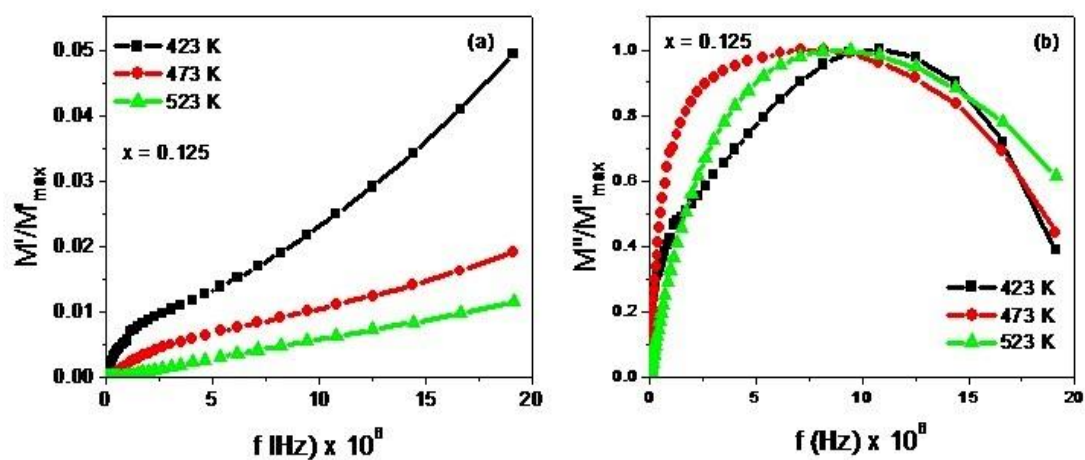


Fig.4.35:(a)Normalized real part of electric modulus, M' (b) Normalized imaginary part of electric modulus, M'' as a function of frequency (100Hz–20MHz) at selected temperature 423K, 473K, and 523K for representative sample of CM system with Mn (x)=0.125

4.4 Stoichiometric composition $Co_{1-x}Mn_xFe_2O_4$

In this composition, x refers to the Mn content that replaces Co at the wt% 0.125, 0.25, 0.375, 0.5 that make this composition stoichiometric.

4.4.1 Crystallographic and Morphological Analysis

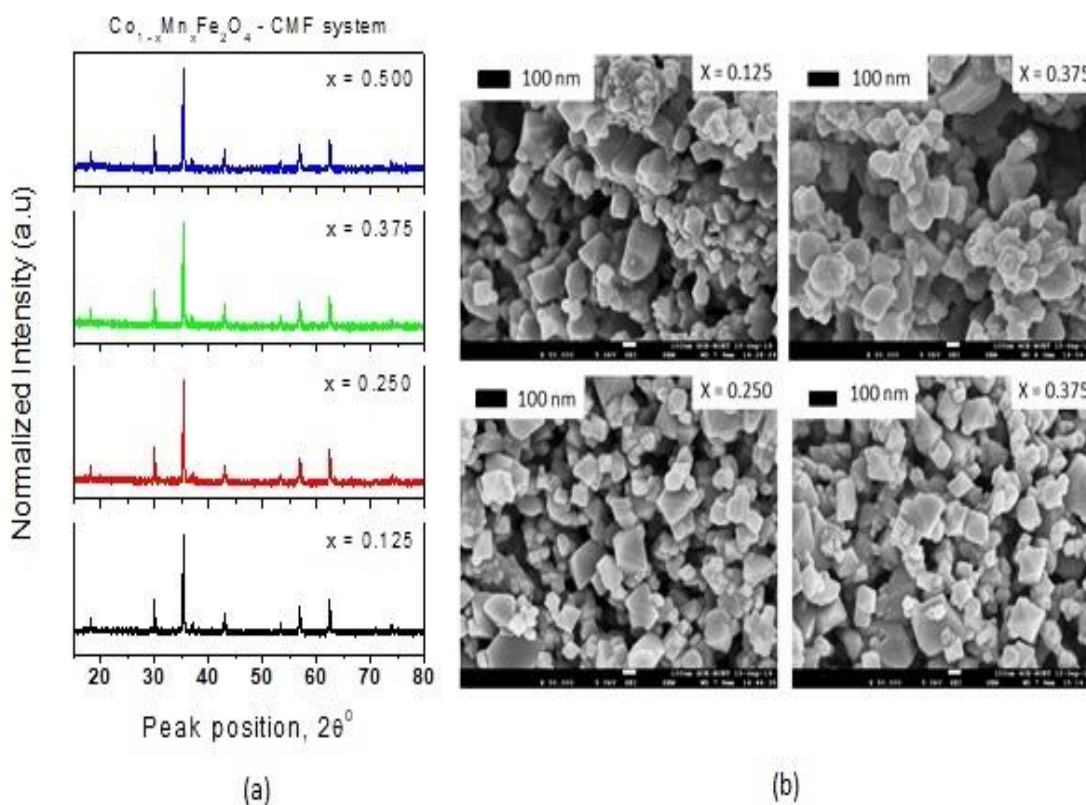


Fig.4.36: (a) X-ray diffraction patterns (b) FE-SEM Micrographs for samples of the CMF system with Mn content (x) = 0.125, 0.25, 0.375 and 0.5

Fig.4.36 (a) shows the X-ray diffraction (XRD) patterns of the $Co_{1-x}Mn_xFe_2O_4$ (CMF) for different Mn content (x) = 0.125, 0.25, 0.375, 0.5. The observed peaks in the patterns are found to well match with the standards JCPDS card No. 22-1086 for $CoFe_2O_4$ and the planes of Mn substituted cobalt ferrite nanoparticles corresponding to Miller indices (111), (220), (311), (400), (422), (511) and (440) [72, 73, 130]. These planes indicate that the samples exhibit the single-phase cubic spinel structure without any impurity phase corresponding to any other structure. The intense sharp peaks confirm their crystallinity. The X'pertpro High Score Plus software was used to determine the peak position (2θ) and full width at

half maximum (FWHM) of the strongest peak corresponding to the Miller plane (311). This Miller plane (311) has been used to estimate the lattice constant (a), cell volume (V), the crystallite size (D_x), X-ray density (ρ_x), and strain (ϵ) by using the usual formulas. Stanley's equations were also used to estimate hopping lengths and bond lengths [6, 82]. All these structural parameters are listed in the following Table-4.17 for crystallographic analysis:

Table-4.17: Different structural parameters of $\text{Co}_{1-x}\text{Mn}_x\text{Fe}_2\text{O}_4$ as determined from the XRD patterns

Structural parameters	Concentration level, x			
	$x = 0.125$	$x = 0.25$	$x = 0.375$	$x = 0.5$
2θ of (311) plane	35.515	35.521	35.525	35.531
FWHM	0.1304	0.1248	0.1245	0.1243
$a(\text{\AA})$	8.383	8.382	8.381	8.380
$V_x(\text{\AA})^3$	589.24	588.96	588.76	588.47
D_x (nm)	64.02	66.90	67.10	67.17
ρ_x (gm cm^{-3})	5.104	5.107	5.109	5.111
$L_A(\text{\AA})$	3.630	3.629	3.627	3.623
$L_B(\text{\AA})$	2.964	2.963	2.962	2.960
A-O(\AA)	1.817	1.815	1.813	1.811
B-O(\AA)	2.097	2.095	2.092	2.089
Microstrain ϵ	0.00181	0.00170	0.00169	0.00168

From Table-4.17, the lattice constant (a) and other associated parameters such as unit cell volume (V_x), tetrahedral hopping length (L_A), octahedral hopping length (L_B), tetrahedral bond length (A-O), and octahedral bond length (B-O) are observed to slight decrease with the Mn content (x). The decrease in lattice constant, a , may be attributed to the effect of the relatively smaller ionic radius of Mn^{2+} (66\AA) [72] that replaces a larger ionic radius of Co^{2+} (0.78\AA) in the B-site [78]. The slight increase in the X-ray density (ρ_x) may arise from the decrease in the volume of the unit cell (V_x) [82]. However, the crystallite sizes (D_x) are found to increase with the Mn content (x) that may be due to the combined effects of the increase in 2θ and decrease in $FWHM$, arising from the relatively smaller ionic size of dopant (Mn). The strain (ϵ) is also

found to decrease with the increase of Mn content (x) and to maintain the usual inverse relationship with the crystallite size (D_x). This decrease in the strain, ϵ , may have originated from the stress relaxation because of the relatively smaller ionic sized dopant (Mn) [78, 82]. In the present work, the Rietveld refinement and Bertaut methods are used to determine the cation distribution. The best information on cation distribution is achieved by comparing the experimental and calculated intensity ratios for reflections whose intensities vary with the cation distribution in opposite ways, and do not significantly differ [72, 79, 131]. The final results of the cation distribution are listed in Table 4.18.

Table-4.18: Cation distribution of $\text{Co}_{1-x}\text{Mn}_x\text{Fe}_2\text{O}_4$ (CFM) system as determined from Rietveld refinement of XRD patterns

x	Cation Distribution	
	A site	B site
0.125	$\text{Co}_{0.01}\text{Mn}_{0.03}\text{Fe}_{0.96}$	$\text{Co}_{0.99}\text{Mn}_{0.095}\text{Fe}_{1.04}$
0.25	$\text{Co}_{0.025}\text{Mn}_{0.04}\text{Fe}_{0.94}$	$\text{Co}_{0.975}\text{Mn}_{0.214}\text{Fe}_{1.06}$
0.375	$\text{Co}_{0.048}\text{Mn}_{0.087}\text{Fe}_{0.9}$	$\text{Co}_{0.952}\text{Mn}_{0.288}\text{Fe}_{1.1}$
0.5	$\text{Co}_{0.07}\text{Mn}_{0.13}\text{Fe}_{0.86}$	$\text{Co}_{0.93}\text{Mn}_{0.37}\text{Fe}_{1.14}$

From Table-4.18, it is seen that Fe^{3+} ions occupy both the A and B sites, a very small fraction of Co^{2+} ions occupy the A-site due to their bivalence. The Mn^{2+} ions are found to replace Co^{2+} ions in both the A and B sites, which may be assumed due to the higher calcination temperature. Thus the cations are observed to deviate from their assumed ideal occupancy and are redistributed in both the sites. Fig.4.36 (b) shows the FE-SEM micrographs for the samples of different Mn content ($x = 0.125, 0.25, 0.375, 0.5$). The micrographs demonstrate randomly agglomerated particles with nearly spherical shaped of average particle size around 32 nm, 30nm, 28 nm, and 24 nm respectively as determined by the line method using the Image-J software. The average particle sizes are found to follow the decreasing trend of lattice constant due to the relatively smaller ionic size of Mn^{2+} . Besides pores are also observed in their FE-SEM micrographs and assumed to have originated from the uneven sizes and non-spherical shapes of particles due to their agglomeration [72, 73, 80, 82].

4.4.2 Magnetic Properties

To analyze the magnetic properties of the materials, the Waynekerr impedance analyzer 6500 B series was used to measure the permeability using the toroid shaped samples of $\text{Co}_{1-x}\text{Mn}_x\text{Fe}_2\text{O}_4$ at different concentration levels, $0.125 \leq x \leq 0.5$ under the variations of both frequency and temperature. The dc magnetization was measured using the vibrating sample magnetometer (VSM) both at room temperature (RT) and liquid nitrogen temperature (LN₂) by a thermocouple temperature controller. However, the significant experimental findings on the magnetic properties of the investigated samples are elaborately explained in this section for our purpose.

4.4.2.1 AC Permeability

The ability to create a magnetic field within itself of a material is generally known as permeability. The dynamic response of permeability by the alternating magnetic field gives rise to the complex permeability and described by the relation $\mu = \mu' - j\mu''$, where μ' represents the real part and μ'' imaginary part [102, 104, 109]. The phase between the response of magnetic domains and applied field determines this real part and this imaginary part of the complex permeability. The function frequency ascertains the dynamic condition of the magnetic domains. At low frequency, the initial permeability creates a lot of information about the domain wall motion. Therefore, the complex permeability as a function of frequency for different composition is very important for understanding the mechanism of dynamic properties of these materials and to ascertain their effectiveness in the field of high-frequency applications. Fig.4.37(a) shows the dispersion of μ' for the investigated samples (toroid shaped) of $\text{Co}_{1-x}\text{Mn}_x\text{Fe}_2\text{O}_4$ at room temperature (RT). The initial rise in μ' with the applied frequency up to around 550Hz may cause from the collective effect of the domain wall motions and spin rotations. A very slight linear decrease in μ' with the applied frequency seems to be almost constant over the band 550Hz–1MHz. This behavior of μ' maybe attributed to the damping mechanism of spin only rotations due to nanosized particles [9, 73, 85]. Over the whole frequency band (100Hz – 1MHz) the magnitude of μ' decreases with the increase in Mn content (x) due to the antiferromagnetic effect of Mn^{2+} in the B site. Fig.4.37 (b) shows the

dispersion of μ'' for the same samples. An almost exponential decrease in μ'' up to around 1.5 kHz is observed in its dispersion that may be due to the damping mechanism of dipolar orientations. Afterward, μ'' becomes non-responsive to the applied frequency over the band 1.5 kHz – 1MHz and is expected to cause from the spin only rotations due to their nanosized particles [73, 82, 123]. This non-responsive or independence behavior of μ'' in the frequency range may make this material a suitable candidate to be used in the high-frequency applications.

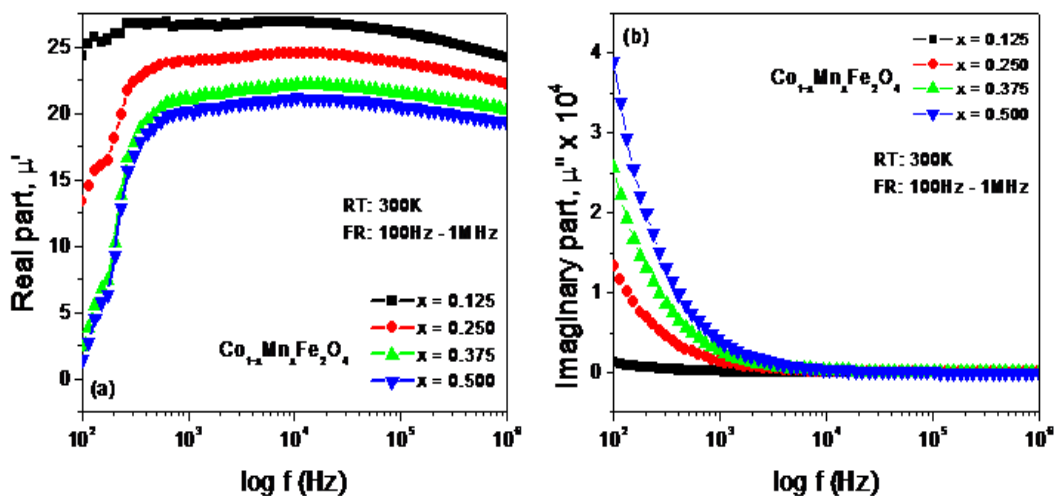


Fig.4.37: (a) Real part, μ' (b) Imaginary part, μ'' for the sample of $\text{Co}_{1-x}\text{Mn}_x\text{Fe}_2\text{O}_4$ at different Mn(x) in the frequency range 100Hz – 1MHz

4.4.2.2 Magnetic modulus

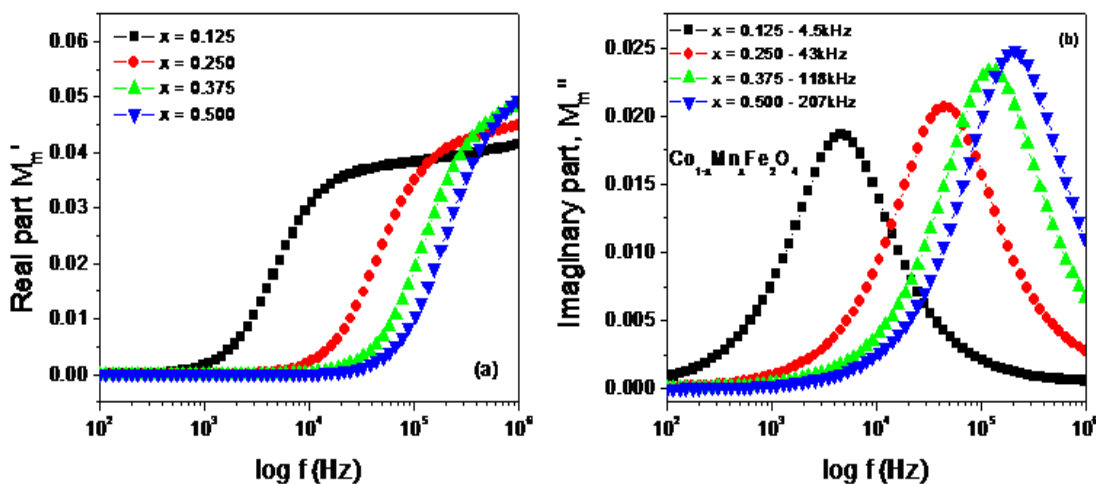


Fig.4.38: (a) M_m' vs $\log f$ curves (c) M_m'' vs $\log f$ curves at room temperature for the samples of $\text{Co}_{1-x}\text{Mn}_x\text{Fe}_2\text{O}_4$

The complex permeability, in particular, the value of μ' , depends on stoichiometry, average grain size, composition, impurity, coercivity, and porosity, etc. Hence, to understand and analyze the effect of Mn content in the complex permeability of $\text{Co}_{1-x}\text{Mn}_x\text{Fe}_2\text{O}_4$, the magnetic modulus has been used to separate the local behavior of defects from any other effects (air gap, etc.). The magnetic modulus has been determined by the usual formula from the measured values of μ' and μ'' [73]. This formalism also provides information about inductance and magnetic resistance. Fig.4.38 shows the dispersion of the real part M'_m and the imaginary part M''_m of the magnetic modules. As seen in Fig. 4.38 (a), a non-linear increase in M'_m is observed with the increase of the applied frequency that signifies the contributions of both the wall motion (wall relaxation) and the spin rotations (rotational resonance) in the magnetization [73, 85]. Afterward, M'_m is found to a slight linear increase to a single asymptotic value, which implies the ceasing of wall motions but the only presence of spin rotations. Both the increasing and decreasing trend up to and from well-resolved peaks is observed with the increase of frequency in the dispersion of M''_m as shown in Fig.4.38 (b). The frequency corresponds to the peak is known as the resonance frequency $f_{resonance}$ and follows the increasing trend in the crystallite/grain size as revealed from Table-4.17. Besides, the magnitude of M''_m at the corresponding resonance frequency is also marked to increase with the increase in Mn content. This fact implies the more absorption of magnetic energy from the magnetic field that in turn leading to decrease spin rotations. The calculated values of relaxation time constant as enumerated from the formula $\tau_m = 1/2\pi f_{resonance}$ are listed in Table 4.19:

Table 4.19: Resonance frequency, $f_{resonance}$ and relaxation time constant (τ) of $\text{Co}_{1-x}\text{Mn}_x\text{Fe}_2\text{O}_4$

Parameters	x = 0.125	x = 0.25	x = 0.375	x = 0.5
Spin resonance frequency, $f_{resonance}$	4.5 kHz	43 kHz	118 kHz	207 kHz
Relaxation time, $\tau = 1/2\pi f_{resonance}$	37 μ s	13 μ s	1.35 μ s	0.77 μ s

From Table-4.19, it is seen that the relaxation time constant decreases with the Mn content. This signifies the increase in the damping mechanism of wall motion that causes a decrease in the permeability of the material. This damping may arise

from the oxygen vacancies created by Mn^{2+} replacing the Co^{2+} ions in the B site [104]. These oxygen vacancies may be responsible for hindering wall motion and spin rotation.

4.4.2.3 Magnetization (M-H curves)

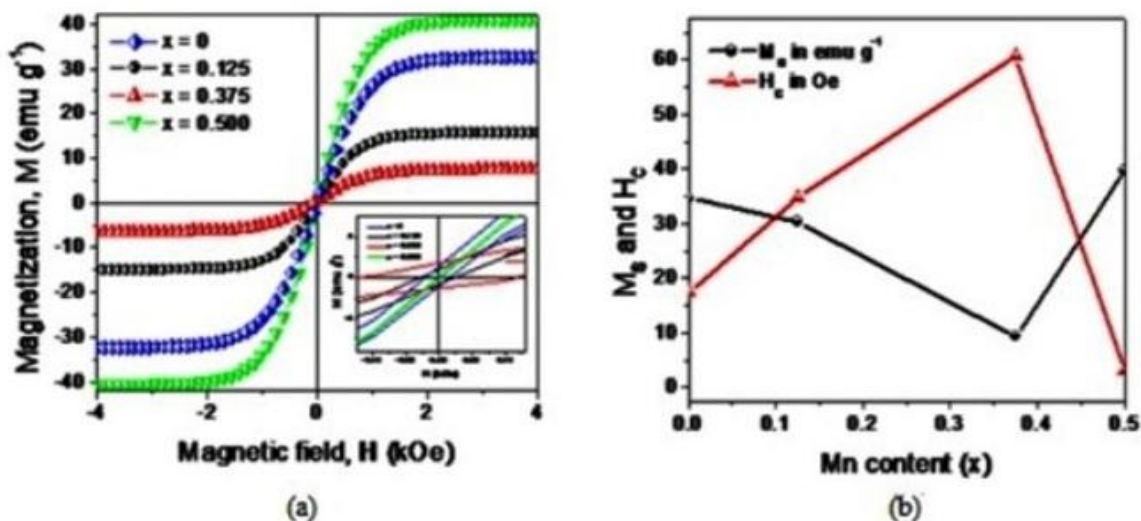


Fig.4.39: (a) M-H Curves (b) the variation of M_s and H_c as a function of Mn content (x) for the samples of $\text{Co}_{1-x}\text{Mn}_x\text{Fe}_2\text{O}_4$, within Mn content ($0 \leq x \leq 0.5$) at RT

The magnetic hysteresis (M - H) loops are recorded at room temperature (RT) for the samples of $\text{Co}_{1-x}\text{Mn}_x\text{Fe}_2\text{O}_4$ with Mn content ($0 \leq x \leq 0.5$) and presented in Fig. 4.39 (a). The M-H curves exhibit almost line hysteresis and are found to be similar nature for each system at room temperature (RT). The saturation magnetization (M_s) is defined here as the magnetization at the field of 4 kOe for the explanation of the variation of magnetization with the Mn content. This saturation magnetization (M_s) and coercivity (H_c) as determined from the hysteresis curves have been used to calculate the remnant magnetization (M_R), anisotropy energy constant, and magnetic moment per formula unit (n_B) in Bohr magnetons (μ_B) [81, 108] and are listed in the table-8.4. The value of M_s for the un-doped Cobalt ferrite (CoFe_2O_4) nanoparticles (i.e. for Mn content, $x = 0$) is found to be 34.68 e.m.u g^{-1} as seen in Table-4.20, which is almost in agreement with the reported value (30 emu g^{-1}) but almost half of the corresponding reported value (60 emu g^{-1}) and also much smaller compared to its bulk counterpart (80 emu g^{-1}) [85, 96] due to surface disorder originating from the broken exchange bonds and high anisotropy on the surface for

the effects of nanosized particles, which leads to non-collinearity of magnetic moments on their surface as explained in the literature [115, 132]. Fig.4.39 (b) shows the variations in M_S and H_C as a function of Mn(x) content (x). From Fig. 4.39 (b), it is observed that initially, M_S decreases with Mn(x) content up to Mn(x) content = 0.375 and then increases up to $x = 0.5$ at RT. The initial decrease in M_S may be ascribed to the usual antiferromagnetic effect of Mn^{2+} in the B site. The increase of M_S may be attributed to the migration of $Fe^{3+}(4\mu_B)$ ions to the A site substituted by $Mn^{2+}(5\mu_B)$ ions in the B site due to particle size confinement effect according to Neel's two sublattices model as explained in the literature [82, 103].

Table 4.20: The magnetic parameters for the samples of $Co_{1-x}Mn_xFe_2O_4$ at room temperature (RT)

System	x	M_S (emu/g)	H_C (Oe)	M_r (emu/g)	K_{eff} erg/Oe	n_B (μ_B)	μ_i
Un-doped (PARENT)	0	34.68	17.50	0.53	632.20	1.46	24.54
CMF System	0.125	15.82	26.05	0.72	429.30	0.66	11.64
	0.375	7.79	125.15	1.23	1015.50	0.32	6.20
	0.5	41.97	1.66	1.24	72.50	1.75	18.97

The initial decrease in M_S may be ascribed to the usual antiferromagnetic effect of Mn^{2+} in the B site. The increase of M_S may be attributed to the migration of $Fe^{3+}(4\mu_B)$ ions to the A site substituted by $Mn^{2+}(5\mu_B)$ ions in the B site due to particle size confinement effect according to Neel's two sublattices model as explained in the literature [11, 85]. However, H_C is found to increase with Mn content (x) up to $x = 0.375$ and afterward to decrease up to $x = 0.5$. This increase in H_C is usual and maintains the inverse relationship with M_S . However, the decrease in H_C may be attributed to the decrease in octahedral Co^{2+} density due to Mn^{2+} substitution [81].

4.4.2.4 Initial Magnetization and Susceptibility

The initial permeability (μ_i) has been measured from the slope of the initial M - H curves as shown in Fig.4.40 (a) for the investigated samples and are listed in

Table 6.5. The nature of variation in μ_i is found to be similar to M_S for similar reasons as explained above. Fig. 4.40 (b) shows the variation of the susceptibility ($\chi = \frac{M}{H}$) as calculated from the M-H curves with the magnetic field. This susceptibility is found to increase with the increase of Co^{2+} concentration that as usually implies the high initial permeability (μ_i) and is the signature of ferrimagnetic-to-ferromagnetic transition in the low field range due to the ferromagnetic ordering of Co^{2+} ions in the B site. Afterward, the susceptibility is seen to decrease with the increase of the magnetic field, which demonstrates the ferromagnetic-to-paramagnetic transition due to the weakening of spin-orbit coupling by the dominance of canting effects for Mn^{2+} ions in the B sublattices in the anisotropy field. The magnitude of χ is found to decrease from the un-doped CoFe_2O_4 for the samples where Mn content, $x = 0.125$, and 0375 due to the presence of the antiferromagnetic effect of Mn^{2+} in their B sublattices.

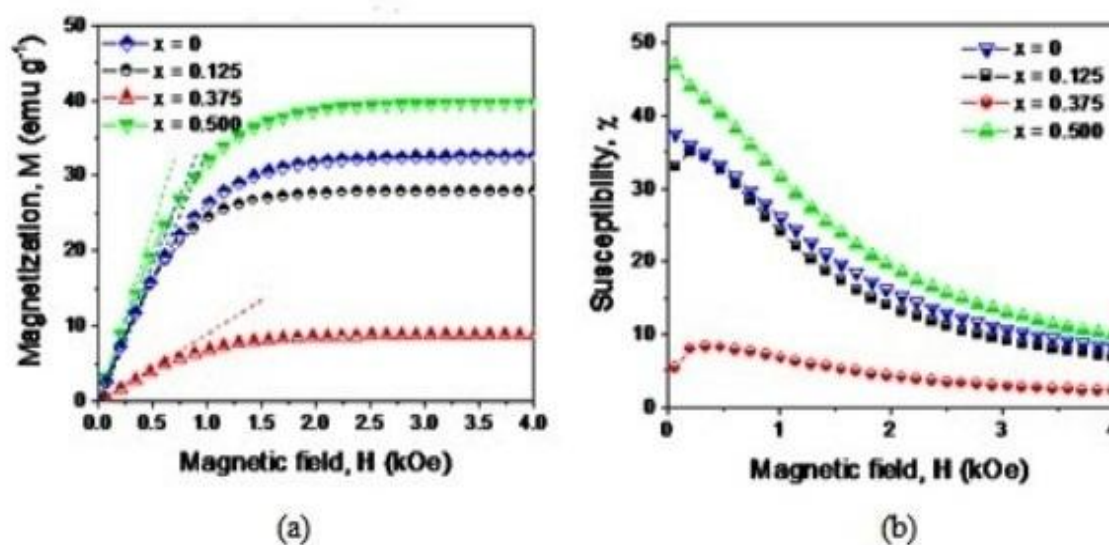


Fig.4.40: (a)Initial M -H curves for the determination of μ_i (b) χ vs. H Curves for the samples of $\text{Co}_{1-x}\text{Mn}_x\text{Fe}_2\text{O}_4$ with different Mn content ($0 \leq x \leq 0.5$) at RT

4.4.3 Electric Properties

To analyze the electric properties of the materials, the Waynekerr impedance analyzer (6500B series) was used to measure the dielectric constant and resistivity using the disc-shaped samples for different Mn content (x), $0.125 \leq x \leq 0.5$ under the variations of both frequency and temperature. Their dc resistivity was also measured by the conventional 4-probe technique as a function of temperature and

magnetic field. However, the significant findings on the analysis of the electrical properties of the materials are explained here in this section.:

4.4.3.1 AC resistivity at the room temperature (RT)

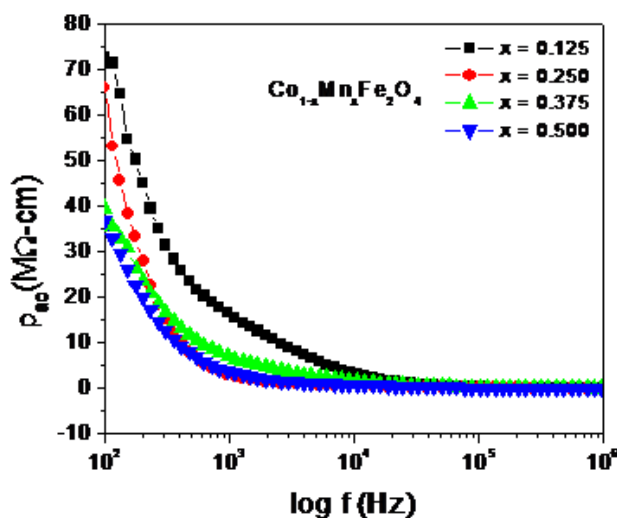


Fig.4.41: AC resistivity for the samples of $\text{Co}_{1-x}\text{Mn}_x\text{Fe}_{2-x}\text{O}_4$ in the frequency range 100 Hz – 1MHz at room temperature (RT)

The variation of ac resistivity (ρ_{ac}) with the frequency is shown in Fig.4.41 on a logarithmic scale for the investigated samples at different Mn content (x). From Fig.4.41 the ac resistivity (ρ_{ac}) is found to decrease with the increase in frequency almost exponentially. This behavior of ρ_{ac} can also be explained based on Maxwell-Wagner interfacial polarization and is in agreement with Koop's phenomenological theory [84], which suggested that the ferrite compact acts as multilayer capacitors and also the grain and grain boundaries have accounted for possessing their different properties. The effect of multilayer capacitors increases with the increase in frequency leading to cause a decrease in ρ_{ac} below 0.01MHz as explained in the literature [133]. Above 0.01MHz, the ac resistivity, ρ_{ac} becomes independent of frequency. However, the ac resistivity ρ_{ac} is found to decrease with the Mn content (x) below 0.01MHz and afterward, the difference in ρ_{ac} is negligibly low that leading it to be independent of Mn content (x). The ac resistivity ρ_{ac} for the samples of $\text{Co}_{1-x}\text{Mn}_x\text{Fe}_{2-x}\text{O}_4$ is found to be higher compared to those of the $\text{CoMn}_x\text{Fe}_{2-x}\text{O}_4$ due to slower mobility of Co^{2+} (p-type carriers) ions in the B site.

4.4.3.2 Dielectric constant

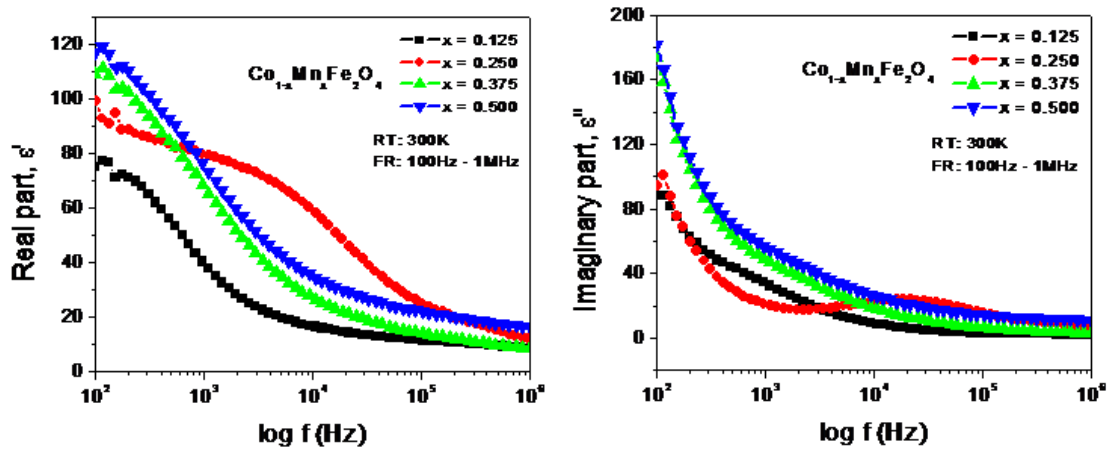


Fig.4.42: (a) Real part, ϵ' as a function of frequency on a logarithmic scale (b) Imaginary part, ϵ'' as a function of frequency on a logarithmic scale for the samples of $\text{Co}_{1-x}\text{Mn}_x\text{Fe}_{2-x}\text{O}_4$ at RT

In an a.c. field, the dielectric constant becomes a complex quantity, which can be expressed mathematically by the relation $\epsilon = \epsilon' - j\epsilon''$ where ϵ' is the real part which represents the stored energy, and ϵ'' is the imaginary part that corresponds to the dissipated energy [134]. The dielectric properties of ferrite materials are influenced by many factors like fabrication method, structural homogeneity, cation distribution, grain size, density, porosity, history of sintering, etc. [135]. Fig.4.42 presents the graphs for both the real part, ϵ' and the imaginary part, ϵ'' of a.c. permittivity as a function of frequency on a logarithmic scale for the samples with different Mn content (x) at the room temperature (RT). Both the real part (ϵ') and imaginary part (ϵ'') of a.c. permittivity is found to decrease with the increase in applied frequency and exhibit the normal behaviors shown in Fig.4.42(a) and (b). This behavior can be explained based on the Maxwell Wagner polarization model, which states that the conductivity and dielectric have the common origin of charge carriers and hopping between Fe^{2+} and Fe^{3+} ions [78]. At lower frequencies, the hopping frequency of charge carriers follows the frequency of the applied field, which increases the dielectric constant. However, at higher frequencies, the hopping frequency of charge carriers lags behind the applied field and hence the dielectric constant (permittivity) decreases due to the random dipolar orientations up to around 100 kHz [103]. Afterward, the dielectric constant becomes almost independent of

applied frequency and it is most likely for the only electronic contribution in their polarization. However, in the low-frequency regime i.e. below 400 Hz, the magnitudes of dielectric constant are found to increase with Mn content (x). Afterward, it follows the same trend other than for the sample of Mn content $x = 0.25$. This increasing trend of dielectric constant with the Mn content may be due to the decreased density of Co^{2+} ions for being replaced by Mn^{2+} ions in the B site. However, the increased magnitude of dielectric constant for Mn = 0.25 seems to be unpredictable.

4.4.3.3 AC conductivity at the room temperature (RT)

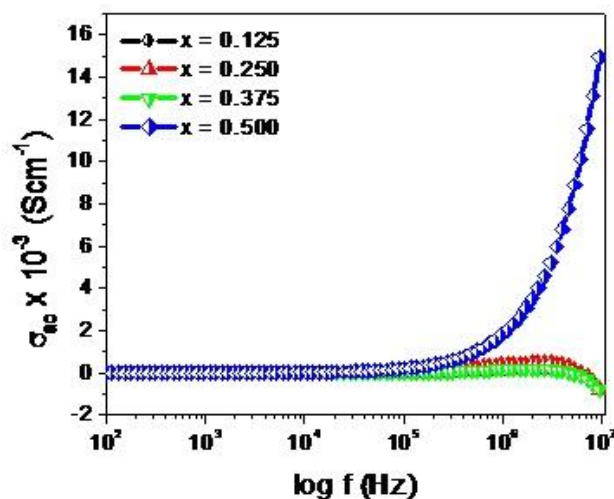


Fig.4.43: AC conductivity for the samples of $\text{Co}_{1-x}\text{Mn}_x\text{Fe}_{2-x}\text{O}_4$ at RT in the frequency range 100 Hz – 10 MHz

The ac conductivity as determined from ϵ'' using equation $\sigma_{ac} = \omega \epsilon'' \epsilon_0$ (symbols bear the usual meanings) is plotted as a function of frequency in Fig.4.43. The ac conductivity, σ_{ac} remains almost constant up to 100kHz. This conductivity may be accounted as dc conductivity, σ_{dc} , which may be associated with the diffusion of charge carriers through the grain boundaries. However, in the higher frequencies ($>100\text{kHz}$), the ac conductivity, σ_{ac} is found to increase almost exponentially that may be associated with the local hopping of charge carriers in the grains. Again a turning to the lower value of σ_{ac} is observed at around 4.5 MHz, which might occur due to unharmonic vibrations for the coexistence of antiferromagnetic and ferromagnetic clusters [133].

4.4.3.4 Electric modulus

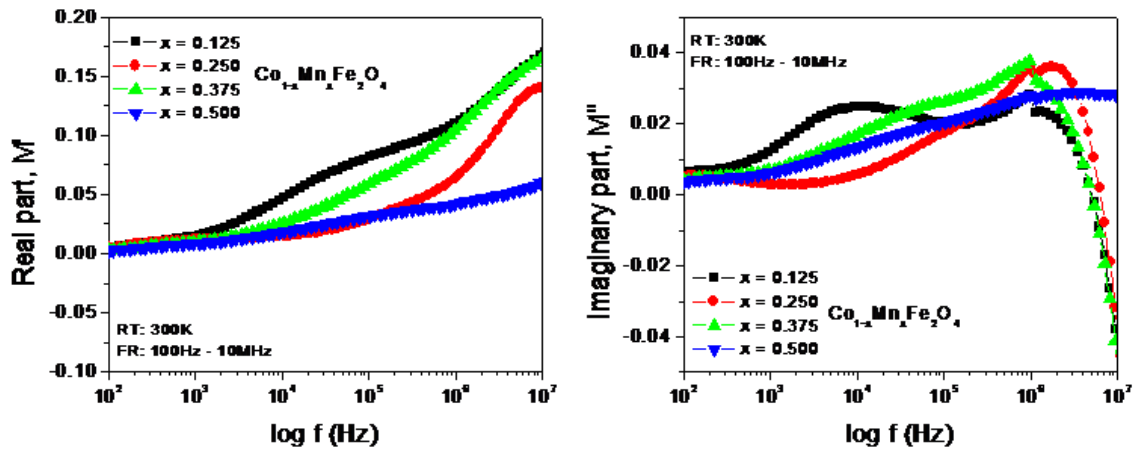


Fig. 4.44: (a) Real part, M' , (b) Imaginary part, M'' of electric modulus as a function of frequency, for the sample of $\text{Co}_{1-x}\text{Mn}_x\text{Fe}_2\text{O}_4$ at RT in the frequency range 100Hz–10MHz

Fig. 4.44 (a) shows the variation of the real part of electric modulus (M') with the frequency on a logarithmic scale at room temperature (RT). The values of the M' approach to almost zero in the low-frequency regime. This fact marks the negligible contribution of electrode polarization in the materials [72, 73, 103–129]. An increasing trend in M' with the applied frequency is observed for the samples. The increasing trend may have originated from the short-range mobility of charge carriers (p-type and n-type)[136] due to shorted hopping length (L_B) in the B site [73]. Fig.4.44 (b) shows the variation of M'' with the increase in frequency on a logarithmic scale at RT. In the low-frequency regime, the higher values of M'' indicates lower conductivity and the higher dielectric constant arising from the Maxwell-Wagner interfacial polarization in the grain boundaries. This polarization is expected to have originated from the hopping of electrons between Fe^{2+} and Fe^{3+} ions in the direction of the applied electric field, and between Co^{3+} and Co^{2+} ions in the opposite direction across the grain boundaries. The well-resolved peaks are found to appear at the characteristic frequency (f_{max}) in their $M''(f)$ spectra other than for the sample of Mn content ($x = 0.5$). These peak positions are found to depend on the Mn content but not sequentially and predictably. The characteristic frequency (f_{max}) determined from the corresponding peak, and the relaxation time (τ) estimated by the equation ($\tau = 1/2\pi f_{max}$) [124, 156] are presented in Table-4.21

Table 4.21: Characteristic frequency (f_{max}) and relaxation time (τ)

Parameters	x=0.125	x=0.250	x=0.375
f_{max} , determined from peaks	1MHz	1.8MHz	938kHz
τ , estimated by $\tau = 1/2\pi f_{max}$	0.16 μ s	0.09 μ s	0.17 μ s

From Table-4.21, both the characteristic frequency and relaxation time are found to differ with the Mn content (x). However, the minimum relaxation time constant is obtained for the Mn content 0.25, which implies the higher hopping rate.

4.4.3.5 Significance of Nyquist plot of electric modulus

Fig.4.45 presents the Nyquist plot of electric modulus for the samples of $\text{Co}_{1-x}\text{Mn}_x\text{Fe}_{2-x}\text{O}_4$ at different Mn content (x). As seen in Fig.4.45, a depressed single semicircle of non-ideal shape is observed for the samples of Mn content 0.25 (b), 0.375 (c), 0.5 (d). They demonstrate no-Debye type dielectric relaxation with single relaxation time constant but a similar type of double semicircles are observed for the sample of Mn content 0.125 (a), which exhibits the contribution of the grains and grain boundaries in its dielectric relaxation. In the high-frequency regime, the higher values of the imaginary part, M'' signifies lower conductivity and thereby the higher dielectric constant due to Maxwell-Wagner interfacial polarization. This fact has been confirmed from all the Nyquist plots. Conversely, in the lower-frequency regime, the higher values of M' represent higher conductivity as evident from these Nyquist plots. The higher conductivity may have originated by the increased hopping rate between charge carriers across the grain boundaries in the B-site. Besides, the negative value of the imaginary part of modulus, M'' is assumed to cause from the hopping of ions in the opposite direction [110]. The hopping between Fe^{2+} to Fe^{3+} is considered in the positive direction and Co^{2+} to Co^{3+} in the opposite direction as mentioned above. Hence, the dominance of carrier type can easily be identified from the Nyquist plots. As such, n-type ($\text{Fe}^{2+}/\text{Fe}^{3+}$) plays a dominant role in the hopping process for the sample of Mn content 0.5 across the grain boundaries in the B site. Conversely, the p-type ($\text{Co}^{2+}/\text{Co}^{3+}$) carriers are found to play its role in the hopping process across the grain boundaries for the sample of Mn content 0.125, 0.25, and 0.375 [72, 74, 103].

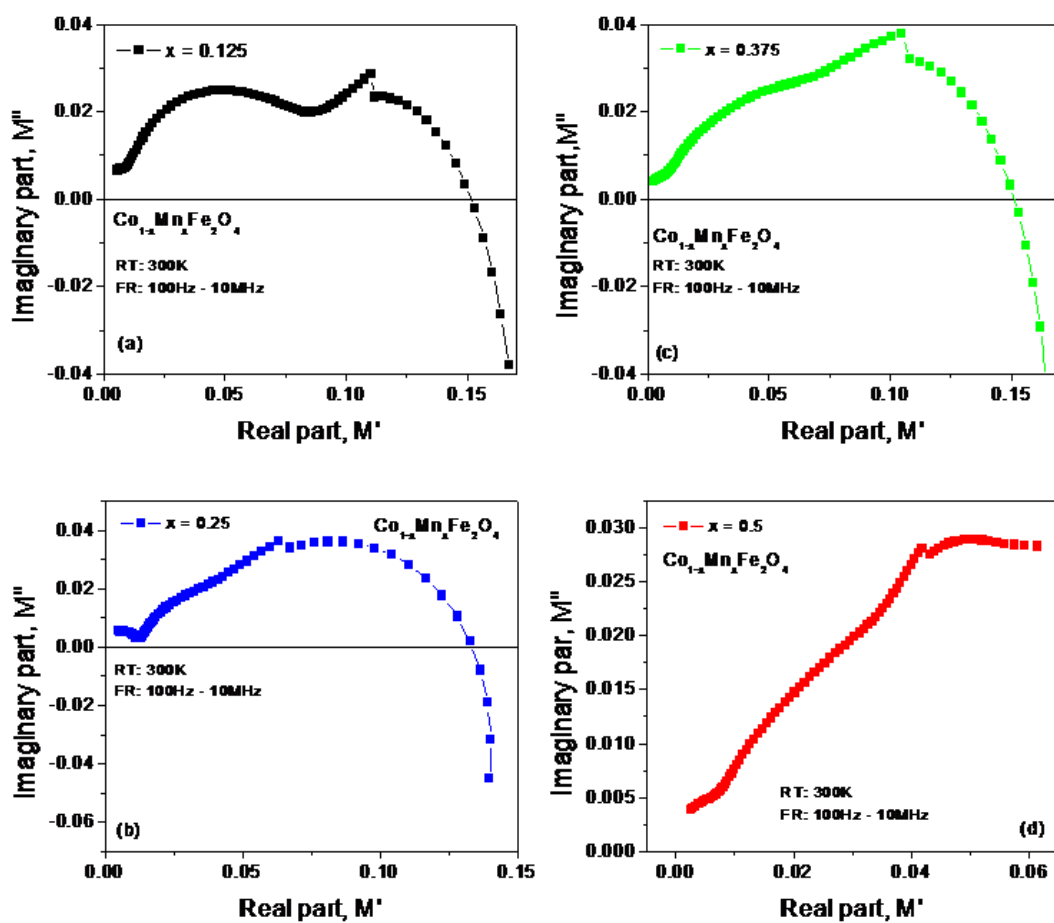


Fig.4.45: Nyquist plot or electric modulus for the sample of $\text{Co}_{1-x}\text{Mn}_x\text{Fe}_2\text{O}_4$ at Mn content (a) $x = 0.125$ (b) $x = 0.25$ (c) $x = 0.375$, and (d) $x = 0.5$ in the frequency range 100Hz – 100MHz

4.5 Comparison of Three Systems on the Manifested Properties

A brief comparison on significant demonstrated properties have been presented in tabular form in Tabl 4.22:

Table 4.22: Comparison of three compositions on significant demonstrated properties

Parameters	CFMZ system	CMF system	CFM system
Lattice constant	Decreasing trend with x	Decreasing trend with x	Decreasing trend with x
Crystallite size	Larger but decreasing trend	Smaller but increasing trend	Smaller but increasing trend
Particle size	Decreasing trend	Increasing trend	Decreasing trend
Electric modulus	A boundary between short-range and long-range mobility of charge carriers	-	-
Nyquist Plot	Single semicircle observed	Single semicircle observed	Two depressed semicircle observed.
Magnetic modulus	Crossover frequency observed	-	-
Glass transition state	Observed in the low temperature regime	Not observed	Observed in the low temperature regime
Impedance spectroscopy	Double conducting frequency band observed	Single conducting frequency band observed	-

CHAPTER – V

CONCLUSION AND RECOMMENDATION

5.1 Conclusion

The demonstrated semiconducting nature in the non-stoichiometric composition $\text{Co}_{1+x}\text{Mn}_x\text{Fe}_{2-x}\text{O}_4$ may make this material suitable to be used in the thermoelectric devices. The eddy current loss that is expected at the resonance due to a higher conductivity in the magnetic modulus of this non-stoichiometric composition may make this material applicable in hyperthermia or related research in medical science. The equality in the real part and imaginary parts of complex permittivity at resonance suggests this material to use in the high-frequency switching devices. The exponential decreasing rate of resistivity with the applied magnetic field in the non-stoichiometric composition at room temperature may make this sample suitable to be used in the field of position and biosensors. The increasing nature of magnetization with the temperature at constant concentration levels x provides the ability to control and probe the magnetization of the material and thus make the system suitable to be used in the field of sensor applications. The decreasing trend in coercivity H_C from a certain peak temperature is observed in $\text{Co}_{1+x}\text{Mn}_x\text{Fe}_{2-x}\text{O}_4$ that may make this sample suitable to be used as ferrite cores in high-frequency inductors, transformers and antennas in the low-temperature regime. The negative magnetoresistance and its variation nature of this non-stoichiometric composition may be used to identify the types of charge carriers and to probe the material's capability to control the electron transport properties in the sensor and spintronics applications. The dispersion of the real part of permeability in the stoichiometric composition of manganese doped cobalt nanoferrite with composition formula $\text{Co}_{1-x}\text{Mn}_x\text{Fe}_2\text{O}_4$ is found to be almost independent over the frequency band 550Hz – 1MHz that makes this material a good candidate to be used in high-frequency applications. Besides, the observed single metallic frequency band in $\text{Co}_{1-x}\text{Mn}_x\text{Fe}_2\text{O}_4$ may make this material suitable to be used in radiofrequency switches. The varied nature of temperature dependent resistivity in the material of composition $\text{CoMn}_x\text{Fe}_{2-x}\text{O}_4$ may make the material suitable to be used in the high temperature sensor devices. However, the use of manganese doped cobalt ferrite nanoparticles in

the application of hyperthermia, it is required to ascertain and quantify the generated heat in the subject material, which in turn demands a further investigation on that perspective.

5.2 Recommendations

It is suggested/recommended to carry out further researchs on these materials on the following aspects to exploit/explore their usability in other fields of applications:

- i. The magnetocaloric effects for analyzing its suitability to be used in the magnetic refrigerator.
- ii. The photocatalytic conversion of visible solar energy to generate e^-/h^+ , which in turn may produce reactive oxygen species through the redox process for the degradation of pollutants in water.
- iii. In a quest of exploring new alternatives of RE permanent magnets by investigating non-stoichiometric manganese doped cobalt ferrites and compositing it to Nickel to enhance magnetism and coercivity.
- iv. An investigation of this material is required to enhance dye degradation capability.
- v. Improvement of the efficiency and savings of energy in renewable energy devices using cobalt ferrite nanoparticles with non-stoichiometric composition.

REFERENCES

-
- [1] Jadhav, P. A., Devan, R. S., Kolekar, Y. D., and Chougule, B. K., "Structural, electrical and magnetic characterizations of Ni–Cu–Zn ferrite synthesized by citrate precursor method", *J. Phys. Chem. Solids* vol.70, pp. 396-400, 2009.
- [2] Bayoumi, W., "Structural and electrical properties of zinc-substituted cobalt ferrite", *J. Mater.Sci.* vol. 42, pp. 8254 – 8261, 2007.
- [3] Patange, S. M., Shirsath, S. E., Toksha, B. G., Jadhav, S. S., and Jadhav, K. M., "Electrical and Magnetic properties Cr³⁺ substituted nanocrystalline nickel ferrite ", *J. Appl. Phys.* vol. 106, pp. 023914-1 – 023914-7, 2007.
- [4] Vasundhara, N. K., Achary, S. N., Deshpande, S. K, Babu, P. D., Meena, S. S., and Tyagi, A. K. "Size-dependent magnetic and dielectric properties of nano CoFe₂O₄ prepared by a salt assisted gel-combustion method", *J. Appl. Phys.* vol. 113, pp.194101-1- 194101-9, 2013.
- [5] Nongjai, R., Khan, S., Asokan, K., Ahmed, H., and Khan, I., "Magnetic and electrical properties of In doped cobalt ferrite nanoparticles", *J.Appl.Phys.* vol. 112, pp. 084321-1084321-8, 2012.
- [6] Ahsan, M. Z., and Islam, M. A. "A Theoretical Approach: Effects of Mn Substitution in Cobalt Ferrite", *American J. of App. Sci. Res.*, vol. 5(3), pp. 56-61 2019.
- [7] Bawa Waje, S., Hashi, M., and Ismail, I., "Effects of sintering temperature on the grain growth and complex permeability of Co_{0.3}Ni_{0.3}Zn_{0.5}Fe₂O₄ material prepared using mechanically alloyed nanoparticles", *J. Magn. Magn.Mater.* vol. 323, pp. 1433 – 1439, 2011.
- [8] Atif, M., Idrees, M., Nadeem, M., Siddique, M., and Ashraf, M. W., "Investigation on the structural, dielectric and impedance analysis of manganese substituted cobalt ferrite *i.e.*, Co_{1-x}Mn_xFe₂O₄ (0.0 ≤ x ≤ 0.4)", *RSC Adv.* vol. 6, pp. 20876-20885, 2016.
- [9] Khan, F. A., and Ahsan, M. Z., "Study of structural and magnetic properties of manganese doped cobalt ferrite nanoparticles for high frequency and sensor application", *J Mat.Sci.Eng.* vol. 6 (7), 2017.
- [10] Supriya, S., Kumar, S., and Manoranjan, K., "Correlation between AC and DC transport properties of Mn substituted Cobalt ferrite", *J. App. Phys.*, vol. 120, pp. 215106, 2016.
- [11] Caltun, O.F., Rao, G.S.N., Rao, K. H., Rao, B.P., GiKim, C., OhKim, C., Dumitru, I., Lupu, N., and Chiriac., H., "High Magnetostrictive Cobalt ferrite for sensor applications", *Sensor Lett.*, vol. 5, pp. 1-3, 2007.

- [12] Nlebem, I.C., Moses, A.J., and Jiles, D.C., "Non-stoichiometric cobalt ferrite, $\text{Co}_x\text{Fe}_{3-x}\text{O}_4$ ($x= 1.0$ to 2.0) structural, magnetic and magnetostrictive properties", *J. Magn. Magn.Mater.*, vol. 343, pp. 49-54, 2013.
- [13] Adeela N., Khan, M., Khan, U., Iqbal, M., Riaz, S., and Naseem, S., "Temperature-dependent magnetic response of antiferromagnetic doping in cobalt ferrite nanostructures", *Nanomaterials* vol. 6(73), pp. 1-13, 2016.
- [14] Xavier, S. "Effect of dysprosium substitution on structural and magnetic properties of cobalt ferrite nanoparticles", *Int. J. Eng. Sci. Inno.Tech.*, vol. 4 (5), pp. 91-96, 2015.
- [15] Mariano, M. R., Mietta, J. L., Soledad P., A., Perez, O. E., Negri, M. M., and George, G., "Structural and magnetic properties of $\text{Fe}_{2-x}\text{CoSm}_x\text{O}_4$ and $\text{Fe}_{2-x}\text{CoSm}_x\text{O}_4$ -PDMS magneto elastomers as a function of Sm content", *J. Magn.Magn mater.*, vol. 327, pp.11-19, 2013.
- [16] Xavier, S., Thankachan, S., Binu., Jacob, P., and Mohammed, E.M., "Effect of Samarium substitution on the structural and magnetic properties of Nanocrystalline cobalt ferrite", *J. Nanosci.*, vol. 20(13), pp. 1-7, 2013.
- [17] Nasrin, S., Haque, M. S., Chowdhury, F.-U. -Z, and Hossein, M. M., "Influence of Zn substitution on the structural and magnetic properties of $\text{Co}_{1-x}\text{Zn}_x\text{Fe}_2\text{O}_4$ nano-ferrites", *J.App.Phys*, vol. 6 (2), pp. 58-66, 2014.
- [18] Singhal, S., Namgyal, T., Bansal, S., and Chandra, K., "Effect of Zn substitution on the magnetic properties of cobalt ferrite nanoparticles prepared via sol-gel route", *J.Elect. Analys. & Appli.*, vol. 2, pp. 376-381, 2016.
- [19] Kumar, H., "Structural and magnetic properties of dysprosium substituted cobalt ferrite nanoparticles", *J.Magn. Magn.Mater.* vol. 401, pp. 16-21, 2016.
- [20] Paulsen, J. A., Ring, A.P., Lo, C.C.H., Snyder, J. E., and Jiles, D.C., "Manganese substituted cobalt ferrite magnetostrictive materials for magnetic stress sensors application", *J. Appl. Phys*, vol. 97, pp. 044502, 2005.
- [21] Caltan, O., Dumitru, I., Feder, M., Nupu, N., and Chiriac, H., "Substituted cobalt ferrites for sensor applications", *J.Magn. Magn. Mater.*, vol. 320, pp. 869-873, 2008.
- [22] Caltun, O.F., Rao, G.C.N., Rao, K. H., Rao, B.P., Gi Kim, C., Oh Kim, C., Dumitru, I., LupuN., and Chiriac, H., "High magnetostrictive Cobalt ferrite for sensor applications", *Sensor Lett.*, vol. 5 (6), pp. 1-3, 2016.
- [23] Ajroudi, L., Villain, S., Madigan, V., Maliki, N., and Leroux, C., "Synthesis and microstructure of cobalt ferrite nanoparticles", *J. Cryst. Growth*, vol. 312, pp. 24-65, 2010.

- [24] Kumar, H., “FTIR and electrical study of dysprosium doped cobalt ferrite nanoparticles”, *J. Nanosci.*, vol. 2014, pp. 1-10, 2014.
- [25] Khan, A., “Dielectric and transport properties of Zn substituted cobalt ferrite”, *J. Bang. Ac. of Sci.*, vol. 37 (1), pp. 73-82, 2013.
- [26] Farooq, H., “Structural and dielectric properties of Mg ferrite nanoparticles”, *J. Basic Appl.*, vol. 8, pp. 597-601, 2012.
- [27] Kadam, A. A., Shinde, S. S., Yadav, S. P., Patil, S. P., and Rajpur, and K. Y., “Structural, morphological, electrical and magnetic properties of Dy doped Ni-Co substitutional spinel ferrite”, *J. Magn. Mater.*, vol. 329 pp. 59-64, 2013.
- [28] Tapdiya, S., Ashwani K. Shrivastava, and Singh, S., “Effect of Mn substitution on structural and magnetic properties of cobalt ferrite”, *Adv. Mate. Proc.*, vol. 2(9), pp. 547-551, 2017.
- [29] Ponpandian, N., Balaya, P., and Narayanasamy, A., “Electrical Conductivity and Dielectric Behaviour of Nanocrystalline NiFe₂O₄ Spinel”, *J. Phys. Cond. Mater.* vol. 14, pp. 3221–3237, 2002.
- [30] Rani, R., Kumar, G., Mujasam K.B., and Singh, M., “Electric and Dielectric Study of Zinc Substituted Cobalt Nanoferrites Prepared by Solution Combustion Method”, *American J. Nanomater.*, vol. 1(1), pp. 9-12, 2013.
- [31] Atif, M., Idrees, M., Nadeem, M., Siddique, M., and Ashraf, M. W., “Investigation on the structural, dielectric and impedance analysis of manganese substituted cobalt ferrite, Co_{1-x}Mn_xFe₂O₄ (0.0 ≤ x ≤ 0.4)”, *RSC Adv.*, Vol. 25, pp. 20453- 21292, 2016.
- [32] Maurya., J.C. Bhaskar. S.V., and Mathe, V.L., “Effect of manganese substitution on magnetoimpedance and magnetostriction of cobalt ferrites”, *Physica B: Condens. Matter.* vol. 436, pp. 220-226, 2014.
- [33] Zhihong, Y., Zhengwen, and LiYanhui, Y., “Novel Frequency Dispersion of Permeability in Nickel Ferrites with Different Amounts of Cobalt Doping”, *IEEE Trans. Magn.*, vol. 50(1), pp. 1-4 2013.
- [34] Kumar, L., Kumar, P., and Manoranjan, K., “Influence of Mn substitution on crystal structure and magnetocrystalline anisotropy of nanocrystalline Co_{1.2x}Mn_xFe_{2.22x}Mn_{2x}O₄”, *Appl. Nanosci.*, vol. 3, pp. 75–82 2013.
- [35] Supriya, S., Kumar, S., and Manoranjan, K., “Correlation between AC and DC transport properties of Mn substituted cobalt ferrite”, *J. App. Phys.* vol. 120, 215106, 2016.
- [36] Azam A., Arham S. A., Chaman, M., and Naqvi, A. H., “Investigation of

- electrical properties of Mn-doped tin oxide nanoparticles using impedance spectroscopy”, *J. App. Phys.* vol. 108 (09), 4329, 2010.
- [37] Birajdar, A. A., Sagar E. Shirsath, Kadam, R. H., Mane, M. L., Mane, D. R., and Shire, A. R., “Permeability and magnetic properties of Al^{3+} substituted $Ni_{0.7}Zn_{0.3}Fe_2O_4$ nanoparticles”, *J. App.Phys.* vol. 112(5), 053908, 2012.
- [38] Nongjai, R., Shakeel Khan, S., Asokan, K., Ahmed, H., and Khan, I., “Magnetic and electrical properties of In doped cobalt ferrite nanoparticles”, *J. App. Phys.* vol. 112, 084321, 2012.
- [39] Ashish, S., Kumar, P., Ravelo, B., Lallechere, S., Thakur, A., and Thakur, P., “Magneto-dielectric properties of doped ferrite based nanosized ceramics over very high-frequency range”, *Eng. Sci. and Techn.*, , vol. 19, pp. 911-916, 2016.
- [40] Sichuan, Li., Vijay, T., Johna, Charles, O’C., Harris, V., and Carpenter, E., “Cobalt-ferrite nanoparticles: Structure, cation distributions, and magnetic properties”, *J. Appl. Phys.*, vol. 87(9), pp. 6223-6225, 2000.
- [41] Jacob, J., and Khader, M. A., “Investigation of mixed spinel structure of nanostructured nickel ferrite”, *J. App. Phys.* vol. 107, pp. 114310, 2010.
- [42] Arabi, H., and Ganjali, F., “Structural and Magnetic Properties of Cobalt and Manganese Doped Ni-Ferrite Nanoparticles”, *J. Supercond. Nov. Magn.*, vol. 26, pp. 1031–1035, 2013.
- [43] Waje, S.B., Hashim, M., and Ismail, I., “Effects of sintering temperature grain growth and complex permeability of $Co_{0.2}Ni_{0.3}Zn_{0.5}Fe_2O_4$ material prepared using mechanically alloyed nanoparticles”, *J. Magn. Mater.*, vol. 323, pp. 1433-1439, 2011.
- [44] Hansen, R.C., and Burke, M., “Antennas with magneto-dielectrics”, *Microw.Opt.Techno. Lett.* vol. 26, pp. 75–78, 2000.
- [45] Saini, A., Thakur, A., and Thakur, P., “Matching permeability and permittivity of $Ni_{0.5}Zn_{0.3}Co_{0.2}In_{0.1}Fe_{1.9}O_4$ ferrite for the substrate of large bandwidth miniaturized antenna”, *J. Mater. Sci.*, vol. 27(3), pp. 2816-2823, 2015.
- [46] Sailni, A., Thakur, A., and Thakur, P., “Effective Permeability and Miniaturization Estimation of Ferrite-loaded Microstrip Patch Antenna”, *J. Elec. Mat.*, vol. 45 (8), pp. 4162-4170, 2016.
- [47] Jeppson, P., Sailer R., Jarabek, E., Sandstrom, J., Anderson, B., Bremer, M., Grier, D. G., Schulz, D. L., Caruso, A. N., Payne, S. A., Eames, P., Tondra, M., Hongshan H., and Chrisey, D. B., “Cobalt ferrite nanoparticles: Achieving the superparamagnetic limit by chemical reduction”, *J. Appl.*

- Phys. vol. 100, 114324, 2006.
- [48] Carvalho, F.E., Lemos, L.V., Migliano, A.C.C., Machado, J.P.B., and Pullard, R.C., “Structural and complex electromagnetic properties of cobalt ferrite (CoFe₂O₄) with an addition of niobium pentoxide”, (2018), *Ceram. Int.*, vol. 44, pp. 915–921, 2018.
- [49] Baldi, G., Lorenzi, G., and Ravagli, C., “Hyperthermic effect of magnetic nanoparticles under the electromagnetic field”, *Process. Appl. Ceram.*, vol. 3, pp. 103–109, 2009.
- [50] Fiorillo, F., Beatrice, C., Bottauscio, O., and Carmi, E., “Eddy-Current Losses in Mn-Zn Ferrites”, *IEEE Trans. Magn.*, vol. 50(1), pp. 1-9, 2014.
- [51] Tapdiya, S., Ashwani, K., Shrivastava, and Singh, S., “Effect of Mn substitution on structural and magnetic properties of cobalt ferrite”, *Adv. Mater. Proc.*, vol. 2(9), pp. 547-551, 2017.
- [52] Melikhov, Y., Snyder, J. E., Jiles, D. C., Ring, A. P., Paulsen, J. A., Lo, C. C., and Dennis, H. K. W., “Temperature dependence of magnetic anisotropy in Mn-substituted cobalt ferrite”, *J.App. Phys*, vol. 99, pp. 08R102, (2006).
- [53] George, T., Sunny, A. T., and Varghese, T., “Magnetic properties of cobalt ferrite nanoparticles synthesized by sol-gel method”, *IOP Conf. Series: Mater. Sci. and Eng.*, vol. 73, 012050, 2012.
- [54] Kambale, R C, Shaikh, P A, Bhosale, C H, Rajpure, K Y, and Kolekar, Y D., “The effect of Mn substitution on the magnetic and dielectric properties of cobalt ferrite synthesized by an auto combustion route”, *Smart Mater. Struct.* vol. 18, pp. 115028, 2009.
- [55] Kolekar, Y.D., Sanchez, L., Rubio, E.J., and Ramanan C.V., “Grain and grain boundary effects on the frequency and temperature dependent dielectric properties of cobalt ferrite–hafnium composites”, *Solid State Commun.* vol. 184, pp. 34-39, 2014.
- [56] Ramesh, T., and Murthy, S R., “Electromagnetic properties of nanocrystalline Al³⁺ substituted MgCuMn ferrites synthesized by microwave hydrothermal method”, (2016), *Bull. Mater. Sci.*, vol. 39 (6), pp. 1593–1601, 2016.
- [57] Shabnam, S. K., Prasad, P.D., and Manjura, H. K., “Effect of Temperature on the Structural and Magnetic Properties of CuFe₂O₄ NanoParticle Prepared by Chemical Co-Precipitation Method”, *Int. J. Mater., Mech. and Manufac.*, vol. 2 (1), pp. 5-6, 2014.
- [58] Carvalho, F. E., Lemos, L.V., Migliano, A.C.C., Machado, J.P.B., and Pullard, R.C., “Structural and complex electromagnetic properties of cobalt ferrite (CoFe₂O₄) with an addition of niobium pentoxide”, *Ceram. Int.*, vol.44, pp. 915-921, 2018.

- [59] Pubby, K., Meena, S.S., Yusuf, S.M., and Naranga, S. B., “Cobalt substituted nickel ferrites via Pechini’s sol-gel citrate route: X-band electromagnetic characterization”, *J. Magn.Mag. Mat.* vol. 466, pp. 430-445, 2018.
- [60] Stein, C.R., Bezerra, M.T.S., Holanda, G.H.A., and r´e-Filho, J., “Structural and magnetic properties of cobalt ferrite nanoparticles synthesized by coprecipitation at increasing temperatures”, *AIP Adv.*, vol. 8, 056303, 2018.
- [61] Yu`ksel Ko`seog`lu, Furkan Alan, Muhammed Tan, Resul Yilgin, and Mustafa O`ztu`rk, “Low-temperature hydrothermal synthesis and characterization of Mn-doped cobalt ferrite nanoparticles”, *Ceram. Int.*, vol. 38 (5), pp.3625-3634, 2012.
- [62] Jabbar, R. Sabah H.Sabeeh, Newham M. and Hameed, “Structural, dielectric and magnetic properties of Mn^{+2} doped cobalt ferrite nanoparticles”, *J. Magn. Magn. Mat.* vol. 494, 165726, 2020.
- [63] Bakker, H., Zhou, G.F., and Yang, H., “Mechanically driven disorder and phase-transformations in alloys”, *Progress in Materials Science*, vol. 39, 159241, 1995.
- [64] Globus, A., Passcard, H., and Cagan, V., “Distance between magnetic ions and fundamental properties in ferrites”, *J. Phys. Colloquia*, C1, suppl. vol. 38 (C1), pp.C1-163-C1-168, 1977.
- [65] Asano, K., Enoki, H., and Akiba, E., “Synthesis of HCP, FCC and BCC structure alloys in the Mg-Ti binary system employing ball milling”, *J. Alloys and Compounds*, vol. 480, pp. 558-564, 2009.
- [66] Sinha, B., “Investigation of frequency-dependent permeability of Ca, Mg and Ti substituted Mn-Zn ferrite”, M. Phil Thesis, Department of Physics, Bangladesh University of Egineering and Technology, 2005.
- [67] Suk-Joong, K., “Sintering Densification, Grain Growth, and Microstructure” Elsevier Butterworth-Heinemann Linacre House, Jordan Hill, Oxford OX2 8DP 30 Corporate Drive, Burlington, MA 01803, 2005.
- [68] Castricum, H. L., “Mechanically induced chemical and structural changes in materials”, Ph.D. thesis, University of Amsterdam, 2001.
- [69] Provenzano, V., Della Torre, E., and Bennett, L. H.. “Study of Magnetizing Processes in $Ni_{50}Mn_{35}In_{15}$ Heusler Alloy”. *IEEE Trans. Magn.*, vol. 49(9), pp. 4956–4959, 2013.
- [70] Purnama, B., Tri Wijayanta, A., and Suharyana, “Effect of calcination temperature on structural and magnetic properties in cobalt ferrite nanoparticles”, *J. King Saud Univ. Sci.*, vol. 31, pp. 956-960, 2019.
- [71] Ahsan, M. Z., and Khan, F. A., “Study of Structural, Electrical and Magnetic

- Properties of Manganese Doped Cobalt Ferrite Nanoparticles with Non-stoichiometric Composition”, *J. Phys. Sci. app.*, vol. 7(6), pp.30-37, 2017.
- [72] Ahsan, M. Z., Khan, F. A., and Islam, M.A., “Frequency and temperature dependent intrinsic electric properties of manganese doped cobalt ferrite nanoparticles”, *Results in Phys.*, vol. 14, 102484-1 – 102484-7, 2019.
- [73] Ahsan, M. Z., Islam, M. A., Bally, A. A., and Khan, F. A., “Spectroscopic analysis for electric and magnetic properties of manganese doped cobalt nanoferrite”, *Results in Phys.*, vol. 17, pp. 103172, 2020.
- [74] Jian Chin C., Wen-ChngC., Yin-Chun T., and Chi-Jen S., “Effect of calcination temperature on the crystallite growth of cerium oxide nanopowders prepared by the co-precipitation process”, *J. Alloys Compd*, vol. 496(1), pp. 364-369, 2010.
- [75] Toby, B. H. “R factors in Rietveld analysis: How good is good enough?” *Powder Diffraction*, vol. 21(01), pp. 67–70, 2006.
- [76] Rećko, K., Waliszewski, J., Klekotka, U., Soloviov, D., Ostapczuk, G., Satuła, D., ... and Szymański, K., “Phase composition and magnetism of sol–gel synthesized Ga–Fe–O nanograins”, *Phase Trans.*, vol. 91(2), pp. 128–139, 2017.
- [77] Purnama, B., Tri Wijayanta, A., and Suharyana, “Effect of calcination temperature on structural and magnetic properties in cobalt ferrite nanoparticles”, *J. King Saud Univ. Sci.*, vol. 31, pp. 956-960, 2019.
- [78] Xavier, S., Thankachan, S., Binu. P. Jacob, and Mohammed, E.M., “Effect of Samarium substitution on the structural and magnetic properties of Nanocrystalline cobalt ferrite”, *J. Nanosci.*, vol. 2013, pp. 1-7, 2013.
- [79] Khandker, M. S., Kambale, R., Patil, J. Y., Kolekar, Y. D., and Suriyavanshi, S. S., “Effect of calcination temperature on the structural and electrical properties of cobalt ferrite synthesized by combustion method”, *Journal of Alloy's compounds*, vol. 509(5), pp. 1861-1865, 2011.
- [80] Ahsan, M. Z., and Khan, F. A., “Structural and electrical properties of manganese doped cobalt ferrite nanoparticles”, *Mater Sci. Nanotechnol.*, vol. 2(2), pp. 1-9, 2018.
- [81] Tapdiya, Ashwani K., Shrivastava, and Sing, S., “Effect of Mn substitution on structural and magnetic properties of cobalt ferrite”, *Adv. Mater. Proc.*, vol. 2(9), pp. 547-551, 2017.
- [82] Ahsan, M. Z., Khan, F. A., and Islam, M. A., “Influence of Milling Time on Structural and Electromagnetic Properties of Manganese Doped Cobalt Ferrite Nanoparticles”, *Int. J. Mater. Sci. App.*, vol. 7(6), pp. 199-208, 2018.
- [83] Al-Hada, N. M., Kamari, H. M., Baqer, A. A., Shaari, A. H., and Saigon, E.,

- “Thermal Calcination-Based Production of SnO₂ Nanopowder: An Analysis of SnO₂ Nanoparticle Characteristics and Antibacterial Activities”, *Nanomaterials*, vol. 8(4), pp. 250, 2018.
- [84] Mariano M. R., Mietta, J. L., Soledad P., A., Perez, O. E., Negri, M. M., and Jeorge, G., “Structural and magnetic properties of Fe_{2-x}CoSm_xO₄ and Fe_{2-x}CoSm_xO₄-PDMS magneto elastomers as a function of Sm content”, *J. Magn.Magn mater.*, vol. 327, pp. 11-19, 2013.
- [85] Ahsan, M. Z., Khan, F.A., and Islam, M.A., “Frequency and temperature dependent dielectric and magnetic properties of manganese doped cobalt ferrite nanoparticles”, *J. Electron. Mater.*, vol. 48, pp.7721-7729, 2019.
- [86] Jacob, J., and Khadar, M. A. “Investigation of mixed spinel structure of nanostructured nickel ferrite”, *J. Appl. Phys*, vol. 107, pp.114310, 2010.
- [87] Bally, A. A., Ahsan, M. Z., Islam, M. A., Alam, M. K., and Khan, F. A., “Magnetic, magnetocaloric, and dielectric properties of polycrystalline perovskiteLa_{0.7}Ca_{0.2}Pb_{0.1}CoO₃”, *AIP Adv.* vol. 10, 015033, 2020.
- [88] Nakamura, T., “Low-temperature sintering of Ni-Zn-Cu ferrite and its permeability spectra”, *J. Magn. Magn. Mater.* vol. 168, pp.285-291, 1997.
- [89] K. Ishino, Y. and Narumiya, Development of magnetic ferrites: control and application of losses, *Am. Ceram. Soc. Bull.* vol. 66, pp. 1469-1474, 1987.
- [90] Pubby, K., Meena, S. S., Yusuf, S. M., and Narang, S. B., “Cobalt substituted nickel ferrites via Pechin’s sol-gel citrate route: X-band electromagnetic characterization”, *J. Magn, Magn Mat*, vol. 466, pp 430 – 445, 2018.
- [91] Nogai, R., Khan, S., Asokan, K., Ahmed, H., and Khan, I., “Magnetic and electrical properties of In doped cobalt ferrite nanoparticles”, *J. App. Phys*, vol. 112 , pp. 084321-1 – 084321-8, 2012.
- [92] Sunghyun, Yoon., Kannan, M., and Krishnan, “Temperature dependence magnetic anisotropy constant in manganese ferrite nanoparticles at low temperature”, *J. App, Phys*, vol. 109, pp. 07B534-1 - 07B534-3, 2011.
- [93] Chiranjib, N., Kaustuv, M., Gourab, B., Pattukkannu, M., and Ihab O., “Investigating Size- and Temperature-Dependent Coercivity and Saturation Magnetization in PEG Coated Fe₃O₄ Nanoparticles”, *Magnetochemistry*, vol. 3 (19), pp. 1-15, 2017.
- [94] Kittel, C., *Introduction to solid-state Physics*, 7th edition, John Wiley & Sons, Inc. Singapore, 1996.
- [95] Ovidiu, C, Rao, G.S.N., Rao, K.H., Rao, B.P., Dumitru, I., Chong-Oh Kim, and Geol G. K., “The influence of Mn doping level on magnetostriction

- coefficient of cobalt ferrite”, *J. Magn. Magn. Mat*, vol. 316(2), pp. 618-620, 2007.
- [96] Maaz, K., Mumtaz, A., Hasanian, S. K., and Ceylon, A., “Synthesis and magnetic properties of cobalt ferrite (CoFe_2O_4) nanoparticles prepared by wet chemical route”, *J. Magn. Mater*, vol. 308(2), pp 389-395, 2007.
- [97] Ahsan, M. Z., Ahsan, Pk. M. A., Islam, M. A., and Asif, F.C., “Structural and electrical properties of copper doped lanthanum manganite NPs”, *Results Phys.*, vol. 15, pp. 102600-1 – 202600-7, 2019.
- [98] Bhuvaneswari, M., Sendhilnathan, S., Kumar, M., Tamilarasan, R., and Giridharan, N. V., “Synthesis, investigation on structural and electrical properties of cobalt doped Mn–Zn ferrite nanocrystalline powders”, *Materials Sci.*, vol. 34(2), pp. 344-353, 2016.
- [99] Nasrin, S. Chowdhury, F.-U.-Z., and Hoque, S. M., “Study of hyperthermia temperature of manganese-substituted cobalt nanoferrites prepared by chemical co-precipitation method for biomedical application”, *J Magn. Magn. Mater*, vol. 449, pp. 126-134, 2019.
- [100] Bally, A. A., Ahsan, M. Z., Islam, M. A., Alam, M. K., and Khan, F. A., “Magnetic, magnetocaloric, and dielectric properties of polycrystalline perovskite $\text{La}_{0.7}\text{Ca}_{0.2}\text{Pb}_{0.1}\text{CoO}_3$ ”, *AIP Adv.*, vol. 10, 015033, 2020.
- [101] Nogai, R., Khan, S., Asokan, K., Ahmed, H., and Khan, I, “Magnetic and electrical properties of In doped cobalt ferrite nanoparticles”, *J. App. Phys*, vol. 112, pp. 084321-1 – 084321-8, 2012.
- [102] Krutika, L. Routray, and Dhruvananda, B., “Structural and Dielectric Properties of Bismuth Doped Cobalt Nano Ferrites Prepared by Sol-Gel Auto Combustion Method”, *IOP Conf. Series: Mater. Sci. and Eng.*, vol. 178, pp. 012007, 2017.
- [103] Hossain, A., Sarker, M. S. I., Khan, M. K. R., and Khan, F. A., Kamruzzaman, M., & Rahman, M. M. “Structural, magnetic, and electrical properties of sol–gel derived cobalt ferrite nanoparticles”. *Appl. Phys. A.*, vol. 124(9), pp. 608, 2018.
- [104] Nordblad, P. *Disordered Magnetic Systems. Reference Module in Materials Science and Materials Engineering*, (2016). doi:10.1016/b978-0-12-803581-8.01101-2
- [105] Hossein, M. B, and Hossain AKMA. “Complex impedance and electric modulus studies of magnetic ceramic $\text{Ni}_{0.27}\text{Cu}_{0.10}\text{Zn}_{0.63}\text{Fe}_2\text{O}_4$ ”, *J. Adv. Ceram.*, vol. 4(3), pp.217–25, 2015.
- [106] Rayssi, C., El.Kossi, S., Dhahri, J., and Khirouni, K. “Frequency and temperature-dependence of dielectric permittivity and electric modulus

- studies of the solid solution $\text{Ca}_{0.85}\text{Er}_{0.1}\text{Ti}_{1-x}\text{Co}_{4x/3}\text{O}_3$ ($0 \leq x \leq 0.1$)". RSC Adv., vol. 8(31), pp. 17139–17150, 2018.
- [107] Ebenezer, E. M., Abbas, Z., Azis, R. S., and Khamis, A. M., "Enhancement of complex permittivity and attenuation properties of recycled hematite (α - Fe_2O_3) using nanoparticles prepared via ball milling technique", Materials, vol. 12(10), pp. 1696, 2019.
- [108] Mathe, V. L., and Kamble R. B.. "Electrical and dielectric properties of nanocrystalline Ni-Co spinel ferrites", Mater. Res. Bull; vol. 43, pp.1415–1419, 2008.
- [109] Hongbo Gu, Hongyuan Zhang, Jing Lin, Qian Shao, David P. Young, Luyi Sun, T.D. Shen, and Zhanhu G., "Large negative giant magnetoresistance at room temperature and electrical transport in cobalt ferrite-polyaniline nanocomposites", Polymer, vol.143, pp. 24 – 330, 2018.
- [110] Islam, M. A., Khan, F. A., Ahsan, M. Z., and Bally, A.A. "Influence of manganese substitution on magnetoresistance and magnetic properties of $(\text{Fe}_{1-x}\text{Mn}_x)_{75}\text{P}_{15}\text{C}_{10}$ alloy ribbon", J.Non-Cryst. Solids, vol. 521, pp. 119479-1 – 5, 2019.
- [111] Ponpandian, N., Balaya, P., and Narayanasamy, A., "Electrical Conductivity and Dielectric Behaviour of Nanocrystalline NiFe_2O_4 Spinel", J. Phys. Cond. Mater. vol. 14, pp. 3221–3237, 2019.
- [112] Purnama, B., Tri Wijayanta, A., and Suharyana, "Effect of calcination temperature on structural and magnetic properties in cobalt ferrite nanoparticles", J. King Saud Univ. Sci., vol. 31, pp. 956-960, 2019.
- [113] Birajdar, AA, Shirsath Sagar, E, Kadam, RH, Patange, SM, Mane DR, and Shitre AR., "Rietveld structure refinement and cation distribution of Cr^{3+} substituted nanocrystalline Ni-Zn ferrites", ISRN Ceram., vol. 2012, pp.876123 | 5, 2012. .
- [114] Akhtar, M. Z., Khan, M.A., Ahmad, M., Nazir, M.S., Imran, M., Ali, A., Sattar, A., and Murtaza, G., "Evaluation of structural, morphological and magnetic properties of CuZnNi ($\text{Cu}_x\text{Zn}_{0.5-x}\text{Ni}_{0.5}\text{Fe}_2\text{O}_4$) nanocrystalline ferrites for core, switching and MLCI's applications, J.Magn, Magn, Mat, vol. 421, pp. 260-268, 2017.
- [115] Gharibshahi, L., Saigon, E., Gharibshahi, E., Shaari, and Khamirul, K. A., "Structural and Optical Properties of Ag Nanoparticles Synthesized by Thermal Treatment Method", Materials, vol. 10(4), pp. 402, 2017.
- [116] Saini, A., Thakur, A., and Thakur, P., "Matching permeability and permittivity of $\text{Ni}_{0.5}\text{Zn}_{0.3}\text{Co}_{0.2}\text{In}_{0.1}\text{Fe}_{1.9}\text{O}_4$ ferrite for the substrate of large bandwidth miniaturized antenna", Mater. Elec., vol. 27(3), pp. 2816–2823, 2015.

- [117] Kadam, A. A., Shinde, S. S., Yadav, S. P., Patil, P. S., and Rajpure, K. Y. "Structural, morphological, electrical and magnetic properties of Dy doped Ni–Co substitutional spinel ferrite". *J. Magn. Magn. Mat.*, vol. 329, pp. 59–64, 2013.
- [118] Mosallaei, H., and Sarabandi, K., "Magneto-dielectrics in electromagnetics: concept and applications", *IEEE Trans.* vol. 52, pp. 1558–1567, 2004.
- [119] Nlebedim, IC., Melikhov, Y., and Jiles, DC., "Temperature dependence of magnetic properties of heat-treated cobalt ferrite *J. Appl. Phys.*", vol. 15, pp. 043903, 2014.
- [120] George, T., Sunny, A. T., and Varghese, T., "Magnetic properties of cobalt ferrite nanoparticles synthesized by sol-gel method", *IOP Conf. Series: Mater. Sci. Eng.* vol. 73 (2015) 012050, 2012.
- [121] Gomes, J. A., Azevedo, G. M., Depeyrot, J., Mestnik-Filho, J., da Silva, G. J., Tourinho, F. A., and Perzynski, R., "ZnFe₂O₄ nanoparticles for ferrofluids: A combined XANES and XRD study". *J. Magn. Magn. Mat.*, vol. 323(10), pp. 1203–1206, 2011.
- [122] Molak A, Paluch M, Pawlus S, Klimontko J, Ujma Z, and Gruszka I. "Electric modulus approach to the analysis of electric relaxation in highly conducting (Na_{0.75}Bi_{0.25})(Mn_{0.25}Nb_{0.75})O₃ ceramics", *J. Phys. D. Appl. Phys.*, vol. 38: pp.1450–60, 2005.
- [123] Koop, C. G., "On the dispersion of resistivity and dielectric constant of some semiconductors at audio frequencies", *Phys Rev*, vol. 83(1), pp. 121–4 1951.
- [124] Al Arfaj, E., Hcini S, Mallah AR, Dhaou MH, and Bouazizi ML, "Effect of Co substitution on the microstructural, infrared, and electrical properties of Mg_{0.6-x}Co_xZn_{0.4}Fe₂O₄ ferrites" *J. Supercond. Nov. Magn.*, vol. 31, pp. 4107–4116, 2018.
- [125] Vasoya Jha, Saija Dolia, and Zankat M., "Electric modulus, scaling and modeling of dielectric properties for Mn²⁺-Si⁴⁺ Co-substituted Mn-Zn ferrites" *J. Electric Mater, J. Electron. Mater.*, vol. 45(2), pp. 917–927, 2015.
- [126] Barner, K., Mandal, P., Heimoit, RV., Chapter-VII: "Positive and Negative magnetoresistance in mixed superexchange–double exchange systems", *Phys. Status Solidi (B)*; vol. 223, pp. 811, 2001.
- [127] Pradhan, A. K, Nath, TK, and Saha, S., "Impedance spectroscopy and electric modulus behavior of molybdenum doped cobalt–zinc ferrite", *Mater. Res. Express*, vol. 4(7), pp. 0761107, 2017.
- [128] Mohanty V, Cheruku R, Vijayan L, and Govindara G., "Ce-substituted lithium ferrite: preparation and electrical relaxation studies", *J. Mater. Sci.*

Technol., vol. 30(4) pp. 335–41, 2014.

- [129] Byeong-Eog, J., Hyung-Kook, K., and Yoon-Hwae, H. “Electric modulus scaling behaviors of the near stoichiometric potassium lithium niobate”, *Cryst J. Korean Phys. Soc.*, vol. 49(6), pp. 2408–12, 2006.
- [130] Venkatesan, K., Rajan Babu, D., Kavya Bai, M P., Supriya, R., Vidya, R., Madeswaran, S., Anandan, P., Arivanandhan, M., and Hayakawa, Y. “Structural and magnetic properties of cobalt-doped iron oxide nanoparticles prepared by solution combustion method for biomedical applications”, *Int. J. Nanomedicine*. vol. 10, pp.189–198, 2015.
- [131] Birajdar, AA., Shirsath, Sagar., E, Kadam, RH, Patange, SM, Mane DR, and Shitre AR., “Rietveld structure refinement and cation distribution of Cr³⁺ substituted nanocrystalline Ni-Zn ferrites”, *ISRN Ceram.*, vol. 2012 |Article ID 876123 | 5, 2012.
- [132] Singh, J. P., Kumar, H., Singhal, A., Sarin, N., Srivastava, R. C., and Chae, K. H., “Solubility Limit, Magnetic Interaction and Conduction Mechanism in Rare Earth Doped Ferrites.”, *App. Sci.Lett.* vol. 2 (1), pp. 03-11, 2016.
- [133] Adrian Radoń, Łukasz Hawelek, Dariusz Łukowiec, Jerzy Kubacki, and Patryk W., “Dielectric and electromagnetic interference shielding properties of high entropy (Zn, Fe, Ni, Mg, Cd) Fe₂O₄ ferrite”, *Sci. Rep.* , vol. 9, pp. 20078, 2019.
- [134] Shore, K. A. “Electronic Processes in Non-crystalline Materials (Second Edition), by N.F. Mott and E.A. Davis”, *Contemp. Phys.*, vol. 55(4), pp. 337–337, 2014.
- [135] Shirsath, S. E, Toksha, B.G., and Jadhav, K. M., “Structural and magnetic properties of In³⁺ substituted NiFe₂O₄”. *Mater. Chem. Phys.*, vol. 117, pp.163, 2009.
- [136] Hemedat, O. M.. “IR spectral studies of Co_{0.6}Zn_{0.4}Mn_xFe_{2-x}O₄ ferrites”. *J. Magn. and Magn. Mater.*, vol. 281(1), pp. 36–41, 2004.

Appendices

I. Procedure of Stoichiometry Calculation

Step-1: Calculation of total molecular mass of compound (taken for sample) in g/mol.

Atomic mass of compound (amu)	Co g/mol	Mn g/mol	Fe g/mol	O g/mol	Total weight g/mol
Co ₂ O ₃	58.9332	-	-	15.9994	2x58.9332+3x15.9994 = 165.8646
MnO ₂	-	54.93805	-	15.9994	1x54.93805+2x15.9994 = 86.9368
Fe ₂ O ₃	-	-	55.845	15.9994	2x55.845+3x15.9994 = 159.6882

Step-2: Calculation of total molecular mass of the sample composition

Composition	x	Mass of the sample (g/mol)	Symb ol
<i>Co_{1-x}Mn_xFe₂O₄ (stoichiometric)</i>			
CoFe ₂ O ₄	0.000	58.9332+2x55.845+4x15.9994 = 234.6208	Parent (P)
Co _{0.875} Mn _{0.125} Fe ₂ O ₄	0.125	0.875x58.9332+0.125x54.93805+2x55.845+4x15.9994=234.12141	CMF-1
Co _{0.750} Mn _{0.250} Fe ₂ O ₄	0.250	0.750x58.9332+0.250x54.93805+2x55.845+4x15.9994=233.6220125	CMF-2
Co _{0.625} Mn _{0.375} Fe ₂ O ₄	0.375	0.625x58.9332+0.375x54.93805+2x55.845+4x15.9994=233.122618	CMF-3
Co _{0.500} Mn _{0.500} Fe ₂ O ₄	0.500	0.500x58.9332+0.500x54.93805+2x55.845+4x15.9994=232.623225	CMF-4
<i>CoMn_xFe_{2-x}O₄ (stoichiometric)</i>			
CoMn _{0.125} Fe _{1.875} O ₄	0.125	58.9332+0.125x54.93805+1.875x55.845+4x15.9994 = 234.5074313	CFM-1
CoMn _{0.250} Fe _{1.750} O ₄	0.250	58.9332+0.250x54.93805+1.750x55.845+4x15.9994 = 234.394175	CFM-2
CoMn _{0.375} Fe _{1.625} O ₄	0.375	58.9332+0.375x54.93805+1.625x55.845+4x15.9994 = 234.2966125	CFM-3
CoMn _{0.500} Fe _{1.500} O ₄	0.500	58.9332+0.500x54.93805+1.500x55.845+4x15.9994 = 234.19155	CFM-4
<i>Co_{1+x}Mn_xFe_{2-x}O₄ (Non-stoichiometric)</i>			
Co _{1.125} Mn _{0.125} Fe _{1.875} O ₄	0.125	1.125x58.9332+0.125x54.93805+1.875x55.845+4x15.9994=241.8741	CFMZ-1
Co _{1.250} Mn _{0.250} Fe _{1.750} O ₄	0.250	1.250x58.9332+0.250x54.93805+1.750x55.845+4x15.9994=249.1275	CFMZ-2
Co _{1.375} Mn _{0.375} Fe _{1.625} O ₄	0.375	1.375x58.9332+0.375x54.93805+1.625x55.845+4x15.9994=256.3805	CFMZ-3
Co _{1.500} Mn _{0.500} Fe _{1.500} O ₄	0.500	1.500x58.9332+0.500x54.93805+1.500x55.845+4x15.9994=263.6334	CFMZ-4
<i>Co_{1-x}Mn_xFe_{2+x}O₄ (Non-stoichiometric)</i>			
Co _{0.875} Mn _{0.125} Fe _{2.125} O ₄	0.125	0.875x58.9332+0.125x54.93805+2.125x55.845+4x15.9994=241.102	
Co _{0.750} Mn _{0.250} Fe _{2.250} O ₄	0.250	0.750x58.9332+0.250x54.93805+2.25x55.845+4x15.9994=247.583	
Co _{0.625} Mn _{0.375} Fe _{2.375} O ₄	0.375	0.625x58.9332+0.375x54.93805+2.375x55.845+4x15.9994=254.06	
Co _{0.500} Mn _{0.500} Fe _{2.500} O ₄	0.500	0.500x58.9332+0.500x54.93805+2.5x55.845+4x15.9994=260.546	

Step-3: Calculation of raw materials for 15 g sample of each composition

Composition	X	Molar Mass (TM)	Co ₂ O ₃ (165.8646)	MnO ₂ (86.9368)	Fe ₂ O ₃ (159.6882)	Symbol
<i>Co_{1-x}Mn_xFe₂O₄ (stoichiometric)</i>						
CoFe ₂ O ₄	0.000	234.6208	5.3021	0	9.6979	Parent (P)
Co _{0.875} Mn _{0.125} Fe ₂ O ₄	0.125	234.12141	5.3134	5.56998	4.11662	CMF-1
Co _{0.750} Mn _{0.250} Fe ₂ O ₄	0.250	233.6220125	5.3248	5.58189	4.09331	CMF-2
Co _{0.625} Mn _{0.375} Fe ₂ O ₄	0.375	233.122618	5.3362	5.5938	4.07	CMF-3
Co _{0.500} Mn _{0.500} Fe ₂ O ₄	0.500	232.623225	5.3476	5.6059	4.0465	CMF-4
Total			26.6241	22.35157	26.02433	75
<i>CoMn_xFe_{2-x}O₄ (stoichiometric)</i>						
CoMn _{0.125} Fe _{1.875} O ₄	0.125	234.5074	5.3047	5.5608	4.1345	CFM-1
CoMn _{0.250} Fe _{1.750} O ₄	0.250	234.394175	5.3072	5.5635	4.1293	CFM-2
CoMn _{0.375} Fe _{1.625} O ₄	0.375	234.2966125	5.3094	5.5658	4.1248	CFM-3
CoMn _{0.500} Fe _{1.500} O ₄	0.500	234.19155	5.3118	5.5683	4.1199	CFM-4
Total			21.2331	22.2584	16.5085	60
<i>Co_{1+x}Mn_xFe_{2-x}O₄ (Non-stoichiometric)</i>						
Co _{1.125} Mn _{0.125} Fe _{1.875} O ₄	0.125	241.8741	5.1431	5.3914	4.4655	CFMZ-1
Co _{1.250} Mn _{0.250} Fe _{1.750} O ₄	0.250	249.1275	4.9933	5.2345	4.7722	CFMZ-2
Co _{1.375} Mn _{0.375} Fe _{1.625} O ₄	0.375	256.3805	4.8521	5.0914	5.0565	CFMZ-3
Co _{1.500} Mn _{0.500} Fe _{1.500} O ₄	0.500	263.6334	4.7186	4.9465	5.3349	CFMZ-4
Total			19.7071	20.6638	19.6291	60
Requirement of raw materials						
Total Requirement			67.5643	65.27377	62.16193	195 g

II. Used Formulas

The formulas used for calculation of various parameters for analysis of structural, magnetic, and electrical properties along with software are listed in the following

Table: The formula/procedure used for calculation of different parameters used in this thesis paper

Parameters	Formula	Remarks
Structural		
Lattice Constant	$d = \frac{a}{\sqrt{h^2 + k^2 + l^2}}$	Using high score plus soft ware
Crystallite Size	$0.9\lambda/\beta \cos \theta$	Debye–Scherrer formula
Tetrahedral hopping length	$(L) = \frac{a\sqrt{3}}{4} \text{Å}$	
Octahedral hopping length	$[L] = \frac{a\sqrt{2}}{4} \text{Å}$	
Tetrahedral bond length	$A - O = \left(u - \frac{1}{4}\right) a\sqrt{3} \text{Å}$	Stanley's equation
Octahedral bond length	$B - O = \left(\frac{5}{8} - u\right) a \text{Å}$	
X-ray density	$\rho_x = ZM/Na^3$	
Porosity	$P\% = \left(1 - \frac{\rho_x}{\rho}\right) \times 100$	
Strain	$\beta \cos \theta = \frac{k\lambda}{D} + 4\epsilon \sin \theta$	Williamson–Hall equation (plot)
Magnetic		
Magnetization	$(V_{measd} \times Cac - Const)/M_{measrd}$	Using VSM
Coercivity	$(H_{c1} + H_{c2})/2$	Using hysteresis curves
Remnant Magnetization	$(M_{c1} + M_{c2})/2$	
Curie Temperature	Extrapolated intercept value	Using M – T curves
Anisotropy constant		
Initial Permeability	The slope value at initial magnetization	Using M – H curves
Susceptibility	$M/\mu_0 H$	
Electrical		
DC resistivity	$\rho_{dc} = RA/l$	
DC Conductivity	$\sigma_{dc} = 1/\rho_{dc}$	Using the 4-probe method
AC Resistivity	$\rho_{ac} = RA/l$	
AC Conductivity	$\sigma_{ac} = 1/\rho_{ac}$	Using Wynekerr Impedance analyzer
Magnetoresistance	$MR\% = \frac{\rho_H - \rho_0}{\rho_0} \times 100$	Using the 4-probe method

Electromagnetic

Complex permittivity	$\varepsilon = \varepsilon' - j\varepsilon''$	
Complex permeability	$\mu = \mu' - j\mu''$	
Impedance	$Z = \sqrt{R^2 + X^2}$	Measurement of real and imaginary parts by impedance analyzer
Characteristics impedance	$Z_0 = \sqrt{\mu'/\varepsilon'}$	
Miniaturization factor	$n = \sqrt{\mu' \times \varepsilon'}$	
Dielectric constant	$\varepsilon_r = \frac{C}{C_0}$	Measurement of capacitance by impedance analyzer
Dielectric loss	$\tan \delta = \varepsilon''/\varepsilon'$	Measurement of real and imaginary parts by impedance analyzer
Magnetic loss	$\tan \delta = \mu''/\mu'$	
Eddy current loss	$W_{ed.loss} = \omega\mu_r\mu_0H^2V \sin \delta$	Usual meanings
Currie constant, C	The slope of $\frac{1}{\chi} - T$ plot	
Weise constant, θ	The intercept at the temperature axis	Usual meanings
Electric modulus	$M'(\omega) = \frac{\varepsilon'(\omega)}{\varepsilon'(\omega)^2 + \varepsilon''(\omega)^2}$	Real part
	$M''(\omega) = \frac{\varepsilon''(\omega)}{\varepsilon'(\omega)^2 + \varepsilon''(\omega)^2}$	Imaginary part
Magnetic modulus	$M'_m(\omega) = \frac{\mu'(\omega)}{\mu'(\omega)^2 + \mu''(\omega)^2}$	Real part
	$M''_m(\omega) = \frac{\mu''(\omega)}{\mu'(\omega)^2 + \mu''(\omega)^2}$	Imaginary part

III. List of publications

1. **M. Z. Ahsan** , F.A. Khan, M. A. Islam, “Frequency and temperature dependent intrinsic electric properties of manganese doped cobalt ferrite nanoparticles”, (2019), Results in Physics, Vol 14, 102484 (ELSIVIER)
2. **M. Z. Ahsan** , F.A. Khan, M. A. Islam, “Frequency and temperature dependent dielectric and magnetic properties of Manganese doped Cobalt ferrite nanoparticles”, (2019), J. EMS, Vol-48(12), pp. 7721-7729 (Springer)
3. **M. Z. Ahsan**, F A Khan, M A Islam, Tanzina Tabassum, M K Alam, “Study on AC permeability and permittivity of manganese doped cobalt ferrite nanoparticles” (2018), J.Phys.Commun. Vol-2(10), 105008 (IOP)
4. **M. Z. Ahsan**, F A Khan, “Structural and electrical properties of manganese doped cobalt ferrite nanoparticles”, (2018), Mater Sci Nanotechnol.2(2), pp. 1-9 (Allied).
5. **M. Z. Ahsan**, F. A. Khan, Pk. A. Ahsan, M. A. Islam, “Exploiting of magnetocaloric effect from manganese doped cobalt ferrite nanoparticles for low temperature applications “, (2018), IJRTEM , 2 (12), pp. 43-46)
6. **M. Z. Ahsan** and F. A Khan, “Influence of milling time on structural and electromagnetic properties of manganese doped cobalt ferrite nanoparticles”, (2018), Journal of Materials Science and Applications, Vol-7(6), pp. 199-208 Science PG, SA
7. **M. Z. Ahsan**, F. A. Khan, “Study of Structural, Electrical and Magnetic Properties of Manganese Doped Cobalt Ferrite Nanoparticles with Non-stoichiometric Composition”, (2017), Journal of Physical Science and Application 7 (6) pp. 30-37
8. **M. Z. Ahsan**, M. A. Islam, A. A. Bally , F. A. Khan, “Spectroscopic analysis for electric and magnetic properties of manganese doped cobalt nanoferrite ” ,(2020), Results in Physics, (ELSIVIER) 17, 103172
9. **M. Z. Ahsan** , M. A. Islam, F.A. Khan, “Effects of sintering temperature on ac conductivity, permittivity, and permeability of manganese doped cobalt ferrite nanoparticles”, (2020) , Results in Physics , (ELSIVIER) , 19, 103402
10. **M. Z. Ahsan**, M. A. Islam, M. A. A. Bally, Tanzina Tabassum, F. A. Khan, “Significances of complex impedance in stoichiometric and non-stoichiometric composition of manganese doped cobalt ferrite nanoparticles”, (2020), IJISSET, Vol-6, Issue-7
11. **M. Z. Ahsan**, M. A. Islam, A. A. Bally, Tanzina Tabassum, F. A. Khan, “Temperature dependent Magnetization of Manganese doped Cobalt ferrite Nanoparticles”, (2020) , Journal of Materials, (Accepted)